5-2008

Characterizing and Modeling the Hydrodynamics of Shallow Spouted Beds

Jiandong Zhou

University of Tennessee - Knoxville

To the Graduate Council:

I am submitting herewith a dissertation written by Jiandong Zhou entitled "Characterizing and Modeling the Hydrodynamics of Shallow Spouted Beds." I have examined the final electronic copy of this dissertation for form and content and recommend that it be accepted in partial fulfillment of the requirements for the degree of Doctor of Philosophy, with a major in Chemical Engineering.

Duane D. Bruns, Major Professor

We have read this dissertation and recommend its acceptance:

C. Stuart Daw, David J. Keffer, Hamparsum Bozdogan, Sreekanth Pannala, Charles E. A. Finney

Accepted for the Council:

Carolyn R. Hodges

Vice Provost and Dean of the Graduate School

(Original signatures are on file with official student records.)

To the Graduate Council:

I am submitting herewith a dissertation written by Jiandong Zhou entitled "Characterizing and modeling the hydrodynamics of shallow spouted beds" I have examined the final electronic copy of this dissertation for form and content and recommend that it be accepted in partial fulfillment of the requirements for the degree of Doctor of Philosophy, with a major in Chemical Engineering.

Duane D. Bruns

Major Professor

We have read this dissertation
and recommend its acceptance:

C. Stuart Daw

David J. Keffer

Hamparsum Bozdogan

Sreekanth Pannala

Charles E A Finney

Acceptance for the Council:

Carolyn R. Hodges

Vice Provost & Dean of the Graduate School

(Original signatures are on file with official student records.)

Characterizing and Modeling the Hydrodynamics of Shallow Spouted Beds

A Dissertation
Presented for the
Doctor of Philosophy
Degree
The University of Tennessee, Knoxville

Jiandong Zhou
May 2008

DEDICATION

This dissertation is dedicated to my wife, Qiu Xia, who always supports me and encourages me, and my daughter, Shanning Zhou who inspires me a lot, and my parents and parents-in-law, who encourage me to achieve my goals.

Acknowledgments

I acknowledge support from the U.S. Department of Energy, from Oak Ridge National Laboratory, from APAL (Applied Process Automation Laboratory), from the department of the chemical engineering at the University of Tennessee, Knoxville (UTK), and from TANDEC (Textile and Nonwoven Development Center) of UTK.

I would like to express my deep appreciation to Dr. C. Stuart Daw for a lot of his advices, guidance and help. Dr. Daw also spent a lot of time and energy on commenting on my dissertation after Dr. Bruns got sick. Without Dr. Daw, I would not have obtained my Ph. D degree. I also deeply thank my advisor, Dr. Duane D. Bruns, for his support and instructions during my Ph. D education. I sincerely thank Dr. Charles E A Finney for carefully reviewing my dissertation. I truly thank Dr. Sreekanth Pannala and Dr. Michael J. Roberts for their guidance and help. I also thank Dr. David J. Keffer and Dr. Hamparsum Bozdogan who are among the committee members and spent time and energy on my dissertation. I also express my thanks to my colleagues at UTK for their help, especially Deytcia Lima Rojas, Karl R Menako, Sandeep Rajput, and Alok Patel. I also thank Mr. Douglas E. Fielden for his skillful designing and making some of the equipments.

I want to thank the administration, faculty and staff of the Department of Chemical Engineering of the University of Tennessee, Knoxville for the guidance and help.

I am deeply grateful to my wife, who always not only encourages me but also overcomes a lot of difficulties by herself in order to support me.

Finally, I acknowledge the support and encouragement of my parents and my parents-in-law.

Abstract

The hydrodynamics of shallow, conical spouted beds of heavy particles were experimentally studied to determine how they differ from previous spouted bed reports in the literature. Key experimental measurements included minimum spouting velocity, time-average and time-varying (dynamic) pressure drop, time-average fountain height and time-average gas velocity profile in the bed. New correlations were developed for minimum spouting velocity, time-average pressure drop and fountain height based on the experimental data. The time-average gas velocity profile measurements confirmed that the beds in the present study exhibited gas flow features that were at least qualitatively similar to those previously reported for other experimental conical spouted beds and predicted by detailed computational fluid dynamics models.

At least some of the major features of the observed spouted bed pulsation behavior appear to be captured by a simple zone-based model of ordinary differential equations. The equations are derived from time-differential mass and momentum balances over 4 spatial zones: entrainment, spout, fountain, and annulus. The dynamic behavior of the model is dominated by the entrainment zone, which includes the effects of 3 key processes: 1) Granular particle flow from the annulus into the area immediately above the gas inlet; 2) Radial leakage of gas outward from the inlet zone in response to the inward flowing particles and; 3) Upward flow of the main part of the inlet gas and subsequent particle entrainment in response to the gas-particle drag. Recommendations are made for further improvements to the model.

Contents

List of figures

List of tables

NOMENCLATURE

Units are denoted by M for mass, L for length, T for time, and rad for radians.

A	$= [\rho_g/(\rho_p-\rho_g][U_{mf}u_T/(gD_i)]$, used in the Day (1990) H_f correlation, dimensionless
A_E	cross-sectional area of entrainment zone, $[L^2]$
A_S	cross-sectional area of spout zone, $[L^2]$
Ar	$= \frac{d_p^{\,3}\rho_p(\rho_p-\rho_g)g}{\mu^2}$, Archimedes number, dimensionless
C_d	drag coefficient, dimensionless
D_i	inlet diameter, [L]
d_p	particle diameter, [L]
D_b	diameter of the bottom of the spouted bed, [L]
D_c	diameter of the column part of the spouted bed, [L]
D_s	spout diameter, [L]
F_{Ed}	gas drag force exerted on particles in the entrainment zone, $[MLT^{-2}]$
F_{Sd}	gas drag force exerted on particles in the spout zone, $[MLT^{-2}]$
F_s	$= e^{-1000(\varepsilon_E-\varepsilon_{Emf})}$, solids resistance to compression, dimensionless
g	gravitational acceleration, $[LT^{-2}]$
G	$= k_E t_c$, ratio of characteristic gravitational time to characteristic granular flow time, dimensionless
k_E	rate constant used for granular flow from annulus to entrainment zone, $[T^{-1}]$
H	bed height, [L]
H_0	static particle height in the spouted bed, [L]

H_E height of the entrainment zone, [L]

H_F height of the fountain zone, [L]

H_f fountain height, [L]

H_S height of the spout zone, [L]

H_m maximum spoutable bed height, [L]

m_{Ap} mass of particles in the annular zone, [M]

m_{Ep} mass of particles in the entrainment zone, [M]

m_{Fp} mass of particles in the fountain zone, [M]

m_{Sp} mass of particles in the spout zone, [M]

m_{Tp} total mass of particles in the bed, [M]

m_{Eg} mass of gas in the entrainment zone, [M]

P_a gas pressure in the annulus, $[ML^{-1}T^{-2}]$

P_s gas pressure in the spout, $[ML^{-1}T^{-2}]$

P_t total gas pressure, $[ML^{-1}T^{-2}]$

ΔP gas pressure drop, $[ML^{-1}T^{-2}]$

ΔP_E gas pressure drop in the entrainment zone, $[ML^{-1}T^{-2}]$

ΔP_S gas pressure drop in the spout zone, $[ML^{-1}T^{-2}]$

ΔP_F gas pressure drop in the fountain zone, $[ML^{-1}T^{-2}]$

ΔP_{Ep} gas pressure drop due to particles in the entrainment zone, $[ML^{-1}T^{-2}]$

ΔP_{Sp} gas pressure drop due to particles in the spout zone, $[ML^{-1}T^{-2}]$

ΔP_M maximum pressure drop, peak pressure drop, $[ML^{-1}T^{-2}]$

ΔP_{mf} minimum fluidization pressure drop in a bed of height H, $[ML^{-1}T^{-2}]$

ΔP_{ms} overall spout pressure at minimum spouting, $[ML^{-1}T^{-2}]$

ΔP_s stable spouting pressure drop, $[ML^{-1}T^{-2}]$

Q gas flow rate, $[L^3T^{-1}]$

Re_p $= \frac{d_p u \rho_g}{\mu}$, particle Reynolds number, dimensionless

Re_{ims} $= \frac{d_i u_{ms} \rho_g}{\mu}$, Reynolds number of minimum spouting velocity referred to d_i, dimensionless

Re_{ms} $= \frac{d_p u_{ms} \rho_g}{\mu}$, Reynolds number of minimum spouting velocity, dimensionless

t time, [T]

t_c $= (H_E/g)^{0.5}$, characteristic gravitational time scale, [T]

u gas velocity, $[LT^{-1}]$

u_A gas velocity in the annulus, $[LT^{-1}]$

u_i gas velocity based on spouted bed inlet diameter, $[LT^{-1}]$

u_M maximum gas velocity, $[LT^{-1}]$

u_T particle terminal velocity, $[LT^{-1}]$

U_{mf} minimum fluidization velocity, $[LT^{-1}]$

U_{ms} minimum spouting velocity, $[LT^{-1}]$

u_S gas velocity in the spout, $[LT^{-1}]$

v particle velocity, $[LT^{-1}]$

v_A particle velocity in the annular, $[LT^{-1}]$

v_{Ep} particle velocity in the entrainment zone, $[LT^{-1}]$

v_{Sp} particle velocity in the spout zone, $[LT^{-1}]$

v_{Fp} particle velocity in the fountain zone, $[LT^{-1}]$

v_{SH} particle velocity in the spout at $z = H_0$, $[LT^{-1}]$

v_{SHmax} particle velocity along axis of the column at the top of the spout, $[LT^{-1}]$

V_A volume of the annular zone, $[L^3]$

z vertical coordinate measured from spout inlet, [L]

Greek symbols

β friction coefficient, dimensionless

ε void fraction, dimensionless

ε_{mf} void fraction at minimum fluidization, dimensionless

ε_E void fraction in the entrainment zone, dimensionless

ε_S void fraction in the spout zone, dimensionless

ε_{SH} void fraction in the spout at $z = H_0$, dimensionless

ε_a annular void fraction, dimensionless

θ angle of internal friction, [rad]

ζ $= z/H_0$, nondimensional axial coordinate, dimensionless

μ fluid viscosity, $[ML^{-1}T^{-1}]$

γ cone angle, [rad]

ρ_b bulk density of particles, $[ML^{-3}]$

ρ_p particle density, $[ML^{-3}]$

ρ_g fluid density, $[ML^{-3}]$

Φ particle sphericity, dimensionless

1. Motivation and Objectives

Since spouted beds were first extensively utilized in Canada in 1950s, they have become widely used for many gas-solids contacting processes in which controlled solids circulation is important. The list of such applications is extensive, including grain drying, minerals beneficiation, pill coating, and solids agglomeration.

A particular application that has been an important motivation in this research project is spouted bed particle coating using chemical vapor deposition (CVD). One version of spouted bed CVD is utilized in the production of nuclear fuels used in Advanced High-Temperature Gas-Cooled Nuclear Reactors (AGR). The AGR fuels are composed of uranium-bearing (such as UCO) particles (kernels) that have been coated with four different layers of carbon and silicon carbide to prevent the release of gaseous fission products from the particle (and thus reactor) core. The current AGR fuel production process utilizes a form of shallow spouted bed CVD which operates at high temperatures (e.g., ~1200 °C). Developing improved methods for designing and controlling these coaters has become a high priority in the implementation of AGR technology. The AGR spouted bed coaters are particularly challenging because of the limited ability for making measurements and because the stringent quality requirements of the final product depend heavily on the detailed time-temperature-species history of particles.

Phenomenologically, spouted beds have many features in common with more conventional fluidized beds, such as multi-phase turbulence, high interphase heat and mass transfer, widely variable flow conditions, and complex dynamical relationships that

make scale-up from laboratory to full-scale systems extremely challenging. Spouted beds also have some characteristic features that are relatively unique, including a single (or limited number) of primary gas inlets, a very dominant global circulation pattern (with distinctive pulsations), and highly distinct spatial zones that include lean entrained particle flow (i.e., pneumatic transport) and dense solids flow (i.e., defluidized granular flow).

Although there is considerable published literature on experimental studies of relatively deep spouted beds (i.e., spouted beds where the bed height ≥ the bed diameter), there is relatively little information about shallow beds with the type of dense particles used for AGR fuel coating. In addition, the spouted bed data available are virtually all constrained to time average measurements and correlations, and there is almost no information concerning the dynamics (i.e., the time variations) of spouted bed processes. This lack of information about shallow spouted beds and their dynamics was the primary motivation behind the initiation of this study.

The overall objective of the present investigation is to conduct an experimental study of the hydrodynamics of a shallow spouted bed of dense particles at ambient temperature and pressure and to use the results of these experiments to develop improved correlations and a low-order dynamic model that accurately describe the observed trends. Key questions to be addressed in this investigation include the following:

- How different are the observed trends in minimum spouting velocity, fountain height, and time-average pressure drop compared to the trends in the literature?

- How much gas interchange is there between the spout core and outer annulus as a function of operating conditions?
- How extensive and complex is the gas-solids pulsation behavior?
- What are the competing mechanisms which are driving the pulsations in a spouted bed? Can they be of relevant to other fluidization regimes? If there are any outstanding issues in terms of the basic mechanism, what can be done to identify and understand those processes?
- Is it possible to construct a simple ODE model that can replicate many of the features seen in the pulsation dynamics?
- What are the overall implications of the above for developing improved designs and control schemes for spouted bed processes?

2. Background

2.1 TRISO Fuel Particle Coating

The United States is developing a new generation of High-Temperature Gas-Cooled Reactor (HTGR) referred to as the Advanced Gas-Cooled Reactor (AGR) [Atkins, 1969]**.** This type of reactor requires a special TRISO (tri-structural-isotropic) nuclear fuel [Heit, 1986]. In TRISO fuel, the fissile uranium component is contained as kernels of discrete UO_2 or UCO particles that are coated with layers of carbon and silicon carbide. The coated particles are then compacted into larger pellets used in fuel rods. The specialized construction of the coated kernels prevents the release of the fission products from the nuclear reactor core as nuclear disintegrations occur and also improves the thermo-mechanical durability of the fuel during storage, movement, and usage [Beatty *et al.*, 1965].

Figure 2.1 depicts the cross-section of a TRISO coated uranium fuel particle. The white area at the center is the uranium oxy-carbide kernel. Around the kernel are four successive coating layers: 1) an amorphous (soft) carbon layer (referred to as the buffer layer); 2) an inner pyrolytic (hard) carbon layer (referred to as the IPyC layer); 3) a silicon carbide (SiC) layer; and finally 4) an outer pyrolytic carbon (OPyC) layer. Depending on the fuel specifications, the kernel may be between 200 and 350 μm in diameter. The coating layers are added to the kernel using a stepwise chemical vapor deposition (CVD) process carried out in a spouted bed reactor. During coating, the particle diameter increases to 900–1000μm or more [Daw, 2005]. Maintaining the

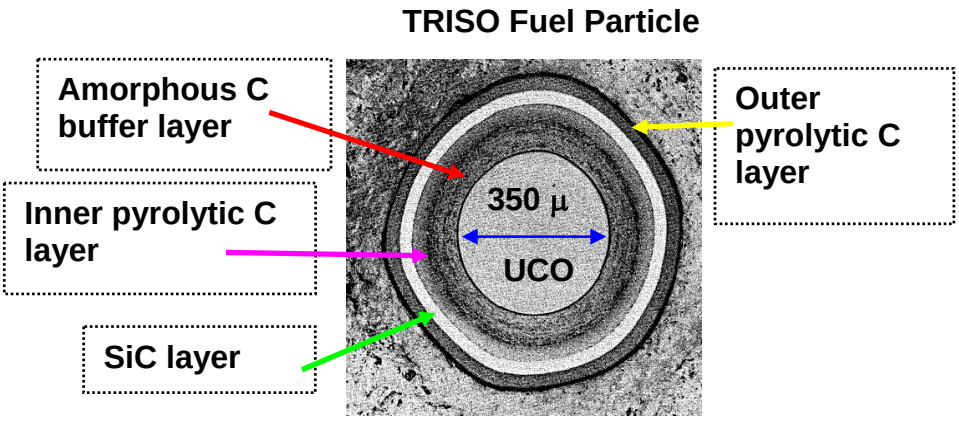

Figure 2.1 Cross-section of a TRISO coated nuclear fuel particle.

uniformity and integrity of the external layers during coating is critical because the AGR fuel specifications require less than one failure in 100,000 [Pannala, 2005a].

The actual design of the spouted bed coaters used for TRISO fuel production is still under development, so the process information presented here is generic rather than precisely quantitative. The currently favored design is based on a shallow spouted bed CVD reactor operated at approximately 1200°C. Because fuel coating quality is so critical to proper AGR performance, design and control these coaters have high priority in implementing AGR research and development [Daw, 2005].

Figure 2.2 shows a schematic of the 2-inch (5.08-cm)-diameter nuclear fuel coater used in experimental studies at Oak Ridge National Laboratory (ORNL) [Pannala *et al*., 2004]. In this particular design, the CVD reactor is constructed from a simple conical spouted bed enclosed in an electrically heated furnace. The inlet gases include argon as carrier,

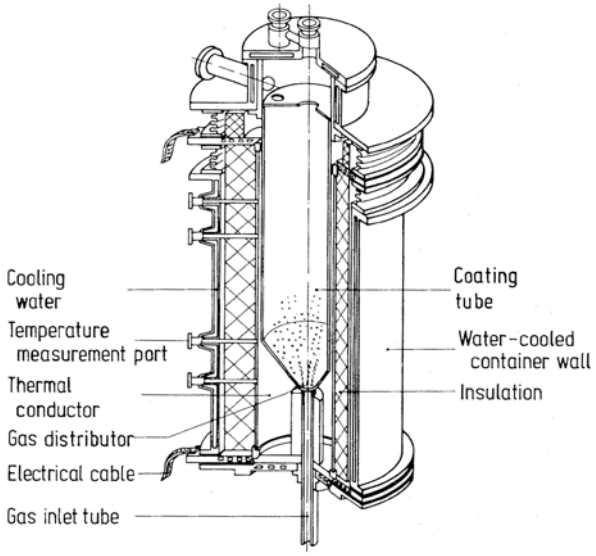

Figure 2.2 Schematic drawing of the 2-inch (5.08-cm)-diameter laboratory TRISO nuclear fuel particle coater used in experiments at ORNL.

plus reactant gases containing hydrogen, methyl trichlorosilane (MTS) and/or propylene depending on which of the four different coatings is being applied.

As the gases flow into the spouted bed through the inlet, they form a central region of dilute phase gas-solids flow (central core or spout zone). Particles are entrained by the gas near the inlet, flow upward through the core and then are ejected from the bed and disengaged from the gas in the spout. As they rise from the inlet, spout gases are rapidly heated from near ambient to bed temperature in a few milliseconds and begin to decompose into free radicals and/or nanoscale particles that become the building blocks

of the coating layer. After separating from the particles, the gas continues upward and out the coater exit.

When particles land back on the surface of the bed, they slowly migrate back toward the bed inlet. The repeated entrainment and return of particles creates a global recirculation process that alternately exposes each particle to the gases in the central core and the outer annular zone where gas flow is much reduced. It is believed that the details of this alternating exposure (e.g., the precise time, temperature, and gas composition history experienced by the particles) are the key to coating quality [Gyarmati and Nickel, 1973; Gyarmati *et al.,* 1983; Voice and Lamb, 1969; Stinton and Lackey, 1977; Lauf and Braski, 1980]. Each of the four coatings is added in a similar fashion by sequentially adjusting the inlet gas composition, flow and temperature (so that particles are treated in a batchwise operation) [Daw, 2007].

In order to produce large quantities of fuel to support commercial AGRs, spouted bed coaters will be needed that are much larger than the present experimental 5-cm diameter coaters at ORNL. As with other types of fluidized beds, there is no universal way to scale up the hydrodynamics of spouted beds *a priori* [Knowlton *et al*., 2005]. Thus a considerable amount of experimentation at different scales is required to develop a reliable full-scale AGR coater design with the desired gas-solids mixing and heat transfer characteristics. Unfortunately, as discussed below, many of the empirical correlations available for spouted bed design in the literature are not applicable for beds as shallow and with such dense solids as those required for TRISO fuels coating.

The situation in AGR coaters is further complicated by the high bed temperature, high inlet gas temperature gradient, and highly reactive species present (including fine particulates), which make it nearly impossible to make direct measurements of the particles during coating. Thus most of what is known about the hydrodynamics and mixing of AGR coaters must be inferred from indirect measurements such as pressure in the gas inlet [Daw, 2005]. Very little is understood about the details of the chemistry also [Daw, 2007].

Given the above constraints and limited state of knowledge, it was decided that the present study should focus on establishing the hydrodynamics of shallow, ambient temperature beds similar to those employed in the ORNL laboratory coating studies. ZrO_2 particles were selected as surrogate fuel particles because of their durability, nearly spherical shape, and high density.

2.2 Spouted Bed Hydrodynamics

Like other types of fluidized beds, spouted beds are good for solid-gas contacting over a wide range of operating conditions. When designed and operated properly, spouted beds are able to achieve good mixing and uniform surface exposure for all the solids. Spouted beds are especially useful for agglomerating solids [Shuck and Knudsen, 1982], and they come in a variety of geometries, including flat base, conical base, jet inlet and rectangular bed, as shown in figure 2.3 [Bi, 2004; Rocha *et al.*, 1995]. The current geometry of choice for nuclear fuel particle coating is based on the conical base design [Daw, 2005].

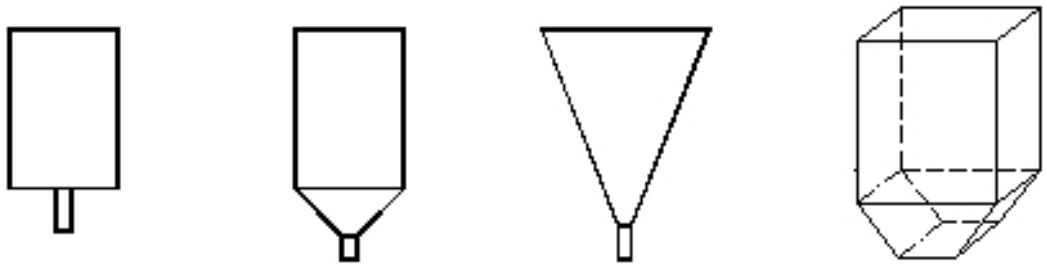

(a) Flat-base (b) Conical-base (c) Jet spouted bed (d) Rectangular bed

Figure 2.3 Four basic geometric configurations of spouted beds.

For coating, the bed is operated with a shallow depth (so that the vertical height of solids in the cylindrical zone is less than the bed diameter).

Figure 2.4 is a schematic of a shallow conical spouted bed as it appears in operation and as it appears when gas flow is turned off. For discussion purposes it is convenient to divide the operating bed into three characteristic zones: the spout, the fountain, and the annulus. As described above, high-velocity gas enters the bed through the inlet at the base, and particles near the inlet are entrained and carried up through the central core or spout zone in dilute two-phase flow. As the particles reach the bed surface and enter the fountain, drag from the gas rapidly diminishes. Particles in the fountain continue to move upward due to inertia, but eventually their velocities decelerate to zero due to the action of gravity, and they fall back to the bed surface. At this point the solids enter the annular zone, where they gradually flow down to the bottom of the bed and are picked up again by the gas.

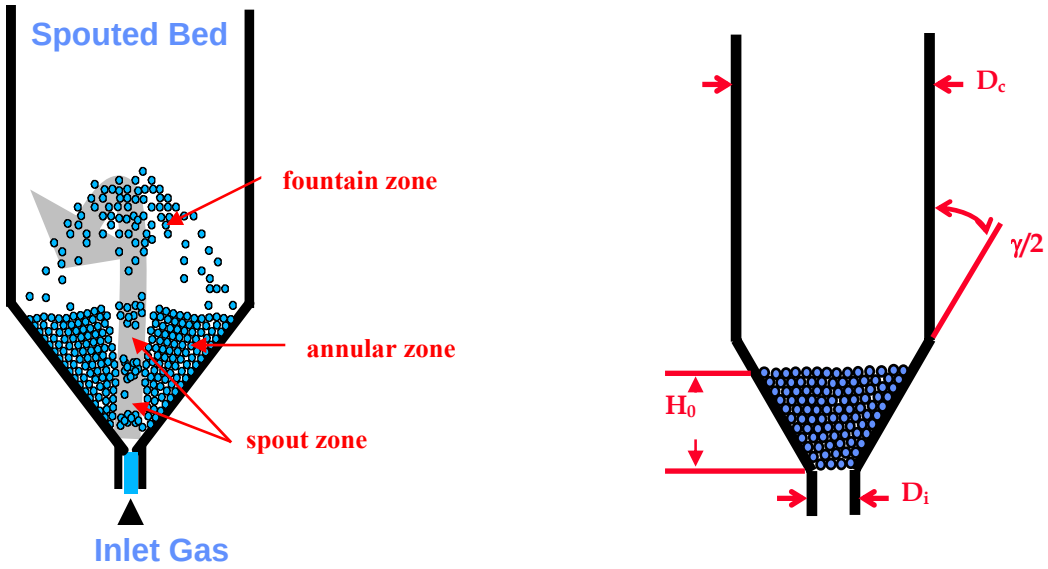

(a) Spouted bed in operation (b) Spouted bed in assumed static condition

Figure 2.4 Schematic drawing of a shallow conical spouted bed in operation (a) and with gas flow absent (b). The latter state is also referred to as the static condition.

An important feature of conical spouted beds is that they typically have little or no dead zones where solids can become trapped. The single, central gas inlet creates a very strong global circulation of solids [Mathur and Epstein, 1974a] that helps maintain the distinctiveness of the three major zones. In simple terms, the global solids circulation is created by the entrainment of solids at the gas inlet. These entrained solids are pushed upward by the gas-solids drag, leaving a momentary void pocket at the apex of the cone which then refills with new solids flowing in from the annulus. For many operating conditions, the repeated emptying and refilling of this void pocket results in a pulsing action, which can be observed visually and also measured in pressure signals as described below.

Like other fluidized beds, conical spouted beds can still have poor performance due to

incorrect design or inappropriate operating conditions for the particular process and solids involved. Such poor performance can be associated with specific issues such as unstable (erratic) flows, hot spots, and particle sintering and agglomeration. All of these issues are important to avoid in TRISO fuel coating.

Certain key experimental measurements have become widely used for characterizing and correlating the hydrodynamics of spouted beds. These measurements include minimum spouting velocity, gas pressure drop, fountain height, and gas velocity distribution. In most cases, the reported values for these quantities in the literature are time average values, so that information about dynamic fluctuations (that is, variations over time) has been removed. As is discussed below, it is now recognized that such dynamic information can be key to understanding the underlying physics.

The minimum spouting velocity (denoted $U_{ms)}$ corresponds to the minimum inlet gas velocity needed to maintain the spouted state in the gas-solid spouted bed [Mathur, 1974b]. Below this critical gas flow, there is no entrainment of the solids at the inlet and global solids circulation is absent. Above this flow, gas drag is sufficient to keep the solids circulating. The value of U_{ms} depends on the bed geometry (cone angle, column diameter, inlet diameter), particle properties (density, size and size distribution, shape) and inventory (static bed height), gas properties (density, viscosity) and running condition (temperature, pressure). For processes such as TRISO coating, it is clearly important to maintain gas flows that are greater than U_{ms} so that sufficient solids gas contacting and overall mixing are maintained.

The minimum spouting velocity of conical spouted beds has been extensively measured experimentally, as summarized in Table 2.1. This table lists 25 U_{ms} correlations published for relatively deep conical beds composed of lower density particles. The dimensionless groups used in the correlations include Ar, D_i/D_c, tan(γ), tan(γ/2), sin(γ/2), H_0/D_c, Re_{ms}, where the Archimedes number is defined as:

$$Ar = \frac{d_p{}^3 \rho_p (\rho_p - \rho_g) g}{\mu^2} \qquad (2.1)$$

and the particle Reynolds number at U_{ms} is defined as:

$$\mathrm{Re}_{ms} = \frac{d_p U_{ms} \rho_g}{\mu} \qquad (2.2)$$

It can be observed from these correlations that U_{ms} is proportional to power of particle size, d_p^{n1}, with n1 ranging from 0.54 to 1, which means U_{ms} increases with particle size. U_{ms} is also proportional to the power of the static particle height, H_0^{n2}, with n2 ranging from 0.25 to 1.757, which means U_{ms} increases with static particle height. Also, U_{ms} increases with cone angle.

Silica gel, polymer, grain, sand, glass, coal, aluminum, activated charcoal, fertilizer and ceramics were used to develop these U_{ms} correlations. The particle sizes ranged from 0.5 to 1.035 mm. The density of the particles ranged from 240 to 2986 kg/m^3 (much lower than for TRISO fuel particles, with a density on the order of 10000 kg/m^3), and the particle size range did not extend down to the kernal size for TRISO particles.

Table 2.1 Previous studies of minimum spouting velocity

No.	Year	Author	Correlation	Bed Geometry	Solids used	Type of Spouted bed
1	1955	Mathur and Gishler	$U_{ms} = (\frac{d_p}{D_c})(\frac{D_i}{D_c})^{\frac{1}{3}} \sqrt{\frac{2gH_0(\rho_p - \rho_g)}{\rho_g}}$	γ=85° D_c=15.2cm D_i=0.95cm H_0=63.5cm	Brucite, Mustard seed, rape seeds, peas, wheat, Ottawa sand, Shale d_p= 0.5-3.1mm ρ_p=1.1-2.67g/cm^3	Conical
2	1958	Madonna and Lama	$U_{ms} = k(1-\varepsilon)^{0.5}(\frac{D_i}{D_c})^2 \sqrt{\frac{2gH_0(\rho_p - \rho_g)}{\rho_g}}$	Not specified	Not specified	Conical
3	1964	Gorshtein and Mukhlenov	$\mathrm{Re}_{ms} = 0.174 \frac{(Ar)^{0.5}}{\tan(\frac{\gamma}{2})^{1.25}} (\frac{D_b}{D_i})^{0.85}, \mathrm{Re}_i = \frac{d_p u_i \rho_g}{\mu}$	D_i=1-1.3cm H_0=3-15cm γ=12-60° Dc=5-10cm	Quartz, sand, millet, Aluminum silicate d_p=0.5-2.5mm ρ_p=0.98-2.36g/cm^3	Conical
4	1964	Manurung	$U_{ms} = 7.73(\tan\gamma)^{0.72}(\frac{d_p}{D_c})^{0.62}(\frac{D_i}{D_c})^{0.155\tan\lambda}(H_0 U_m g)^{\frac{1}{3}}$	D_c=15cm D_i=0.9-1.52mm H_0=20-100cm γ=60°	Coal, polystyrene, rape seed, and millet d_p=1-4mm ρ_p=1.09-1.43g/cm^3	Conical
5	1964	Nikolaev and Golubev	$\mathrm{Re}_{ms} = 0.051(Ar)^{0.59}(\frac{D_i}{D_c})^{0.10}(\frac{H_0}{D_c})^{0.25}$	D_c=12cm D_i=2-5cm H_0=9-15cm γ: not given	Spherical particles dp=1.75-5.6mm ρ_p: not available	Conical
6	1964	Smith and Reddy	$U_{ms} = d_p[\frac{g(\rho_p - \rho_g)}{\rho_g D_c}]^{0.5}[0.64 + 26.8(\frac{D_i}{D_c})^2](\frac{H_0}{D_c})^{0.5-1.76\frac{D_i}{D_c}}$	D_c=15cm D_i=0.9-1.9cm H_0=3.3-5.8cm γ=60°	Sand, alundum, crystolon, polystyrene	Conical
7	1965	Ghosh	$U_{ms} = k(\frac{d_p}{D_c})(\frac{D_i}{D_c})^2 \sqrt{\frac{2gH_0(\rho_p - \rho_g)}{\rho_g}}$	Not reported	Not reported	Conical
8	1967	Goltsiker	$\mathrm{Re}_{ms} = 73(Ar)^{0.14}(\frac{\rho_p}{\rho_g})^{0.47}(\frac{H_0}{D_i})^{0.9}$	D_i=0.41-1.23cm H_0=5-31cm γ=26-60°	Fertilizer, silica gel d_p=1-3mm ρ_p=0.8-1.63g/cm^3	Conical

Table 2.1: Continued.

No.	Year	Author	Correlation	Bed Geometry	Solids used	Type of Spouted bed
9	1967	Tsvik *et al.*	$\mathrm{Re}_{ms} = 0.4(Ar)^{0.52}(\frac{H_0}{D_i})^{1.24}(\tan\frac{\gamma}{2})^{0.42}$	D_i=2-4.2cm H_0=10-50cm γ=20-50° Dc=4-29.4cm	Fertilizer d_p=1.5-4mm ρ_p=1.65-1.7g/cm^3	Conical
10	1969	Abdelrazek	$U_{ms} = \frac{1}{1.74}\{(\frac{d_p}{D_c})(\frac{D_i}{D_c})^{\frac{1}{3}}[\frac{2gH(\rho_p-\rho_g)}{\rho_g}]^{0.5} - 0.25\}$	D_c = 5-10cm D_i = 0.4-0.8cm H_0 =5-30cm γ=60°	Glass, steel spheres d_p=0.5-0.8mm ρ_p=2.46 and 7.07g/cm^3	Conical
11	1969	Pallai and Nemeth	$U_{ms} = U_{mf}(\frac{H_0}{1.5H_m}+1)$	D_c = 6cm D_i = 6, 8, 10mm γ=60° Ho=6-12cm	Glass spheres, activated charcoal Dp=1.6=2.5mm Density=0.5 and 2.46g/cm^3	Conical
12	1969	Wan-Fyong *et al.*	$\mathrm{Re}_{ms} = 1.24\,\mathrm{Re}_t(\frac{H_0}{D_i})^{0.82}(\tan\frac{\gamma}{2})^{0.92}$	D_i=2.6-7.6cm H_0=7-30cm γ=10-70° Dc=11.2-20cm	Millet, silica gel, plastics d_p=0.35-4mm ρ_p=0.45-1.39g/cm^3	Conical
13	1970	Gay *et al.*	$U_{ms} = 1.26\times10^7\frac{d_p\rho_b g}{\rho_g}(\frac{H_0}{D_c})^{0.19(\frac{D_i}{D_c})^{1.38}}(\frac{D_i}{D_c})^{5.62}(\frac{\mu^2}{\rho_b\rho_g D_c^{\,3} g})^{0.5}$	D_c=38-61cm D_i=3.8-13.2cm H_0=18-62cm γ=90°	Whole peanuts, 11mm diameter x 23 mm, ρ_b=0.32g/cm^3	Conical
14	1977	Kmiec	$\mathrm{Re}_{ms} = 0.0176(Ar)^{0.714}(\frac{H_0}{D_c})^{1.535}\gamma^{0.714}\varepsilon_{ms}^{\;2.21}$	D_c=8.8, 18cm γ=24.1, 30, 54.9, 60° H_0=50,60cm Di=1.5, 3.5cm	Sand, silica gel,glass d_p=0.875-6.17mm ρ_p=1.29-2.99g/cm^3	Conical
15	1983	Kmiec	$\mathrm{Re}_{ms}^{\;2}[1.75+\frac{150(1-\varepsilon_{ms})}{\mathrm{Re}_{ms}}] = 31.31Ar(\frac{H_0}{D_i})^{1.757}(\frac{D_i}{D_c})^{0.029}(\tan\frac{\gamma}{2})^{2.073}\varepsilon_{ms}^3$	D_c=8.8-90cm H_0=5-51cm γ=24-53° Di=7.1-15cm	Agalit, rape seed, glass, silica gel, sand, Teflon, Turnip seed d_p=0.88-3.7mm ρ_p=0.85-2.99g/cm^3	Conical

Table 2.1: Continued.

No.	Year	Author	Correlation	Bed Geometry	Solids used	Type of Spouted bed
16	1983	Chen and Lam	$U_{ms} = k\varepsilon^{1.5}(\frac{d_p}{D_c})^{0.5}(\frac{D_i}{D_c})^2\sqrt{\frac{2gH_0(\rho_p-\rho_g)}{\rho_g}}$	Not reported	Not reported.	Not specified
17	1983	Markowski and Maminski	$\mathrm{Re}_{ms} = 0.028(Ar)^{0.57}(\frac{D_c}{D_i})^{1.27}(\frac{H_0}{D_c})^{0.48}$	D_c=11-30cm H_0=20-40 γ=37° Di=1.8-5.6cm	Agalit, polypropylene Teflon d_p=3.41-10.35mm ρ_p=1.12-2.38g/cm^3	Conical
18	1984	Fane and Mitchell	$U_{ms} = 2D_c^{1-e^{(-7D_c^2)}}(\frac{d_p}{D_c})(\frac{D_i}{D_c})^{\frac{1}{3}}\sqrt{\frac{2gH_0(\rho_p-\rho_g)}{\rho_g}}$	H_0/D_c=1-2 D_c=14-110cm γ=60° Di/D_c=1/6	Wheat, coffee beans, celcon d_p=2.5-6.5mm ρ_p=1.14-1.37g/cm^3	Conical
19	1992	Choi and Meisen	$U_{ms} = 0.147(\frac{\rho_p-\rho_g}{\rho_g})^{0.477}(\frac{H_0}{D_c})^{0.508}(\frac{d_p}{D_c})^{0.61}(\frac{D_i}{D_c})^{0.243}\sqrt{2gH_0}$	H_0= 24-53cm D_c=24, 45cm γ=60° Di=21-35mm	Polystyrene, PE, poly-formaldehyde d_p=2.16-2.8mm ρ_p=1.05-1.09g/cm^3	Conical
20	1992	Olazar *et al.*	$\mathrm{Re}_{ms} = 0.126Ar^{0.5}(\frac{D_b}{D_i})^{1.68}(\tan\frac{\gamma}{2})^{-0.57}$	D_c=36cm H_0=36-61cm γ=28-45° D_i=3,4,5,6cm	Glass, beans, rice, peas, lentils, ceramics, polystyrene, wood cubes d_p=1-25mm ρ_p=0.24-3.52g/cm^3	Conical
21	1994a	Olazar *et al.*	$U_{ms} = (\frac{d_p}{D_c})(\frac{D_i}{D_c})^{0.1}\sqrt{\frac{2gH_0(\rho_p-\rho_g)}{\rho_g}}$	D_c=15cm γ=150° H_0=16-45cm Di=5, 6cm	Glass, rice, expanded polystyrene d_p=1-8mm ρ_p=1.25-2.42g/cm^3	Conical
22	1995	Rocha *et al.*	$Q_{ms} = 5.92\times10^{-5}(\frac{d_p}{\phi D_c})^{0.05}(\frac{D_i}{D_c})^{-2.6}[\frac{2gH_0(\rho_p-\rho_g)}{\rho_g}](\tan\frac{\gamma}{2})^0$	γ=30-60° D_c=5-8.57cm H_0=5.41-28cm Di: not reported	Inert tablets, d_p=6.49mm Φ=0.857 ρ_p=1.02g/cm^3	Conical
23	1997	Aravinth and Murugesan	$\mathrm{Re}_{ms} = 0.023Ar^{0.63}(\frac{H_0}{D_c})(\frac{D_i}{D_c})^{0.2}(\sin\frac{\gamma}{2})^{0.5}$	D_c=8-90cm γ=24-180 H_0=5-183cm H_0/D_c<1 Di=0.95-5cm	Glass, polymer, grain, Fe-catalyst, sand d_p=0.5-7.8mm ρ_p=0.855-2.96g/cm^3	Conical

Table 2.1: Continued.

No.	Year	Author	Correlation	Bed Geometry	Solids used	Type of Spouted bed
24	1997	Aravinth and Murugesan	$\mathrm{Re}_{ms} = 0.03Ar^{0.63}(\frac{H_0}{D_c})^{0.25}(\frac{D_i}{D_c})^{0.2}(\sin\frac{\gamma}{2})^{-0.2}$	D_c=8-90cm γ=24-180 H_0=5-183cm H_0/D_c>1 Di=0.95-5cm	Glass, polymer, grain, Fe-catalyst, sand d_p=0.5-7.8mm ρ_p=0.85-2.96g/cm^3	Conical
25	1997	Bi *et al.*	$\mathrm{Re}_{ms} = 0.3Ar^{0.5}(1-0.9(\frac{D_i}{D_b})^2)\sqrt{\frac{1}{3}(\frac{D_b}{D_i})[(\frac{D_b}{D_i})^2+(\frac{D_b}{D_i})+1]}$	D_c=8.8-110cm H_0/D_c<1 γ=24-60° Di=1.5-30cm	grain, polymer, sand, glass, silica, d_p=0.88-6.17mm ρ_p=0.85-2.99g/cm^3	Conical

Note: The fluid is air for all cases listed above.

In addition, the majority of these correlations deal with deep spouted beds with H_0/D_c greater than one. The hydrodynamics of deep spouted beds with $H_0/D_c \geq 1$ is quite different from shallow spouted beds with $H_0/D_c \leq 1$ since the particles are constrained in the conical part for shallow beds. For example, the Mathur and Gishler (1955) correlation for deep beds with $H_0/D_c \geq 1$ overestimates U_{ms} in shallow spouted beds [Choi and Meisen, 1992].

One also must consider the basis for defining U_{ms}, because this is not handled consistently in the literature. The early U_{ms} correlations developed by Nikolaev and Golubev (1964), Gorshtein and Mukhlenov (1964), and Tsvik (1967) are defined as the gas velocity at the onset of spouting when gas velocity is increased from low to high (see Figure 2.5(a)). Later, Kmiec (1983) and Olazar *et al.* (1992) use a different approach. They treat the turn point A in Figure 2.5(a) as minimum spouting velocity from which pressure drop starts to become level as gas flow rate is increased from low to high. Pham (1983) specifies point B in Figure 2.5(b) as U_{ms} when gas velocity is decreased from high to low. This latter method is adopted in the experiments used to measure U_{ms} in the present research.

Gas pressure drop has also been widely studied for spouted bed hydrodynamics. One reason for the importance of pressure drop is that it is one of the few hydrodynamics measurements that can be made externally without requiring direct access to the inside of the spouted bed vessel. Such external access is especially relevant to industrial contexts

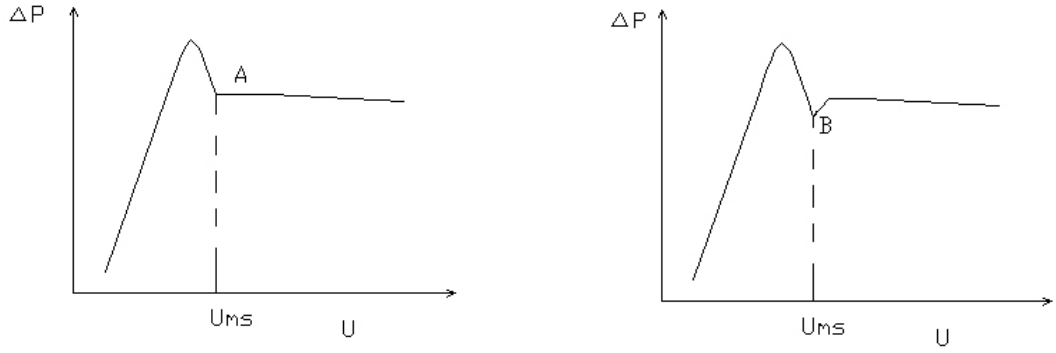

(a) (b)

Figure 2.5 Gas pressure drop *vs*. gas flow rate. (a) Gas flow rate is increased from low to high [Kmiec, 1983]; (b)gas flow rate is decreased from high to low [Pham, 1983].

or situations where external heaters or severe process conditions make internal sensors impractical.

Typically, pressure drop measurements are made between the gas inlet and some reference point at or near the bed outlet. The situation is complicated by the fact that the pulsing action of the global solids flow described above produces relatively large pressure fluctuations that can be readily detected if a fast-response sensor is used. If the latter is available, it becomes also possible to study these fluctuations in addition to the mean pressure drop. Three main approaches are used to analyze pressure drop fluctuations in spouted beds as well as fluidized beds in general: simple statistical analysis, frequency (spectral) analysis, and nonlinear statistical analysis. The last approach is described in detail by Schouten *et al.* (1998) among others.

Once the gas flow exceeds U_{ms}, the average gas pressure drop (ΔP_s) changes little with gas flow rate as indicated in Figure 2.5. Some correlations have been published relating ΔP_s to solids properties and bed dimensions, however, most of these correlations are based on deep spouted beds with a flat base, and very few are for conical spouted beds. Some types of ΔP_s correlations are summarized in Table 2.2.

The two correlations listed in Table 2.2 that apply to conical spouted beds are those proposed by Mukhlenov and Gorshtein (1964) and Olazar *et al.* (1993). Both of these correlations predict that ΔP_s increases with H_0. However, the former shows that ΔP_s increases with cone angle, while the latter shows opposite tendency. The other key dimensionless groups in both correlations are Re_{ms} and the bed height to diameter ratio. Trends in ΔP_s with both of these groups also appear to be inconsistent between these sources.

Table 2.3 summarizes previous studies where the pressure fluctuations of spouted beds were analyzed. Xu *et al*. (2004) analyzed the pressure fluctuations of rectangular conical spouted bed with glass beads and silica gel in both the time and frequency domain. He found that the spouting behavior in deep spouted beds (H_0/D_c=2.9) is significantly different from shallow spouted beds (H_0/D_c=1.5). For the beds Xu studied, the standard deviation of pressure drop fluctuations increased with gas velocity, and skewness exhibited small deviations from that of a normal distribution. He also found that Fourier power spectra of the pressure signals are useful for identifying different flow regimes. In general Xu observed that the pressure fluctuations in shallow spouted beds were rather

Table 2.2 Previous studies of average and maximum gas pressure drop

Year	Author	ΔP_s correlation	Bed geometry	Particles	Bed type
1964	Manu-rung	$\frac{-\Delta P_M}{H(\rho_p-\rho_g)}=[\frac{6.8}{\tan\lambda}(\frac{D_i}{D_c})+0.8]-3.44\frac{d_p}{H}$	D_c=15cm γ=60° d_i = 1.3cm H_0=34-93cm	Coal, polymer, rape seed, millet d_p=1-4mm ρ_p=0.92-1.43g/cm^3	Conical
1964	Mukhlenov and Gorshtein	$-\frac{\Delta P_s}{H_0\rho_b g}=7.68[\tan(\frac{\gamma}{2})]^{0.2}\ \mathrm{Re}_{ms}{}^{-0.2}(\frac{H_0}{D_i})^{-0.33}$	γ=12-60° D_i=1.03-1.29cm H_0=3-15cm Dc= 5cm	Quartz, sand, millet, Aluminum silicate d_p=0.5-2.5mm ρ_p=0.98-2.36g/cm^3	Conical
1965	Malek and Lu	$-\Delta P_M=H(\rho_p-\rho_g)(1-\varepsilon)g$	D_c=15.2cm γ=60° D_i=0.95-3.81cm H_0=28-71cm	Wheat d_p=3.7mm ρ_p=0.83g/cm^3	Conical
1965	Mukhlenov et al.	$\frac{\Delta P_M}{\Delta P_s}=1+6.65(\frac{H}{D_i})^{1.2}\tan(\frac{\gamma}{2})^{0.5}(Ar)^{0.2}$	γ=12-60° D_i=1.03-1.29cm H_0=3-15cm Dc=5cm	Quartz, sand, millet, Aluminum silicate d_p=0.5-2.5mm ρ_p=0.98-2.36g/cm^3	Conical
1968	Mamuro and Hattori	$-\Delta P_S=(\rho_p-\rho_f)(1-\varepsilon_{mf})g(\frac{3}{4}H_m)$	Non-specified	Theoretical model	Conical
1992	Olazar *et al.*	$-\frac{\Delta P_s}{H_0\rho_b g}=1.20[\tan(\frac{\gamma}{2})]^{-0.11}(\mathrm{Re}_i)_{ms}{}^{-0.06}(\frac{H_0}{D_i})^{0.08}$	D_c=36cm γ=28-45° D_i=3-6cm H_0=36-61cm.	Glass, beans, rice, peas, lentils, ceramics, polystyrene, wood cubes d_p=1-25mm ρ_p=0.24-3.52g/cm^3	Conical

Note: The fluid is air for all cases listed above.

Table 2.3 The papers on analysis of spouted bed pressure signal for dynamic content.

No.	Year	Author	Bed geometry	Particles	Bed type	Approach
1	2004	Freitas *et al.*	H_0 = 70cm,L=15cm, W=2.9 and 5.3cm, γ=60°	Glass d_p=1.44mm ρ_p=2.52g/cm^3	Rectangular	Statistics; chaos; frequency
2	2004	Xu *et al.*	H=1.7m,γ=60° D_i=6,10mm Dc=8, 12 cm	Glass, silica gel d_p=1.4-1.9mm ρ_p=0.43-1.53g/cm^3	Conical	Statistics; frequency
3	2005	Zhong and Zhang	H=2m, L = 0.3m, W=0.03m. γ=60°,H_0=0.2-0.5m	Polystyrene d_p=2.5-3.0mm ρ_p=1.018g/cm^3	Rectangular	ARM power spectrum analysis; frequency

Note: The fluid is air for all cases listed above.

random while those in deep spouted beds showed strong periodic behavior. The shallow spouted beds exhibited a wide range of frequencies from 0 to 20 Hz and did not have a distinct dominant frequency, while the deep beds had a sharp dominant frequency from 6 to 8 Hz depending on particle properties, gas velocity and bed geometry.

Zhong and Zhang (2005) investigated the pressure fluctuation frequency characteristics of a two-dimensional deep spouted bed with polystyrene particles. Their results indicated that the main frequency increased with gas flow rate and decreased with bed depth. Freitas *et al.* (2004) also used pressure fluctuations to identify the flow regimes in slot-rectangular spouted beds with glass beads. van der Schaaf *et al.* (2004) showed the similarity between chaos analysis and frequency analysis of pressure fluctuations in fluidized beds with sand particles. Svoboda *et al.* (1983) studied the pressure fluctuations in gas-fluidized beds at elevated temperatures and indicated that the frequency spectrum, dominant frequency and mean pressure depend considerably on the gas flow rate and temperature.

The references in Table 2.3 indicate that the pressure fluctuation signal should be very useful for characterizing the behavior of spouted beds, including the TRISO fuel coaters. Clearly the characteristics of the pressure fluctuation strongly depend on the spouted or fluidized bed structure, particle species, particle diameters and operating conditions, including temperature, pressure and gas flow rate. As far as TRISO fuel coating is concerned, the missing component in the current literature is the lack of studies with shallow spouted beds and dense particles. The nature of the dynamics depicted in the

literature is also somewhat ambiguous and system specific, with no development of a more general understanding of the physical processes that produce the observed dynamics. These missing components in the literature are a chief motivation for the present study.

Previous studies of spouted bed fountain height are summarized in Table 2.4. As explained earlier, the reported values of fountain height are typically based on time average measurements, even though the pulsations described previously are also present in the fountain zone. Grace and Mathur (1978) give a theoretical model-based correlation for the fountain height H_f:

$$H_f = (\varepsilon_{SH})^{1.46} \frac{v_{SH\max}^2}{2g} \left(\frac{\rho_p}{\rho_p - \rho_g}\right) \tag{2.3}$$

This correlation requires knowledge of the void fraction and the central particle velocity at the top of the spout, both of which are usually unavailable in the initial design stage.

Day (1990) published the following correlation for predicting the average fountain height:

$$\frac{H_f}{D_i} = 46.4\left(\frac{U}{U_{ms}} - 1\right)^{0.865} \left(\frac{H_0}{H_m}\right)^{-0.379} A^{2.13} \left(\frac{\rho_p - \rho_g}{\rho_g}\right)^{-0.892} \left(\frac{d_p}{D_i}\right)^{-3.49} \left(\frac{D_i}{D_c}\right)^{-2.75} \tag{2.4}$$

This correlation requires one to know H_m, the maximum spoutable height. Some authors report how to predict maximum spoutable bed height in deep spouted beds with light particles, such as Morgan and Littman (1982), Rao and Husain (1985), and Cecen (1994). However, H_m is not appropriate for shallow spouted beds, because the particles are still spoutable even at highest H value ($H=D_c$).

Table 2.4 The average fountain height

Year	Author	H_f correlation	Bed geometry	Particles	Bed type
1978	Grace and Mathur	$H_f = (\varepsilon_{SH})^{1.46} \frac{v_{SH\max}^2}{2g} (\frac{\rho_s}{\rho_s - \rho_g})$	Theoretical model	Not specified	Conical
1990	Day	$\frac{H_f}{D_i} = 46.4(\frac{U}{U_{ms}} - 1)^{0.865} (\frac{H_0}{H_m})^{-0.379} A^{2.13} (\frac{\rho_s - \rho_f}{\rho_f})^{-0.892} (\frac{d_p}{D_i})^{-3.49} (\frac{D_i}{D_c})^{-2.75}$	D_c=15.2, 24.1, 29.2cm Di=25.4, 38.1mm H_0= 15.2-87.6cm (H_0/D_c=1-3)	Glass, polymer d_p=1.1-3.5mm ρ_p=1.05-2.96g/cm^3	Flat
2005b	San José *et al.*	$H_f = 0.01\gamma^{-0.14} (\frac{D_i}{D_b})^{-1.14} (\frac{d_p}{D_i})^{-0.83} (\frac{H_0}{D_i})^{-0.52} (\frac{u}{U_{ms}})^{4.8} \rho_s^{-0.12} \Phi^{-1.45}$	D_c=36cm γ=28-45° D_i=3-5cm H_0=5-35cm	polymer D_p=1-3.5mm ρ_p=0.07-1.03g/cm^3	Conical

Perhaps the most relevant correlation to the present study found in the literature for spouted bed fountain height was that by San José *et al.* (2005b). They developed the following correlation to predict the average fountain height of polymer particles in conical spouted bed:

$$H_f = 0.0101\gamma^{-0.14}\left(\frac{D_i}{D_b}\right)^{-1.14}\left(\frac{d_p}{D_i}\right)^{-0.83}\left(\frac{H_0}{D_i}\right)^{-0.52}\left(\frac{u}{U_{ms}}\right)^{4.8}\rho_p{}^{-0.12}\Phi^{-1.45} \qquad (2.5)$$

where Φ is particle sphericity and ρ_p is the particle density.

The experiments from which this correlation was produced utilized polymer particles of 1-25 mm diameter in a conical spouted bed with D_c=36 cm, γ=28-45°, H_0=5-35 cm and D_i=3-6 cm. Based on the relative magnitudes of the exponents in this correlation, it appears that gas velocity is the dominant factor.

No previous study of spouted fountain height was found for which the range of bed height and particle density extended to that of TRISO fuel particle coating.

Spouted gas velocity profiles reveal how the inlet flowing gas redistributes itself as it flows upward from the inlet. In particular such measurements reveal how the gas flows outward radially from the spout zone into the annular zone. In addition to changing the shape of these two zones, the outward gas flow can significantly affect gas-solid contact patterns. Generally, gas velocity profiles have been measured with two basic methods [Mathur, 1974b]. One is to use pitot tube that is inserted from the above down into solids fountain, spout, or annulus. The shortcoming of this method is that the pitot tube can disturb the

local voidage and give inaccurate measurements at the bottom of the conical spouted bed where the sectional area of the cone is small. Another much less accurate method is to measure the longitudinal static pressure gradients at the column wall. In general this latter method is not suitable for shallow conical spouted beds such as those of interest here.

Table 2.5 summarizes the previous studies of gas velocity profiles found in the literature. Thorley *et al.* (1955) used the wall method to measure gas velocity profiles of wheat in the column part of a deep conical spouted bed with 61 cm diameter column, 45-85° cone angle and H_0/D_c = 1.5~3. They found that the gas velocity in the spout zone is much higher than the gas velocity in the annular zone, and that 37%-61% gas leaked into annular zone at z/H_0= 0.5. This leakage ratio decreased as gas velocity, inlet diameter, or cone angle increased. These results can probably not be applied to shallow spouted beds because the gas velocity obtained by Thorley *et al.* is for the constant diameter portion above the conical part.

Becker (1961), Mamuro and Hattori (1968) and van Velzen *et al.* (1972) used a pitot tube to measure gas velocity profiles in conical spouted beds. They also found that cross flow of gas from the spout into the annulus increases with smaller cone angle, larger size of inlet, shallower bed and low gas flow rate. At higher gas flow rate, most of the additional gas flows through spout zone. So the ratio of gas leakage from spout zone into annular zone varies with bed geometry and process parameter.

Olazar *et al.* (1995a) measured gas velocity of expanded polystyrene in a conical spouted

Table 2.5 References on gas velocity profile

No	Year	Author	Bed geometry	Particle	Bed type
1	1955	Thorley *et al.*	D_c=61cm H_0=91-185cm γ=45-85° D_i=5.08-10.16cm	Wheat d_p=3.7mm ρ_p=0.83g/cm^3	conical
2	1959	Thorley *et al.*	D_c=15.2, 30.48, 60.96cm D_i=1.3-5cm γ=60°	Wheat d_p=3.7mm ρ_p=0.83g/cm^3	conical
3	1961	Becker	D_c=15.2, 61cm $H_0 = H_m$ D_i=0.1-15.2cm γ=90, 120, 180°	corn, peas, barkley, wheat, rape seed, Ottawa seed d_p=0.8-6.9mm ρ_p=0.83-2.655g/cm^3	conical and flat
4	1968	Mamuro and Hattori	D_c=15.2cm D_i=1.3cm γ=180°	millet, polystyrene, coal d_p=1.3-1.8mm ρ_p=0.655-0.768g/cm^3	flat
5	1972	van Velzen *et al.*	D_c=12.5cm H_0=20cm γ=31° D_i = 2.5-8cm	Glass, polymer, Zirconium oxide d_p=0.5-1.3mm ρ_p=1-4.4g/cm^3	conical
6	1994b	Olazar *et al.*	D_c=36cm D_i=3-5cm H_0=36-60cm γ=28-45°	Glass d_p=1-8mm ρ_p=2.42g/cm^3	conical
7	1995a	Olazar *et al.*	D_c=36cm D_i=5cm H_0=28cm γ=45°	Expanded polystyrene d_p=3.5mm ρ_p=0.014g/cm^3	conical

bed and correlated maximum gas velocity in terms of axial height as below:

$$\overline{u_M} = 3.76e^{-10.27z} \qquad (2.6)$$

where z is the axial height from the gas inlet and its unit is meter.

In addition to experimental investigations of the hydrodynamics of the spouted beds, some attempts have also been made to develop detailed computational models of spouted bed dynamics. Relevant publications on spouted hydrodynamics modeling are summarized in Table 2.5. These publications are divided into two basic classes: discrete element method (DEM) models and computational fluid dynamics (CFD) models. In DEM, the trajectory of each individual particle at each time step. Gas-solid drag is evaluated for each particle based on local conditions, and particle-particle and particle-wall collisions are treated based on explicit Newtonian mechanics and rules for handling elastic/inelastic effects. Prominent DEM models include those by Tsuji *et al.* (1993), Limtrakul *et al.* (2004), Takeuchi *et al.* (2004) and Zhong *et al.* (2006).

CFD models treat gas and solid particles both as continuous but distinct fluid phases (with the particles acting as a pseudo-fluid), such as the model by Lu *et al.* (2004). Using a general CFD model for fluidization created originally at the National Energy Technology Laboratory (NETL), ORNL has developed a detailed model for simulating the shallow conical spouted bed for nuclear fuel coating [Pannala, 2005c]. This model currently appears to be the best approach available for capturing all of the details of potential TRISO coater designs, and compared to DEM methods, it is expected to be computationally much faster. However, even though CFD methods are much faster than

DEM, they are still very computationally demanding and require access to high performance computing facilities. Even with the latter, simulations of individual cases can take days to complete with the fastest computers available. Output from such simulations can also be very large, requiring the processing of many gigabytes of data. Interpretation of such large amounts of data requires specialized expertise and considerable effort.

Because both DEM and CFD models are so computationally intensive, other simpler approaches are needed, especially for situations where rapid results are required such as with on-line diagnostics and controls. Unfortunately, any previous development of low-order dynamic models for spouted beds in the literature has not been found so far. However, some hints about how to begin development of such models might be obtained from two published low-order models for bubbling fluidized beds. One model proposed by Pannala, Daw and Halow (2003) explicitly deals with the behavior of void pockets (bubbles) as these pockets rise through bubbling bed reactors. This model focuses on the number, position, and motion of the bubbles as they evolve with time. Interaction between bubbles includes wake effects from leading bubbles and bubble coalescence, both of which are defined by explicit deterministic rules expressed as ordinary differential equations (ODEs). The number of ODEs is sufficiently small that the model runs in near-real-time on a desktop computer. Mass transfer and first-order reactions between gas and solids are included, and the model can capture both the dynamics of the bubble and solid interactions as well as the effects of simple chemical reactions. Simulation results from this model have been shown to match closely with experimental

results for ozone bubbling bed reactors [Fryer and Potter, 1976]. This model appears to be relevant to shallow spouted beds, because the pulsating void pockets observed in the spout zone in the present study (described in following sections) seem to be very similar to the incipient bubbles that form in very shallow bubbling beds.

Another low-order model for shallow bubbling bed dynamics was proposed by Sierra, Tadrist, and Occelli (2006) based on previous models proposed by Broadhurst (1986) and Schouten *et al.* (1992). It is a one-dimensional numerical model that utilizes an Eulerian-Lagrangian approach for treating the interaction of a chain of particles in an upflowing gas stream. In this case, a series of ODEs is developed to represent the position and velocity of each particle. A modified hard-sphere model with a normal coefficient of restitution $0 < e < 1$ is used to account for the collisions between particles. For fluid phase, mass and momentum conservation are also taken into account. By integrating the ODEs, particle oscillation frequencies are predicted that closely match the dominant frequency of shallow bubbling bed well. This prediction result is encouraging for spouted beds because the resulting frequencies are very similar to those seen in the spouted beds studied here. Also, it appears that the assumptions used to construct this type of model are reasonably close to what one might use to model the entrainment zone of shallow spouted beds.

3. Approach

The general approach followed in the present study involved three key steps:

- Experimental measurements of an ambient-temperature, conical spouted bed;
- Analysis and correlation of the experimental observations; and
- Development of a low-order dynamic spouted bed model.

Since the AGR fuel coating process specifically utilizes shallow, spouted-bed reactors for coating the dense fuel particles, improving the design and operation of this process requires a good understanding of the hydrodynamics of shallow spouted beds of heavy particles. However, as described in the previous chapter, the studies available in the literature do not cover the appropriate combination of bed depth, particle size, and particle density. In addition, some of the results from the previous studies appear contradictory or inconsistent at best, and there is a clear general shortage of information about the time-varying behavior of spouted beds in the current literature. Thus the first key step of the present study was to develop basic hydrodynamics and time-varying information for conditions and parameter ranges closer to those in TRISO fuel coating.

The objective of generating better hydrodynamical information for TRISO fuel coating was accomplished by carrying out a series of laboratory experiments with an atmospheric, ambient-temperature mock-up of the 5-cm diameter conical spouted bed utilized in the ORNL coater development studies [Pannala *et al*., 2004]. Dense surrogate particles made from ZrO_2 were used in place of actual nuclear fuel for obvious safety reasons. While such ambient experiments with surrogate particles clearly cannot fully represent the actual process hydrodynamics, it is reasonable to expect that the behavior of this

experimental setup with the same bed dimensions and bed depth, and similar particle properties was much closer to the actual process than any of the previous studies. In addition, having experiments at ambient temperature and pressure with no reaction made it much more practical to make both optical (video-based) and intrusive pitot probe measurements of the behavior compared to the actual process. Obviously, the effects of the high temperature and reacting conditions in the real AGR coater will need to be the subject of future studies.

The next major step of the present study was to analyze the information from the experiments to develop engineering correlations and an improved quantitative understanding of the dynamical trends for spouted beds like the AGR coater. The new correlations developed included relationships among minimum spouting velocity, average bed pressure drop, and average fountain height as functions of particle properties and flow conditions. Internal time-average gas velocity profiles measured with a pitot probe were compared with those reported by others and also with detailed CFD modeling results for the ORNL coater. The insights provided by the velocity profiles were also useful in constructing assumptions for a low-order dynamical model. Key information regarding explicit time-varying features of the experimental spouted bed was extracted by analyzing dynamic, high-speed pressure-drop measurements.

The final major step of the present study was to lay the groundwork for a low-order dynamical model of shallow, conical spouted beds similar to that studied in the experiments. As described in the previous chapter, the DEM and CFD models of spouted

beds are not suitable for online monitoring and control because of the intensive computational demand. In addition, it is extremely challenging to resolve the essential physics of the collective particle behavior from the huge amount of detailed information produced by CFD and DEM simulations. Inspired by the success of low-order models for bubbling beds, a low-order dynamic model of shallow, conical spouted beds was constructed by making a coarse-grain approximation of the spouted bed. The coarse-graining process involved dividing the bed into a small number of discrete zones and then applying differential mass and momentum balances over each zone. The result of these balances was a small set of ODEs describing the time rate of change of particle concentrations and velocity in each zone. This group of ODEs was then integrated for a range of parameters with appropriate boundary conditions. Both time-average and dynamical trends were then observed and compared with the experimental measurements and limited results from more detailed CFD models

The detailed methods and results for each of the above steps are now discussed in the remaining sections.

4. Experimental Apparatus and Methods

The safety issues associated with nuclear fuels made it necessary to use surrogate particles in the present experimental study. The surrogate material of choice was yttrium-stabilized zirconia (YSZ or ZrO_2) grinding media because of its high density and the high sphericity of the available particles. Both of the latter are important characteristics for matching the behavior of nuclear fuels in the spouted bed coater. Table 4.1 and 4.2 summarize the general physical properties of the ZrO_2 particles used as well as the experimentally measured and estimated minimum fluidizing velocities.

Minimum fluidizing velocity (U_{mf}) is a standard particle characteristic used for correlating and modeling fluidization behavior. The minimum fluidization velocity of each zirconia particle size was measured using a simple fluidized bed apparatus constructed from a Buchner funnel shown schematically in Fig. 4.1. The Buchner funnel was manufactured by Sibata (model 1311-11250A) and had a flat glass filter frit with

Table 4.1 Summary of ZrO_2 particle properties

Molecular mass	123.22g/mol
Appearance	white
Particle Density	5,890kg/m^3
Particle sphericity	≈1
Diameter range(mm)	0.3, 0.4, 0.5, 0.65
Bulk void fraction	0.42- 0.46
Hardness -Knoop (GPa)	10-15
Youngs modulus (GPa)	100-205

Table 4.2 Measured and predicted U_{mf} and predicted U_t of ZrO_2 particles

Particle size (mm)	Measured U_{mf} (cm/s)	U_{mf} from Wen-Yu correlation (cm/s)	U_t (m/s)
0.3	17.6	16	3.98
0.4	22.5	26.9	5.27
0.5	37.9	39	6.48
0.65	58.7	57.5	8.2

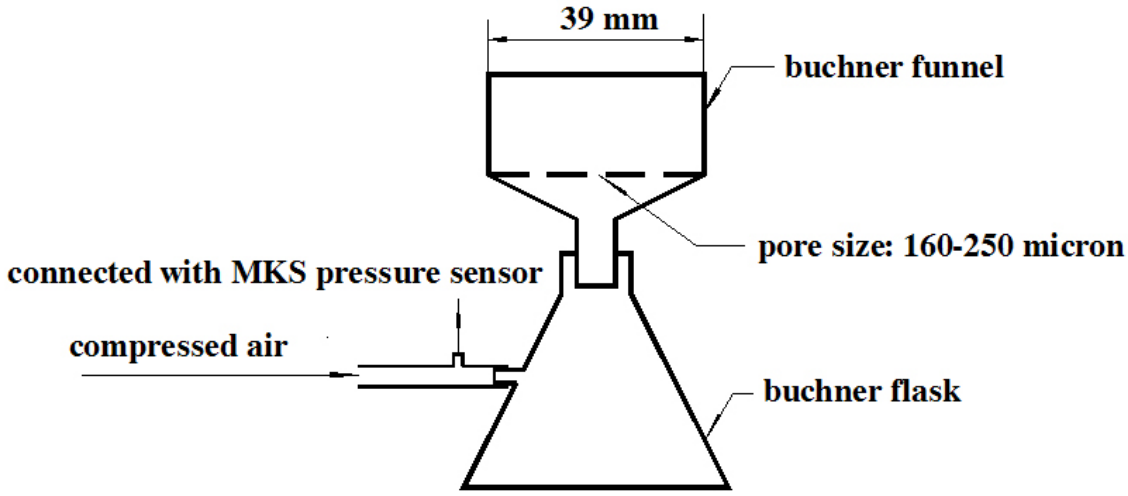

Figure 4.1 Schematic drawing of the Buchner funnel apparatus used to measure U_{mf}.

160-250 micron pores as the filter medium. To begin the measurement, particles of the chosen size were added to the top of the funnel to a static bed height of 3 cm. Compressed air (from the humidified air system described below) was introduced as the fluidizing medium through the Buchner funnel outlet and was metered with a simple manually operated rotameter. Air flow was first raised to achieve a full fluidized condition and then lowered in small increments as average pressure drop across the frit plate was measured with a MKS Baratron pressure transducer (described below) connected to a National Instrument (NI) PXI 6052E data acquisition card driven by NI computer (described below).

As shown in Fig. 4.2, gas pressure drop decreased smoothly until the minimum fluidizing

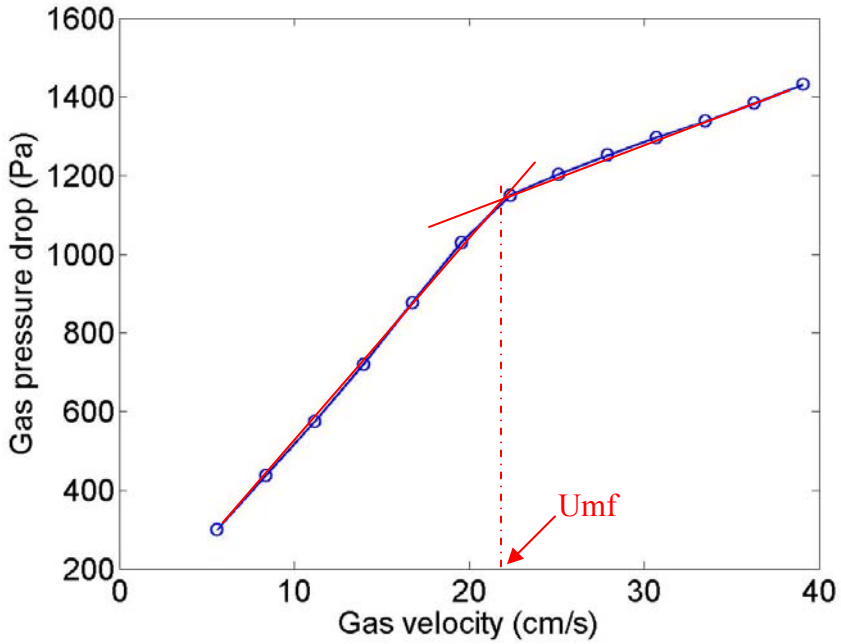

Figure 4.2 Measurement of U_{mf} of 400μm ZrO_2 particles.

condition was reached, at which point it more sharply decreased for further flow reductions. By noting the characteristic breakpoint in the pressure drop curve, the minimum fluidizing air flow was determined. The mean gas velocity in the upper (39-mm diameter) section at this sharp transition point defines the minimum fluidization velocity.

The standard gas used for all spouted bed experiments was room-temperature, humidity-controlled air. Figure 4.3 schematically illustrates the air supply system. High-pressure compressed air was filtered and then metered through a 200 standard liter per minute (0.2 m^3/min) MKS mass flow controller (MFC) (model MKS 1559A-200L). The MFC was controlled by the NI computer via analog output ports on the NI card (described above). To ensure accuracy, the MFC was periodically calibrated with a standardized DryCal air flow meter (model no. DCL-H) manufactured by Bios International Corporation.

After passing through the MFC, the air was temporarily split into two parts. One part of the air passed through a rotameter (used for controlling the flow split) and a humidifier before recombining with the remaining part of air and flowing on to the spouted bed inlet. The humidifier consisted of a sealed plastic column containing 30-cm depth of room-temperature water. By adjusting the ratio of two parts of air, it was possible to control the final humidity of the air flowing into the spouted bed inlet to between 30 and 40% relative humidity. Humidification was necessary to reduce the static electricity generated during bed operation.

Initial experiments intended to provide qualitative visual observations of the spouted bed

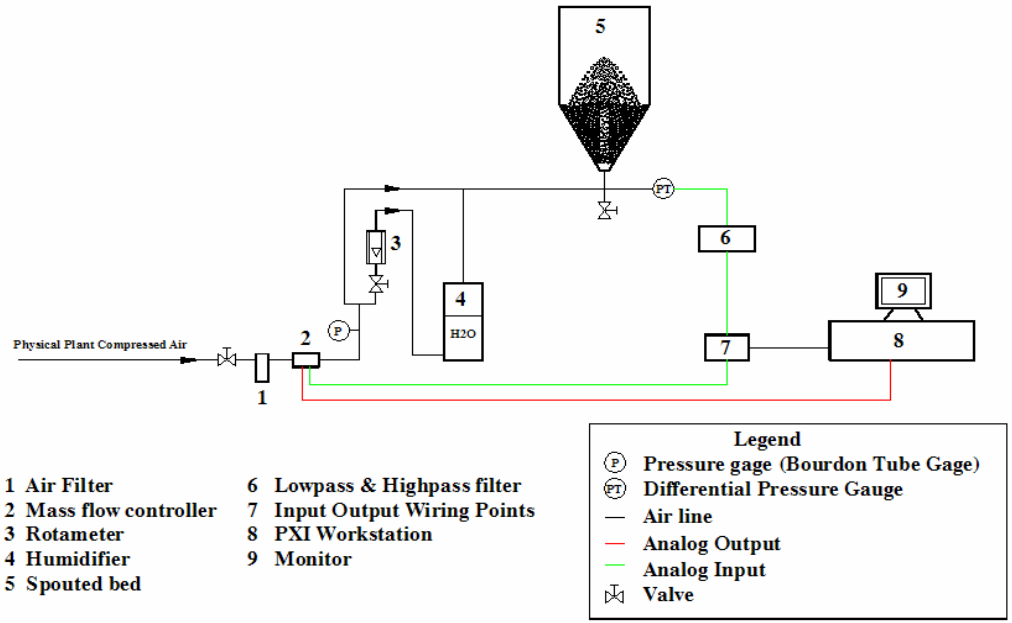

Figure 4.3 Spouted bed process and instrumentation diagram for high-speed differential pressure measurement.

behavior were conducted with a glass mock-up of the 5-cm (2 inch) diameter, 60° conical spouted bed used at ORNL for laboratory coating studies. A schematic of this bed is shown in Fig. 4.4 and a photograph of the experimental setup is shown in Fig. 4.5.

The transparent glass construction of this bed made it possible to visualize the collective motion of the spout and the motion of individual particles at the walls and in the particle entrainment zone. This visual access was important for both helping to interpret the more quantitative measurements made later (as described below) and in developing the key assumptions used in the low-order dynamic model. Visual observations and video recordings using conventional video (nominal 30 frames/s) were made of the glass spouted bed as it was operated over a range of particle sizes, solids inventories (bed depths) and gas flow rates.

Also, a limited number of measurements were made with the laser beam illustrated in Fig. 4.4. The laser was a standard randomly polarized He-Ne laser (Aerotech model LS5R) with 25 mW maximum power. The beam detector was constructed on-site at the university by Dennis Higdon of the Mechanical, Aerospace, and Biomedical Engineering Department. The sensing cell was constructed from a red, super-bright LED. Dark plastic film was placed across the lens of the LED to prevent the sensor from saturating.

This laser-detector combination provided a way to directly measure the large-scale motion of the solid particles at various locations, including the upper (spout), middle (annulus), and lower (inlet) zones of the bed. Since particle fluctuations typically

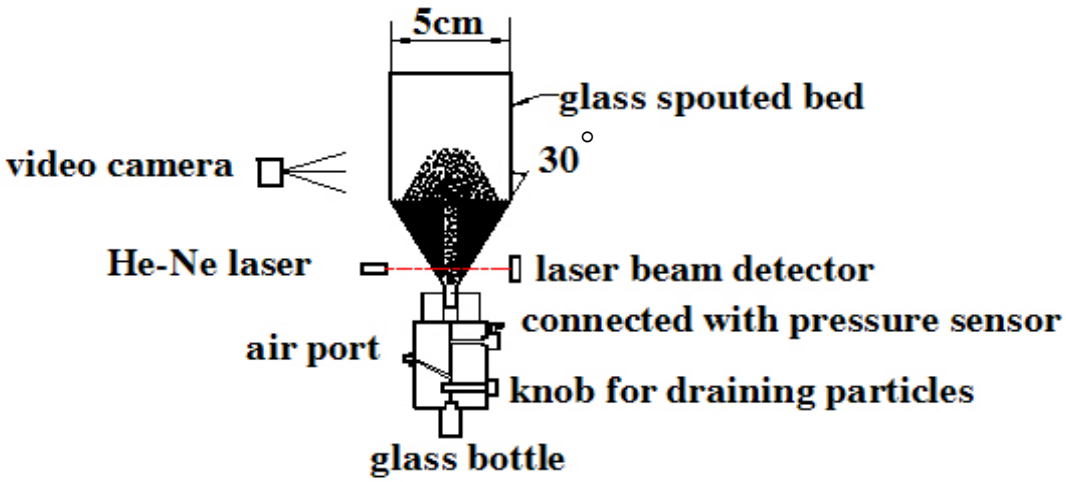

Figure 4.4 Schematic drawing of the glass spouted bed apparatus showing the air distributor, laser beam, and video camera arrangement.

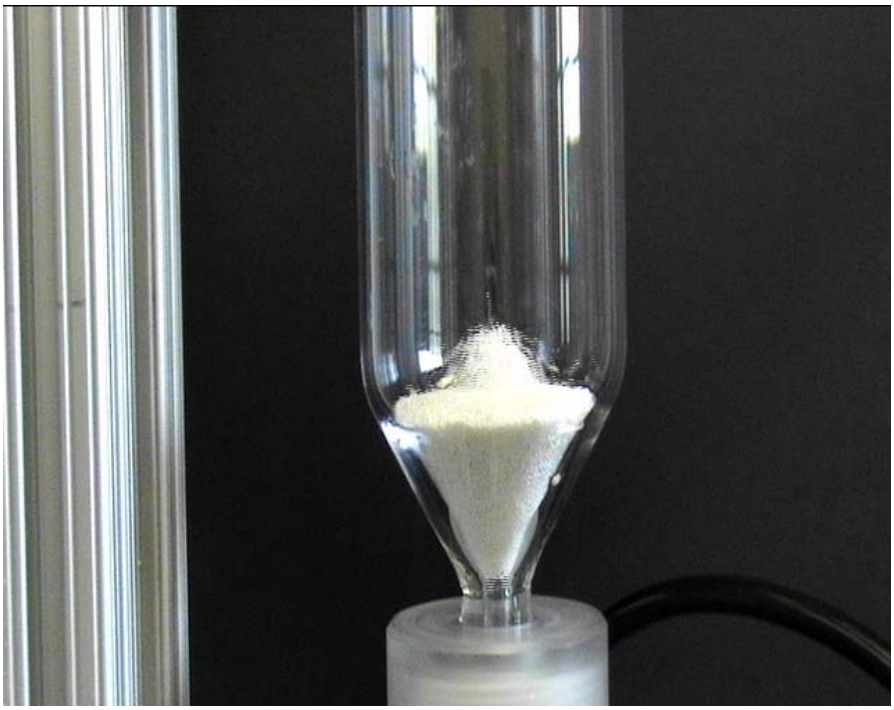

Figure 4.5 Glass spouted bed setup operating with 54.5 grams of 0.65mm of ZrO_2.

happened faster than could be observed directly by eye, these simple measurements made it possible to confirm that the motion of the spout and particles in the cone correlated directly with the pulsations in the pressure measurements made in the gas inlet tube. As described in the following chapter, it was confirmed that the inlet gas pressure measurements contain key information about the solids circulation process.

While useful in providing basic insights into the spouted bed behavior, the glass bed was found to suffer from significant construction imperfections that made it unsuitable for generating more quantitative information. More specifically, the glass blowing process created irregularities in the cone shape that caused obvious asymmetries in the gas and particle flow. Consultations with glass blowing experts indicated that this irregularity would be extremely difficult to overcome (while still maintaining sufficient transparency), so it was decided to build another bed section from more easily machined materials. The material of choice for the cone was aluminum, both because of its ease of machining and its electrical conductivity, which helped disperse static charge. Three different bottom cones were constructed with base cone angles of 45, 60 and 75°, as shown in Fig. 4.6. All three cones came to the same maximum inside diameter of 5 cm and had a 0.4-cm-diameter gas inlet tube.

When assembled, the cones were mounted on a specially machined block of polymethyl methacrylate (PMMA or “acrylic”), which acted as the air distributor and contained the inlet air tube, a side pressure tap, and a special seal arrangement that secured the connection to the bottom of the cone. Figure 4.7 illustrates the acrylic block with key

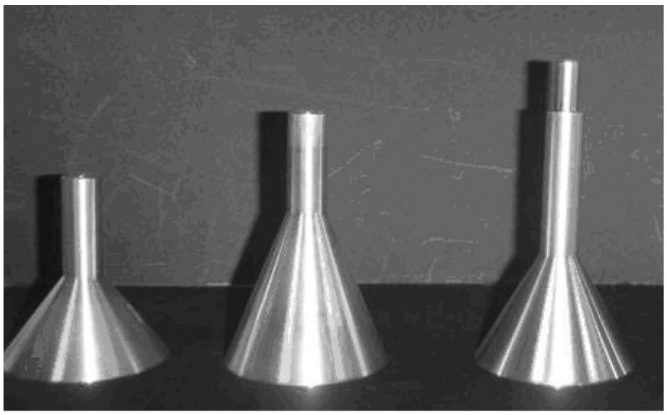

Figure 4.6. The aluminum cones with 75, 60 and 45° base angle (left to right) constructed for the quantitative spouted bed experiments.

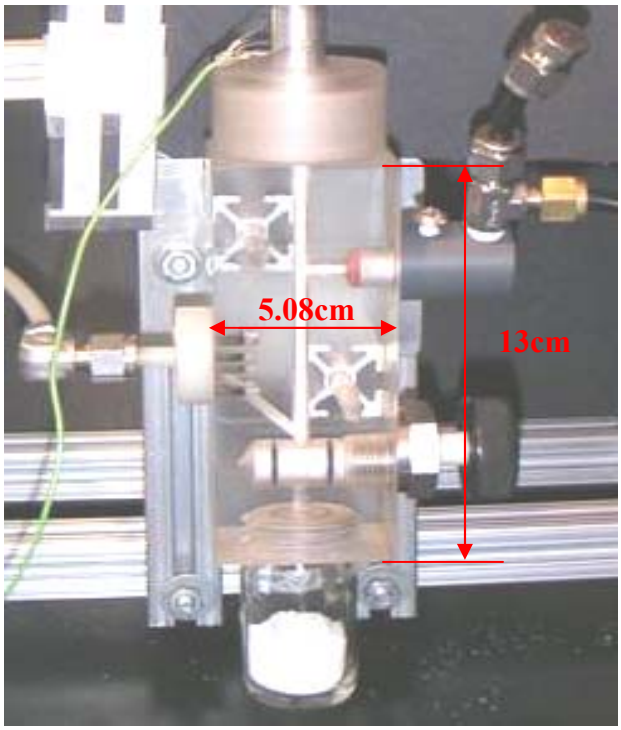

Figure 4.7 The acrylic block used to mount spouted bed, connect pressure sensor and gas pipe, drain particles.

features and dimensions noted.

The upper section of the spouted bed was made of a 5-cm-diameter, transparent quartz cylinder, which still allowed optical observation of the upper portion of the bed during operation. As shown in Figure 4.8, the spouted bed components were assembled in a specially designed, extruded aluminum frame. The bottom was connected to a special T-valve (e in Figure 4.8) which allowed gas flow in or particles to be discharged. A side tap (b in Figure 4.8) connected with one of three MKS pressure transducers, models 223BD-00001AAB (0-133 Pa), 78444-1E (0-1333Pa), and 78444-2B (0-13332Pa)). The specific transducer used depended on the amplitude of the pressure fluctuations. The low-pressure side of each transducer was left open to atmosphere. In order to reduce static electricity, the aluminum cone and all metal parts were grounded. Figure 4.9 shows the bed in operation.

Pressure signals from the MKS transducers were digitized and recorded with a computerized data acquisition system. Signals were first passed through sequential, 4-pole, analog, high- and low-pass Butterworth filters (Wavetek Dual Hi/Lo Filter 452), which were typically set at cut-off frequencies of 0.1 and 100Hz, respectively. After filtering, the signals were digitized at 16-bit maximum resolution with a National Instruments NI PXI-6052E data acquisition card installed in a desktop microcomputer driven by LabVIEW 7.1 software. A special program was written in LabVIEW 7.1 programming code to control the acquisition of both the pressure and video signals.

Typically, the pressure time series was recorded at 1000 Hz for one to two minutes.

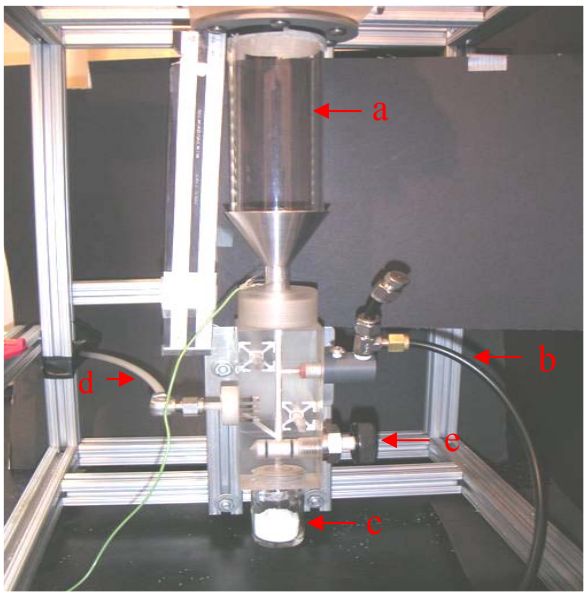

Figure 4.8. Spouted bed assembled with the 75° cone. Air flow is currently off. The label **a** refers to the cylindrical upper portion of the spouted bed; **b** is the pipe connecting with pressure sensor; **c** is ZrO_2 particles that have been discharged from the bed, **d** is the inlet air line and e is T-valve.

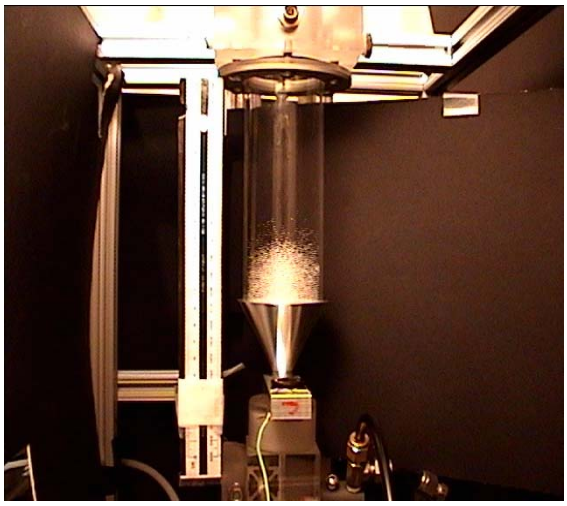

Figure 4.9. The spouted bed with a γ=60° cone installed in operation**.**

In order to further reduce 60 Hz noise coming from power supplies, an isolation amplifier was installed before each piece of electrical equipment.

The standard procedure for a typical experiment involved the following sequence of initial steps:

- Energizing and warming-up of the MFC for at least 30 minutes;
- Start-up and warming of the computer and data acquisition system for 30 minutes;
- Inspection of the pressure sensor line and testing of the instrument's zero reading;
- Inspection of the system grounding (for static charge dissipation);
- And confirmation of bed vertical plumb.

Once the above steps were taken, the T-valve at the bottom of the apparatus was opened to let in a minimum air flow and particles added from above the bed via a funnel (note that without air the particles would immediately fall through the gas inlet into the discharge zone). Air flow rate was then adjusted to the specified value using the MFC. During each experiment the air split to the humidifier was adjusted to maintain a final relative humidity in the bed between 30~40%, as measured in the bed exit with an electronic hygrometer. Ambient temperature always fell in the range 20-26°C. When experimental measurements were completed, air flow was shut off and the particles were allowed to drain to the discharge point.

Experimental determination of minimum spouting velocity was carried out by means of measuring the inlet air pressure relative to atmosphere as a function of air flow rate. Air

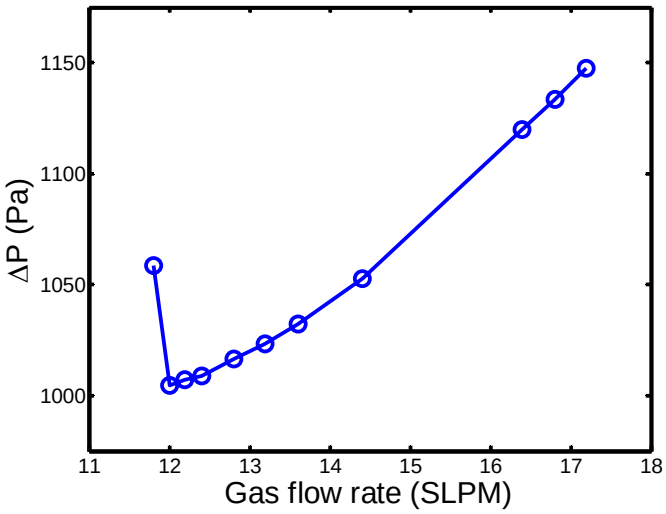

Figure 4.10. Example plot used to determine U_{ms}. In this case, there were 53.9 grams 0.5mm ZrO_2 in a 60° cone.

flow was first raised to achieve a full spouting condition and then lowered in small increments. As shown in Fig. 4.10, gas pressure drop decreases smoothly until the minimum spouting condition is reached, at which point it sharply increases for further flow reductions. The gas inlet velocity (defined in terms of the inlet tube cross section) at this sharp transition point defined the minimum spouting velocity.

Average gas velocity profiles in the bed during spouting were obtained by use of a pitot tube, which is illustrated schematically in Figure 4.11. The pitot tube was composed of inner and outer stainless steel tubes that had normal and opposed-flow openings to the external gas flow, respectively. By measuring the pressure difference between the total gas pressure (P_{total}) and static pressure (P_{static}) of the gas, the dynamic pressure is obtained

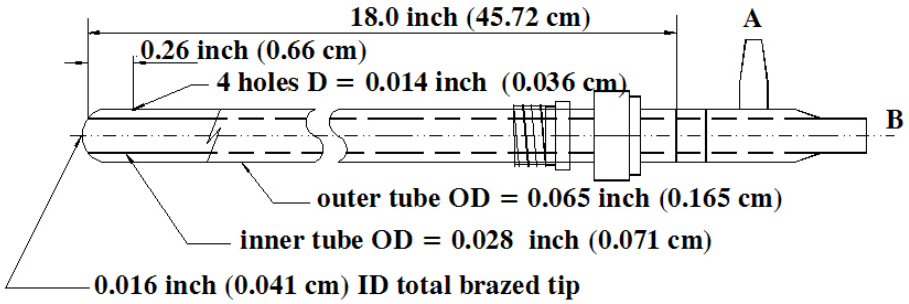

Notes: D: diameter; ID: inner diameter; OD: outer diameter
material: stainless steel
A and B: connect to pressure sensor

Figure 4.11 Schematic of the pitot tube used for velocity profile measurements. D refers to diameter; OD is outer diameter; ID is inner diameter. All tubes were made of stainless steel.

from Bernoulli's equation [White, 2003].

$$u = \sqrt{\frac{2(P_{total} - P_{static})}{\rho_f}} \qquad (4.1)$$

The pitot tube was mounted above the bed with two orthogonal micrometers such that both the x and y horizontal positions could be set very precisely. A vertical clamp allowed manual adjustment in the vertical direction. The precise vertical position was established by measuring the distance between the tip of pitot tube and bottom of the bed. Note that the pitot tube openings and volumes were such that the static-dynamic pressure differential took several seconds to stabilize once the tube was positioned at the desired location. This 'filtering' effect meant that the velocities obtained represented only time average flows. Short-time scale velocities (i.e., turbulent fluctuations) can not typically

be obtained from measurements such as this.

Time-average fountain height for different spouting conditions was determined optically. Video recordings of the upper portion of the spout (above the aluminum cone) were captured using a Sony digital video camera (model DCR-HC42) for 30 seconds. The video recordings were captured electronically on the camera and then extracted as standard video files. Sets of 30 randomly selected frames from the video files were then superposed to create a composite image of the time-average fountain. This composite image was then used to determine the fountain characteristics. Figure 4.12 shows a typical example of the composite image.

Computer processing of the composite image in terms of gray scale variations allowed the determination of an unambiguous fountain height as shown in Fig. 4.13. For purposes of this study fountain height was defined along the centerline of the umbrella shape on the composite image.

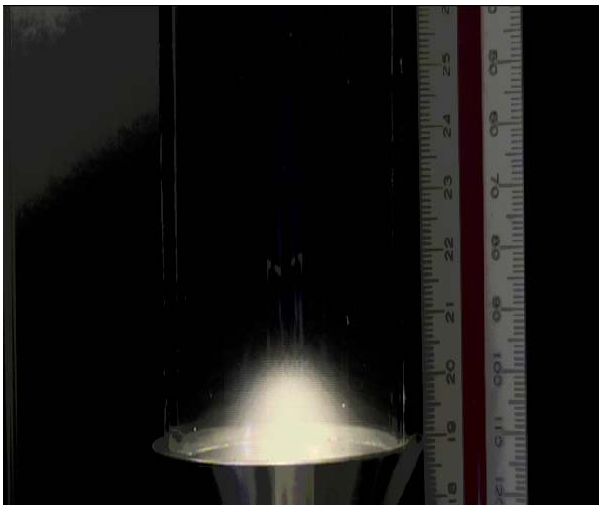

Figure 4.12. A composite image for the spouting condition produced with 53.9 grams of 0.5mm ZrO_2, in a 60° cone with an air flow equivalent to $1.7U_{ms}$.

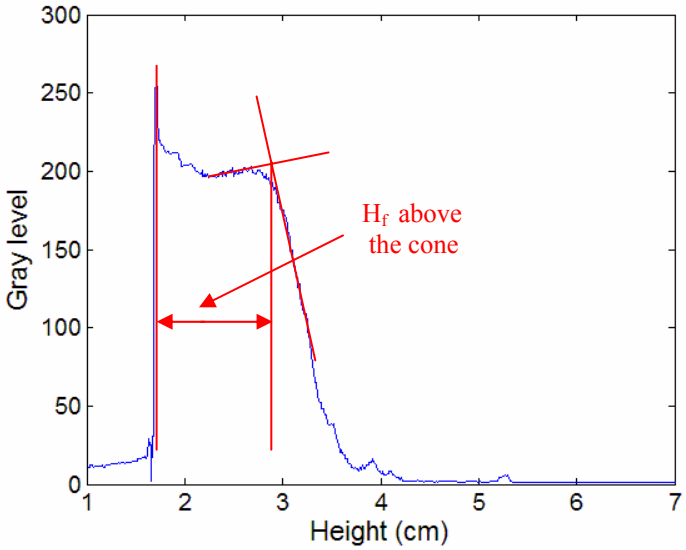

Figure 4.13. Determination of the fountain height above the cone based on the gray-scale intensity along the centerline of a composite image. Case: 53.9 grams of 650μm ZrO_2, 60° cone angle, and air flow rate = $1.7U_{ms}$.

5. Experimental results and analysis

5.1 Time average spouted bed features

5.1.1 Minimum spouting velocity, U_{ms}

As discussed in the previous chapter, the minimum spouting velocity, U_{ms}, was experimentally determined for a range of zirconia particle sizes and spouted bed cone angles. The best correlation for these data was found to be given by Equation 5.1:

$$\mathrm{Re}_{ms} = 0.0015 Ar^{0.86} \left(\frac{H_0}{D_c}\right)^{1.59} \tan\left(\frac{\gamma}{2}\right)^{0.87} \qquad (5.1)$$

with $0.3\text{mm} \le D_p \le 0.65\text{mm}$, $0.5 \le H_0/D_c \le 1$, and $45° \le \gamma \le 75°$. As illustrated in Figure 5.1, the fit between the observations and Equation 5.1 is quite good, with a coefficient of regression of 0.98.

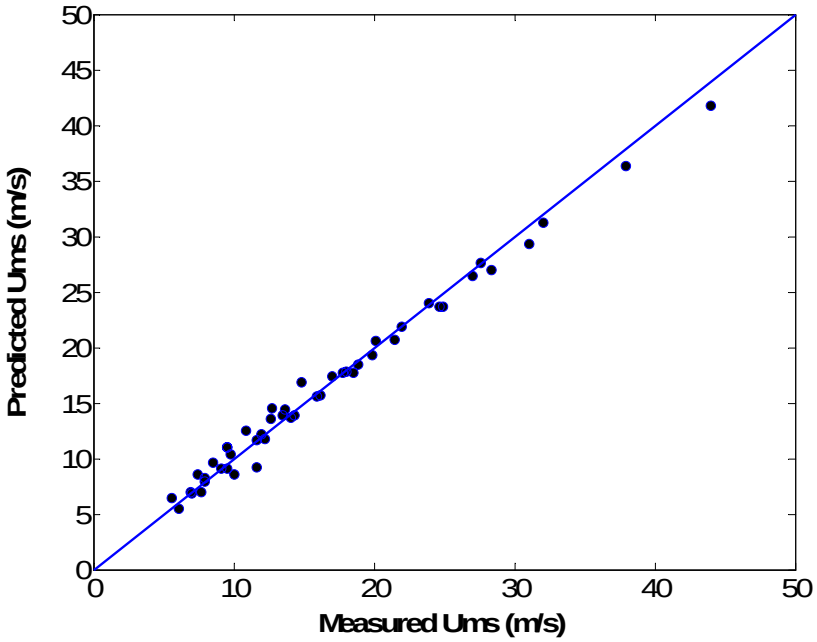

Figure 5.1 U_{ms} predicted by Equation 5.1 vs. measured U_{ms}.

Table 5.1 illustrates the goodness of fit for Equation 5.1 compared to other correlations from the literature for a range of experimental bed heights. Correlations from the literature are designated with numbers, corresponding to 1) San Jose (1992), 2) Tsvik (1967), 3) Gorshtein (1964), 4) Mukhlenov (1965) and 5) Aravinth (1997). Of these, the correlation by Aravinth is the best, and its predicted error still ranges between 12%~60%. The prediction error of correlation (5.1) is 8~13%. Other correlations from the literature were found to have even higher errors for the experimental system of interest here, and are not listed.

It should perhaps not be surprising that many correlations in the literature do not compare well with the U_{ms} observations from this study. In particular, the effects of cone angle were found to be quite significant, but many correlations do not even include cone angle as a variable. Also, most correlations are based on measurements with particles having a density lower than or around 3 g/cm^3, while the density of ZrO_2 is 5.89 g/cm^3. In addition, most correlations in the literature were derived for deep spouted beds (H_0/D_c > 1).

Table 5.1 Comparison of measured U_{ms} with predicted U_{ms} values. D_p=0.5mm, γ=45°.

H_0/Dc	Measured Value(m/s)	Equation 5.1 (m/s)	Method 1(m/s)	Method 2(m/s)	Method 3(m/s)	Method 4(m/s)	Method 5(m/s)
0.5	**0.0450**	0.0393	7.43	14.99	3.78	10.61	0.072
0.6	**0.0586**	0.0525	9.6	18.8	3.9	12.7	0.0869
0.8	**0.0874**	0.0829	14.7	26.8	4.2	17	0.1159
1	**0.1290**	0.1182	20.7	35.4	4.4	21.2	0.1448

5.1.2 Time-average gas pressure drop

The air pressure drop across the empty spouted beds are measured and analyzed. Three correlations predicted the pressure drop across the empty spouted beds are obtained as below, for the base cone angles γ:

γ=45°: $\Delta P = -23.88 + 14.7u_i + 0.84u_i^2$ (5.2a)

γ=60°: $\Delta P = -1.03 + 5.38u_i + 1.62u_i^2$ (5.2b)

γ=75°: $\Delta P = 13.04 + 3.69u_i + 1.58u_i^2$ (5.2c)

where u_i is the gas velocity in the inlet pipe with units in m/s. ΔP has units in pascal.

The air pressure drop across the particles inside the spouted bed equals the measured air pressure drop minus the air pressure drop across the empty spouted bed at the corresponding air flow rate.

Experimental time-average pressure drop measurements were made for the zirconia particles over the following ranges: D_p =0.3-0.65mm, H_0/D_c = 0.5 - 1, γ = 45 - 75°, and U/U_{ms} = 1-1.9. The experimental mean pressure drop measurements were found to correlate well with Equations 5.3a and 5.3b as below:

$$\frac{\Delta P_s}{\rho_p H_0 g} = 0.15\left(\frac{D_p}{D_c}\right)^{-0.208}\left(\frac{H_0}{D_c}\right)^{0.02}\left[\tan\left(\frac{\gamma}{2}\right)\right]^{-0.039} \quad (5.3a)$$

$$\frac{\Delta P_s}{\rho_p H_0 g} = 1.05\left[\tan\left(\frac{\gamma}{2}\right)\right]^{0.057}(\mathrm{Re}_{ms})^{-0.1}\left(\frac{H_0}{D_c}\right)^{0.224} \quad (5.3b)$$

Both Equations 5.3a and 5.3b predict the same result, but Equation 5.3b contains the same predictive variables as Mukhlevnov and Gorshtein (1964) and Olazar *et al.* (1993) correlations. Equations 5.3 a and b actually can be transformed from one to other if Re_{ms} is expressed in terms of γ, D_p and H_o as in Equation 5.3a. The regression coefficient for both forms of the correlation is 0.99. Figure 5.2 shows the pressure drops predicted by equation (5.3) are very close to the corresponding experimental data.

Looking more closely at the correlations by Mukhlevnov and Gorshtein (1964) and Olazar *et al.* (1993), it is seen in Table 5.2 that these correlations from the literature do a poor job of predicting the observed pressure drops in the bed used in this study.

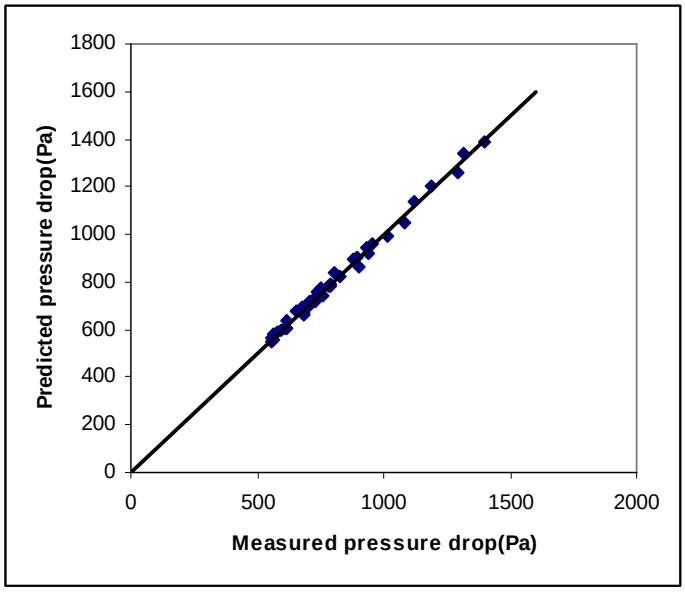

Figure 5.2 Spouted bed pressure drop predicted by Equations 5.3 a and b vs. measured pressure drop.

Table 5.2 Comparison of ΔP_s by Equation (5.3) with ΔP_s by Mukhlevnov and Olazar equations (Units: D_p: mm, γ:degree, ΔP_s: Pa, Error: %)

Condition			Experimental ΔP_s	ΔP_s by Equation (5.2)		ΔP_s by Mukhlevnov equation(Pa)		ΔP_s by Olazar equation(Pa)	
D_p	γ	H_0/D_c		data	error	data	error	data	error
0.3	45	1	1316.6	1338.3	**1.6**	1646.5	**25.1**	2936.3	**123**
0.3	60	0.6	786.3	784.5	**-0.2**	1422.7	**80.9**	1695.3	**115.6**
0.3	75	0.6	755.0	775.7	**2.7**	1469.5	**94.6**	1631	**116**
0.4	45	1	1290.6	1260.6	**-2.3**	1618.1	**25.4**	2921	**126.3**
0.4	60	0.8	1018.4	990.9	**-2.7**	1490.9	**46.4**	2214	**117.4**
0.4	75	0.5	612.0	606.7	**-0.9**	1263.8	**107**	1328.1	**117**
0.5	45	1	1186.2	1203.4	**1.5**	1476	**24.4**	2842	**139.6**
0.5	60	0.5	582.6	585.7	**0.5**	1151.2	**97.6**	1355.4	**132.6**
0.5	75	0.6	676.4	697.5	**3.1**	1239.1	**83.2**	1549.7	**129.1**
0.65	45	0.5	557.3	561.9	**0.8**	1071.3	**92.2**	1403.5	**151.8**
0.65	60	0.8	881.3	895.7	**1.6**	1246	**41.4**	2097.9	**138**
0.65	75	0.6	682.3	660.5	**-3.2**	1138.8	**66.9**	1510.9	**121.4**

It is clear that the Mukhlevnov (1964) and Olazar (1993) correlations considerably overestimate the pressure drops in the current experiments. The relative error by the Mukhlevnov method ranges from 24% to 107% while the Olazar method overestimates 116% ~ 152%. Again, the experimental ranges for which of these literature correlations were derived are quite different from the applicable ranges here.

5.1.3 Gas velocity profiles

As described in the previous chapter, time-average gas velocity profiles were measured in the experimental spouted bed using a pitot tube. In order to get some sense of the variations in these profiles with inlet gas velocity, velocity measurements were made at varying elevations and radial positions as well as at three different inlet air flows: 0.148,

0.193 and 0.237 m/s superficial gas velocity, which corresponds to 1.5, 1.9 and 2.3 U/U_{ms} respectively.

Figure 5.3 illustrates the average gas velocity profile as a function of radial position and elevation above the air inlet. In this case, the bed was operated with the 60° inlet cone and 54.5 grams 0.5mm ZrO_2 ($H_0/D_c = 0.7$). In this case the inlet air U/U_{ms} was 1.9. The observed velocity profiles appear to be very similar to profiles reported by Becker (1961) and Olazar *et al.* (1995a). The air velocity near the spout center is characteristically much higher than near the wall, but the radial gradient in velocity falls quickly with height. Both the central and wall velocities drop rapidly with height in the cone as the cross-sectional area expands. By the time the air exits the bed (i.e., enters the fountain), the radial gradient is nearly flat. The above trends suggest that there is considerable outward flow of air from the central core as a function of height in the core, even though there is little time to do so in such a shallow bed.

Figure 5.4 illustrates the variation in the central gas velocity with bed height in the 60° conical spouted bed with 54.5 grams ZrO_2 (static bed height = 3.5cm) operated at 1.5, 1.9 and 2.3 U/U_{ms} or 290, 378 and 465 cm^3/s. Note that as height increases, the central velocity decreases due to radial expansion of the air. The curve shapes appear similar for each of the three flows. In the literature, this radial expansion of the gas is often described as a 'leakage' of gas from the central spout zone to the annular zone. In the section, gas in the annular zone also continues to expand with height as the cross-section increases. This geometrically motivated gas expansion in the annulus provides a

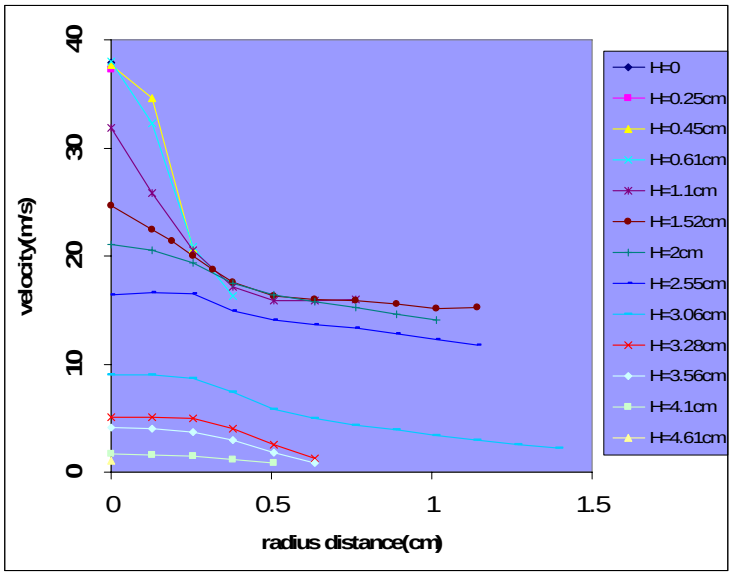

Figure 5.3 Gas velocity profile of 60° spouted bed with 54.5 grams of 0.5mm ZrO_2 ,static bed height = 3.5cm at air flow rate 1.9 U/U_{ms} or 378cm^3/s. H=0 corresponds to the cone bottom.

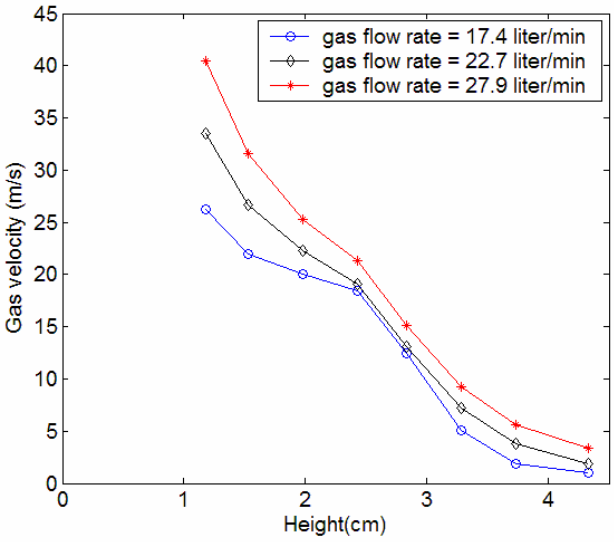

Figure 5.4 Central velocity of 60° spouted bed with 54.5grams ZrO_2 (static bed height = 3.5cm) operated with 1.5, 1.9 and 2.3 U/U_{ms} air flow.

continuing gradient that promotes leakage from the core to the annulus. At the level of the fountain, the difference in velocity between the central and annular zones disappears, and there is no longer a driving force for gas to 'leak' radially.

5.1.4 Fountain height

As described previously, time-average fountain heights were measured by creating composite images from video recordings. An investigation of the fountain height correlations in the literature revealed that the results of the measurements in this study are relatively well correlated by a correlation of the form proposed by San José *et al.* (2005b). The resulting correlation for the present data is given by:

$$\frac{H_f}{H_0} = 7.15\gamma^{0.64}\left(\frac{D_p}{D_c}\right)^{0.20}\left(\frac{H_0}{D_c}\right)^{0.34}\left(\frac{U}{U_{ms}}\right)^{1.03} \qquad (5.4)$$

Here the appropriate parameter ranges are: H_0/D_c = 0.5 ~ 1, γ = 0.785~1.309, D_p = 0.3~0.65mm, U/U_{ms}=1.2 ~ 2.1. The regression coefficient for the fitted correlation is 0.91.

Figure 5.5 illustrates the agreement between equation 5.4 and the observed fountain heights in this study. The maximum error is 15%.

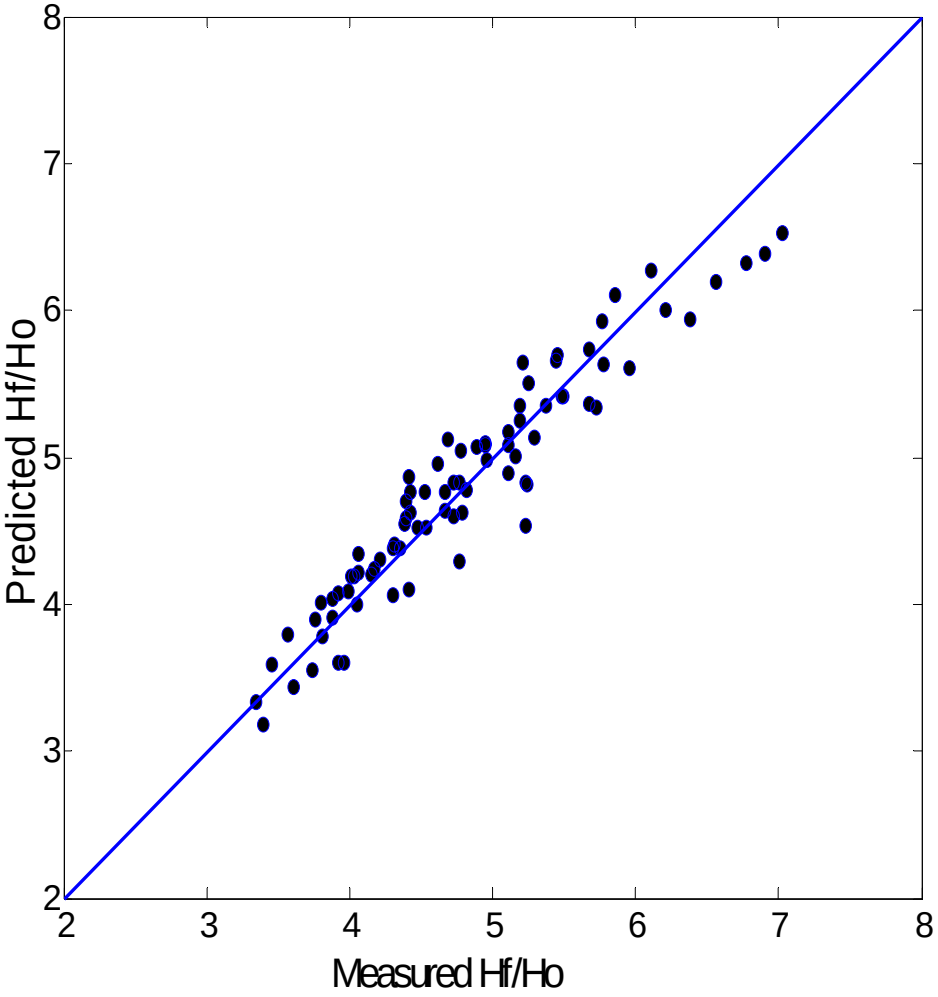

Figure 5.5 Fountain height predicted by equation (5.3) vs. measured fountain height.

5.2 Dynamic trends

5.2.1 Gas pressure drop

Under steady spouting conditions, gas pressure drop over the bed constantly varies over time. In some cases the variation occurs almost periodically around a well-defined mean, but in others the variation is more complex and erratic. Figures 5.6 and 5.7 illustrate an example time series of pressure drop at two different scales of temporal magnification. From the visual and laser measurements made with the glass spouted bed, it is clear that the pressure drop variations correlate with the global motion of particles in the bed. This correlation is especially visible for the particles in the entrainment zone near the air inlet, in the fountain, and for the particles near the walls of the annular zone. Such a correlation implies that the global particle circulation is closely coupled to the gas pressure pulsations, and thus models that capture gas pressure drop pulsations should be useful for

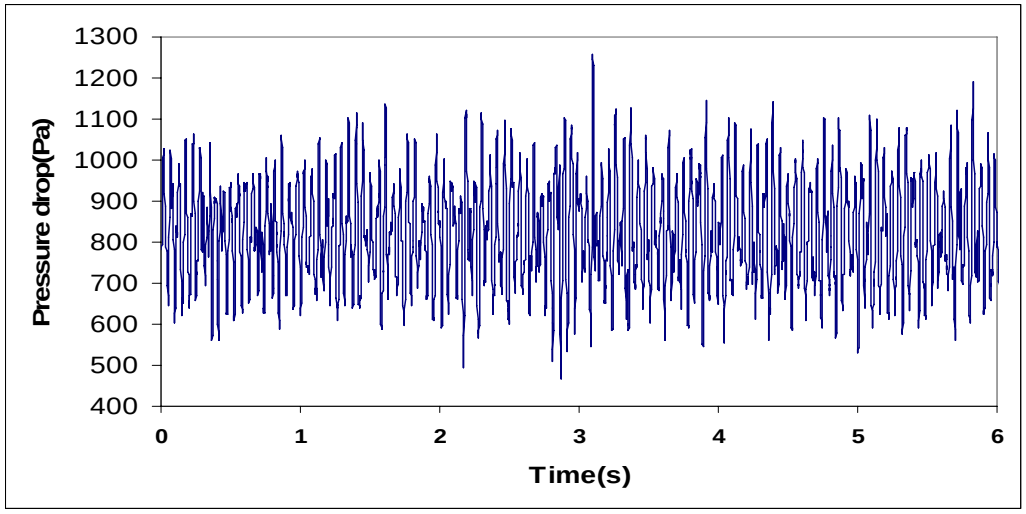

Figure 5.6 Total gas pressure drop versus time for 53.9 grams 0.5mm ZrO_2 (static bed height = 3.5cm) in 60° spouted bed for a gas flow rate corresponding to U/U_{ms}= 1.5.

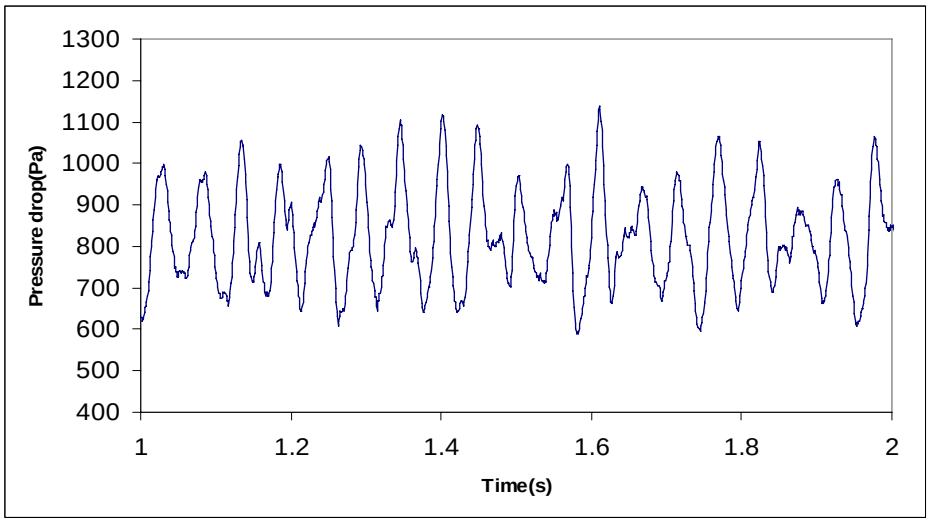

Figure 5.7 Time scale enlargement of the gas pressure drop time series from Figure 5.6. Note the relatively large pulses occurring about 20 times/s. Lower and higher frequency variations in the pulses add a non-periodic complexity.

simulating and tracking the global mixing process. The inventory of particle inside the spouted bed is set to be 53.9grams which corresponds to 0.7 H_0/D_c.

5.2.2 Dynamic pressure drop statistics

One way of characterizing the pressure drop variations over time is to use typical statistics such as standard deviation, skewness and kurtosis. Figure 5.8 illustrates how these statistics calculated from the measured gas pressure drop vary with U/U_{ms} for the 60° conical spouted bed with 53.9 grams 0.5mm ZrO_2 (static bed height = 3.5cm) . As gas flow rate is lowered from U/U_{ms} = 2.3 to 1, the standard deviation of the dynamic pressure drop decreases, reflecting a diminishing size for the pressure pulses. Skewness and kurtosis, on the other had, grow larger at the low flows, indicating that the pressure

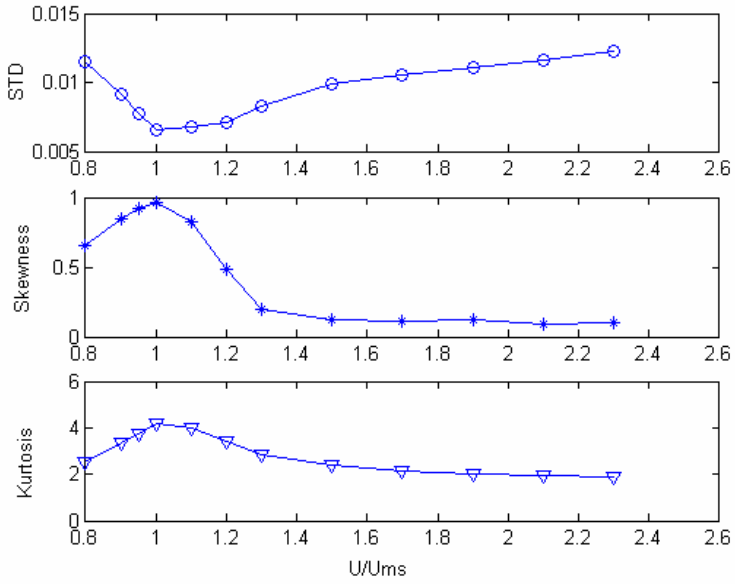

Figure 5.8 Variation of standard deviation, skewness and kurtosis of the dynamic pressure drop vs. U/U_{ms} for the 60° conical bed containing 53.9 grams 0.5mm ZrO_2 (static bed height = 3.5cm).

oscillation magnitudes are becoming less Gaussian (more skewed and less bell-shaped) in distribution.

Figures 5.9 through 5.11 illustrate the trends in the dynamic pressure drop standard deviation, skewness, and kurtosis for changes in particle size and cone angle while U/U_{ms} is held constant. In general, the standard deviation and skewness decrease as particle size increases for all cone angles studies, while the kurtosis varies in a more complex fashion. In figures 5.9 through 5.11, the particle masses in the spouted bed were fixed for each particle size. The particle mass for the 45° cone is 76.2 g, for 60° 53.9 g, for 75° 80.9 g

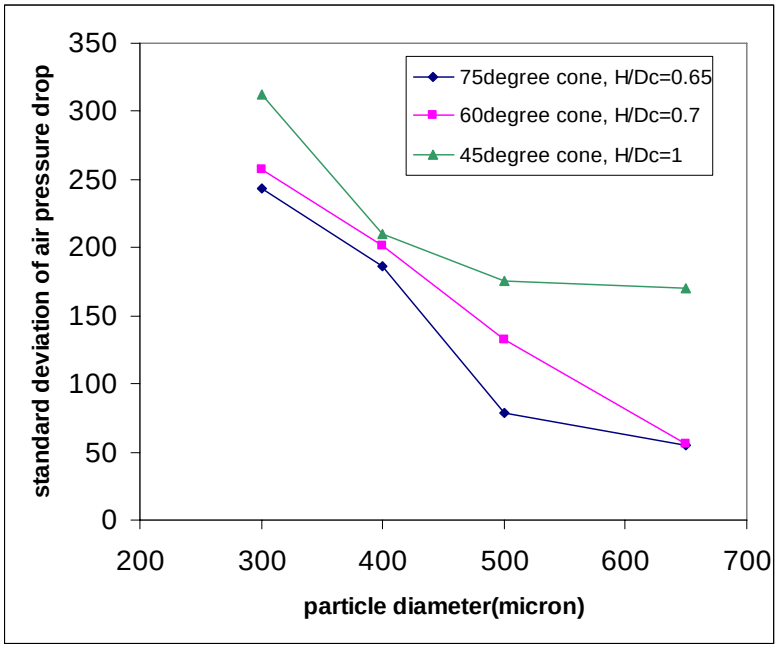

Figure 5.9 Standard deviation of the gas pressure drop vs. ZrO_2 particle diameter at $U/U_{ms}=1.5$

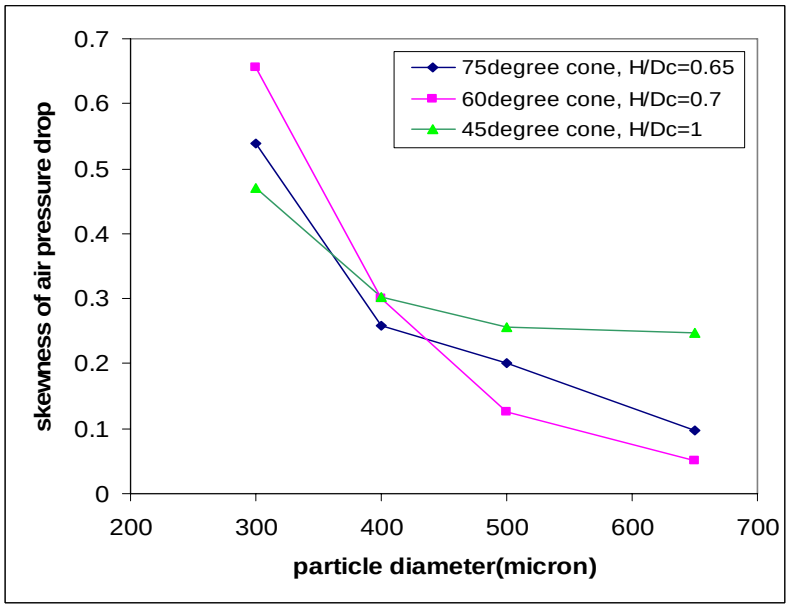

Figure 5.10 Skewness of the gas pressure drop vs. ZrO_2 particle diameter at $U/U_{ms}=1.5$.

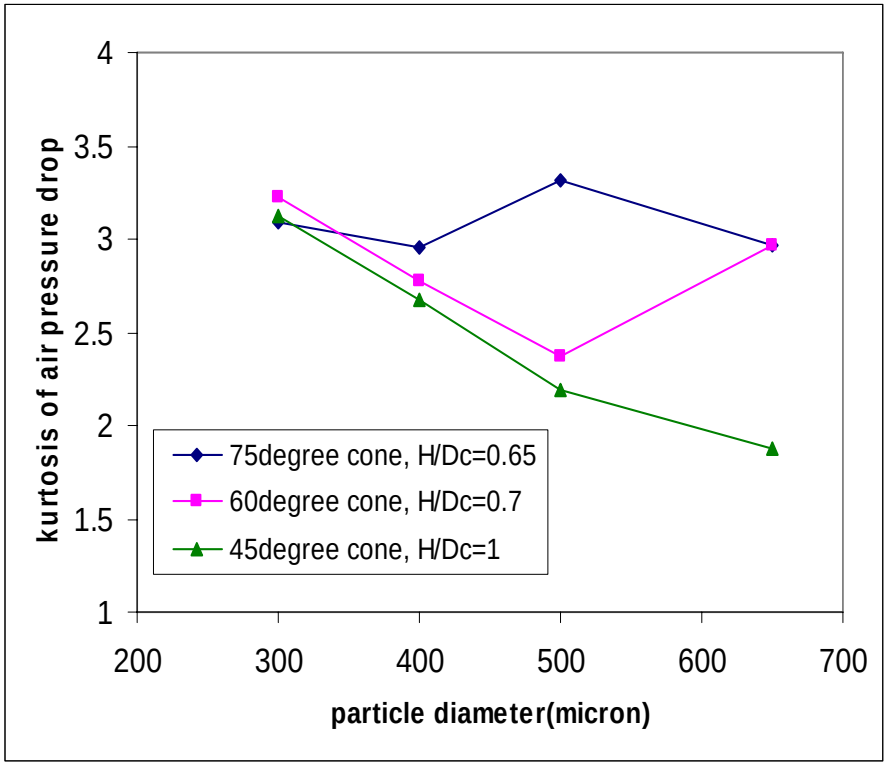

Figure 5.11 Kurtosis of the gas pressure drop vs. ZrO_2 particle diameter at U/U_{ms} =1.5.

One additional interesting statistic studied was the ratio of the dynamic pressure drop standard deviation to the average pressure drop. As illustrated in Figure 5.12, this ratio decreased in a monotonic way for a given cone angle as static bed height increased. Since the bed height directly correlates with the current state of coating in the TRISO process, it appears that this ratio might provide a way to monitor the coating process in real time. If the reliability of this statistic can be confirmed in pilot studies, it would be especially attractive as a process monitoring tool since gas pressure drop signals are typically always available.

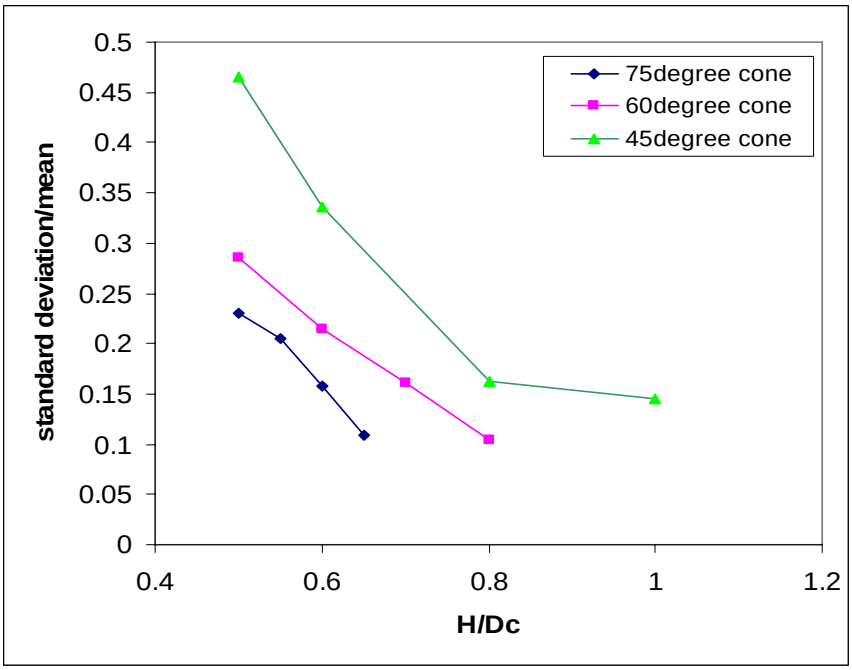

Figure 5.12 The ratio of standard deviation to average pressure drop vs. static bed height and cone angle for 500μm ZrO_2.

5.2.3 Dynamic pressure drop frequency analysis

Even though the pressure drop time series were often far from simple periodic oscillations, Fourier analysis revealed a lot about their characteristics and how these changed with changes in bed geometry, particle properties, and gas flow. As an example, Figure 5.13 illustrates the shift in the observed Fourier power spectrum as the inlet air flow was decreased from 2.1 U_{ms} to slightly below U_{ms} for 0.5mm zirconia particles in the 60° conical bed (with a static bed height of 3.5cm). In this case the dominant pulsation frequency shifted from 21.4 Hz to 17.4 Hz as air velocity dropped from a vigorously spouting condition ($2.3U_{ms}$) to a much more smooth spouting condition at $1.3U_{ms}$. At $U/U_{ms} = 1.2$, the dominant pulsation frequency bifurcated, revealing two

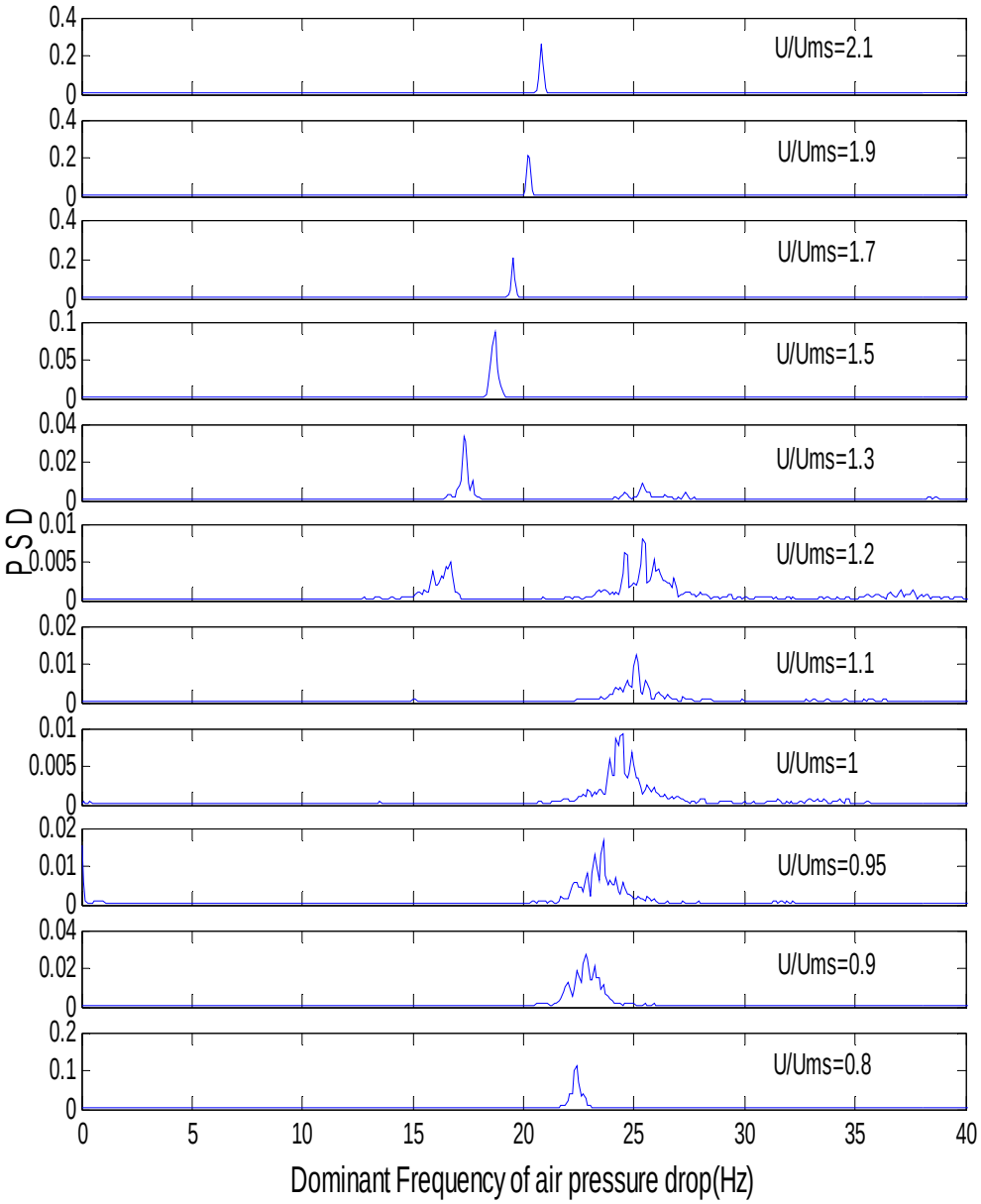

Figure 5.13. Shifts in the Fourier power spectra in the gas pressure drop as the inlet gas flow rate was changed. In this case the 60 ° conical bed was composed of 0.5mm zirconia particles with a static bed depth of 3.5cm.

distinct peaks in the power spectrum. The higher frequency appeared to correspond to a warping of the main pulse shape such that it split into two sub-pulses, creating higher frequency oscillations at nearly twice the main pulse frequency

As air flow continued to drop to U_{ms} and below, the higher dual pulse frequency became dominant at about 25 Hz and then shifted down slowly until the minimum air flow was reached (that is, the point at which particles began falling out through the gas inlet. In this flow region, the 'quivering' of the particles could be observed by eye on the bed surface.

Figure 5.14 depicts the above trends in terms of the variation in the dominant Fourier peak as a function of air flow. Note the very sudden jump in the dominant frequency

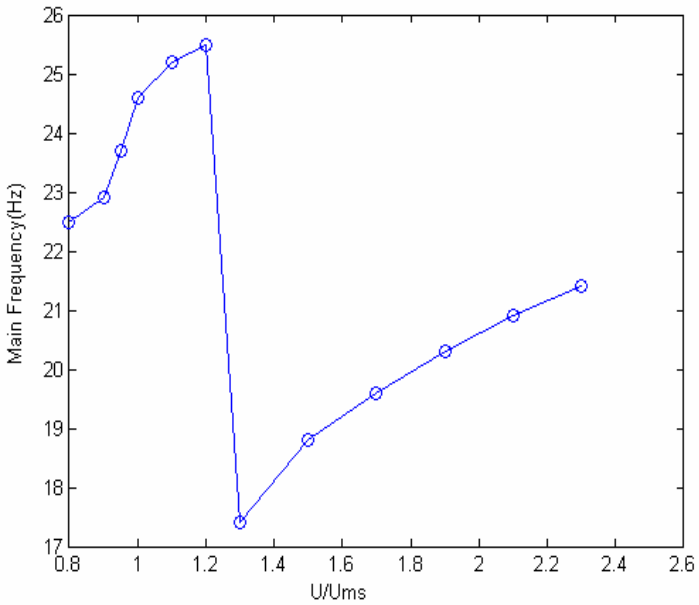

Figure 5.14. Dominant frequency *vs.* gas flow rate for the same case depicted in Figure 5.13.

associated with the bifurcation as the air flow passes through U_{ms}. Significant shifts in the dominant pulsation frequency were also observed in association with changes in cone angle and particle size as illustrated in Figures 5.15 and 5.16. In general, increases in both particle size and cone angle were accompanied by a reduction in the main pulsation frequency. The situation for particle size was more complex however, because the smallest particles (0.3mm) had a much different behavior than the larger sizes. For the former, the dominant pulsation became extremely periodic but there was also a wide band of very complex high frequency oscillations The sudden change in characterization between 0.3 and 0.4mm particles is indicative of some sort of bifurcation event similar to that seen near U_{ms}. Although very intriguing, this bifurcation was considered outside the scope of this investigation and was left for future investigators.

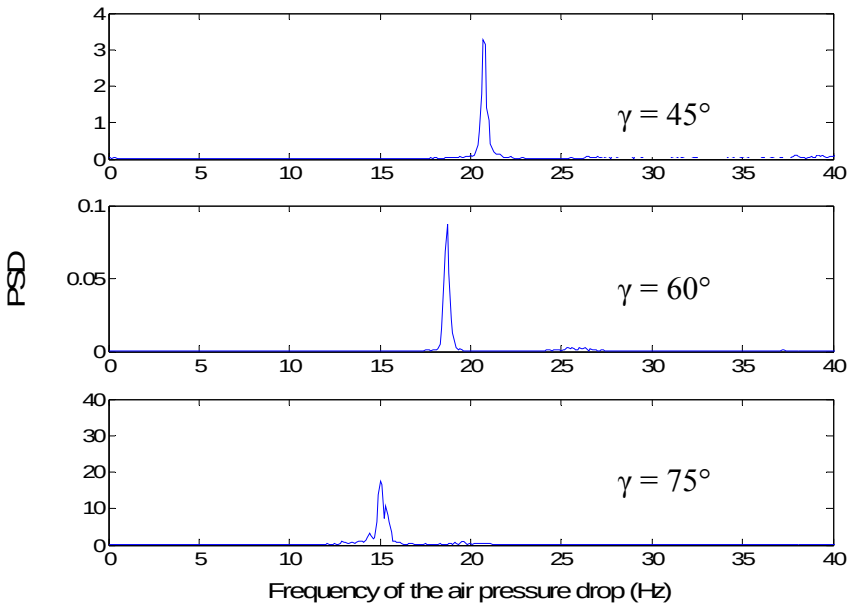

Figure 5.15 Dominant frequency of ΔP for 500 μm ZrO_2 in 45°, 60° and 75° spouted beds at U/U_{ms}= 1.5, H_0/D_c = 0.6.

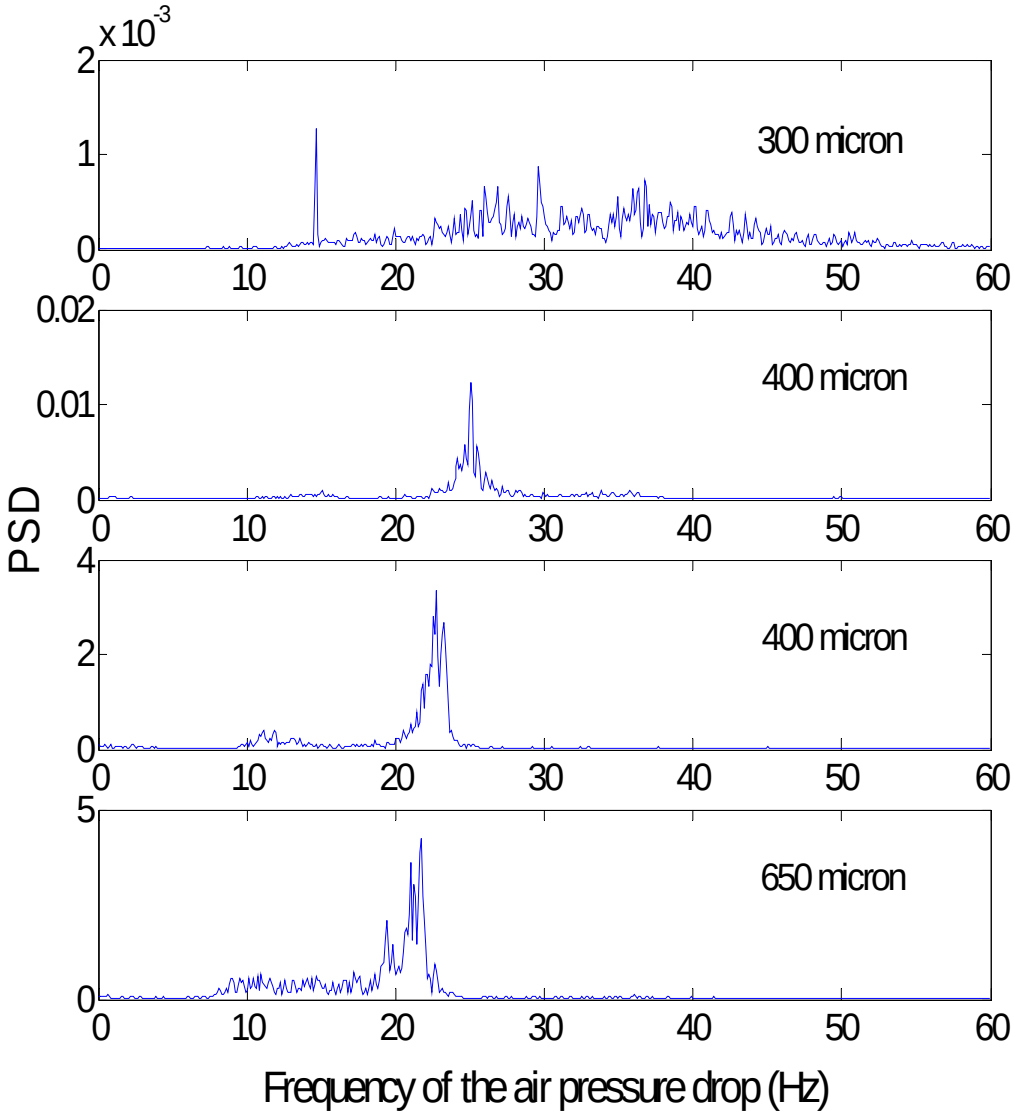

Figure 5.16 Dominant frequency of ΔP for 300, 400, 500 and 650μm ZrO_2 in 60° spouted beds at U/U_{ms}= 1.1, H_0/D_c = 0.7.

The preliminary study observes that 0.2mm zirconia particles behaves in quite different ways from 0.3, 0.4, 0.5 and 0.65mm zirconia particles in terms of fountain shape. The latter fountain shapes are basically parabola with height varying with time. The fountain shapes of 0.2mm zirconia particles not only keep changing in height but also swirling around its axial axis. It needs to be studied by itself and was left for future study.

In contrast to the previous cases of parametric variation, the static bed height did not have an appreciable impact on the dominant pulsation frequency. This can be seen in Figure 5.17, where the dominant frequency stays nearly constant near 19 Hz for four different static bed heights.

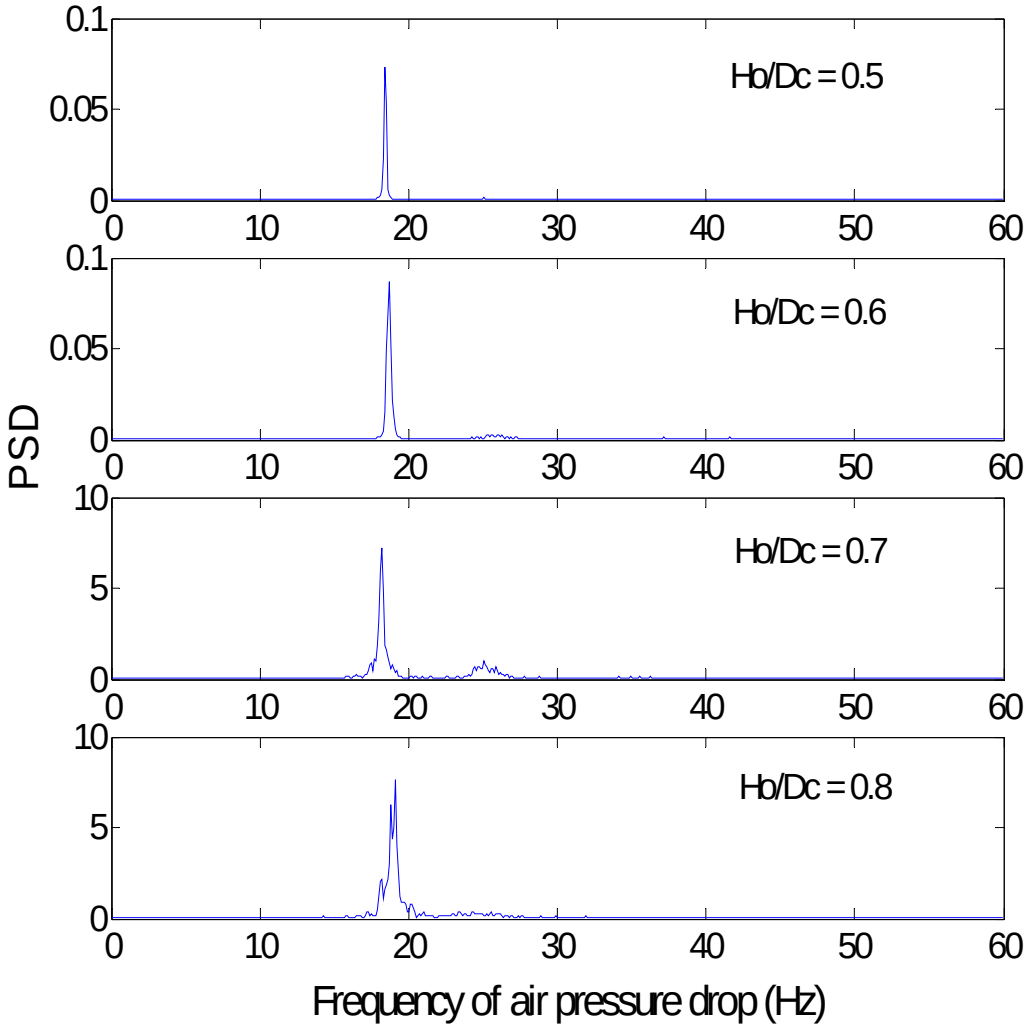

Figure 5.17 Dominant frequency of ΔP for 500 μm ZrO_2 in 60° spouted bed at U/U_{ms}= 1.5, H_0/D_c = 0.5, 0.6, 0.7, and 0.8 (from high to low).

6. Low-order model

6.1 Objectives of low-order model development

As discussed previously, computational models for multi-phase flows that utilize discrete element methods (DEM) and computational fluid dynamics (CFD) can provide extremely detailed simulations of fluidized and spouting beds, but they do so at a significant cost in computational overhead and time. Such costs can be worthwhile when the objective is to evaluate detailed design changes or to probe the underlying physics. But for some purposes, such as on-line diagnostics and controls, simpler approaches are more desirable. Based on the previously described experimental observations of the zirconia spouted bed behavior, it was concluded that a simplified dynamical model of gas and solids interactions for shallow spouted beds could be constructed to capture both the key time average and dynamical features, while also operating in near-real time.

The objective in this chapter is to propose the basic components of such a model and to describe how it should function. In a succeeding chapter, the general trends predicted by this model are studied and compared against the experimental observations for the experimental zirconia spouted bed. Where deficiencies in the model are identified, possible future improvements are recommended.

6.2 Modeling approach and assumptions:

In much of the prior literature, spouted beds have been conceived of as having three characteristic zones: the spout, the fountain, and the annulus (see for example Mathur and Epstein (1974b). The experimental observations in the present study suggest the addition

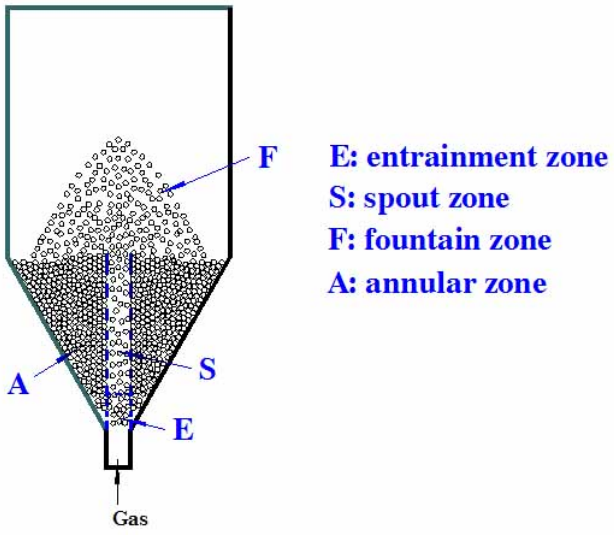

Figure 6.1 schematically summarizes the location of each of the four conceptual zones.

of a fourth conceptual zone, the entrainment zone, which is located immediately above the gas inlet as shown in Figure 6.1. The importance of this fourth zone is supported by the observation that the initial entrainment of particles by the gas occurs at the lower gas-particle interface and that the rising particles form a cluster which is conveyed largely intact upward to the fountain. The size and frequency of the particle cluster formation appears to determine the size and frequency of the pressure pulsations and the overall solids circulation rate. This same type behavior has been observed in CFD simulations by Pannala *et al.* (2006).

The assumed characteristics for each of these zones are summarized below:

- Entrainment zone (denoted with subscript E)
  - Located below the central spout above the gas inlet.
  - Gas enters the bottom at constant mass rate.

- Solids enter radially from the annular zone.
- Solids and most of the gas exit vertically out the top into the spout.
- Some gas exits radially into the annular zone when solids are entering (see below).
- Pressure drop is sufficiently low that gas velocity can be considered constant over this zone.

- Spout zone (denoted with subscript S)
  - Located on the centerline above the entrainment zone and below the fountain zone.
  - Cylindrical shape with constant diameter equal to the gas inlet diameter.
  - Gas and solids enter at the bottom and exit at the top.
  - Gas and solids move in plug flow with no radial gradient.
  - Drag from gas continues to accelerate solids until the top of the spout zone is reached.
  - Pressure drop is sufficiently low that gas velocity can be considered constant over this zone.
- Fountain zone (denoted with subscript F)
  - Above both the annular and spout zones, extending radially across the entire upper bed.
  - Gas and solids enter from the spout zone.
  - Gas flow from spout expands radially to fill entire cross-section and gas drag on particles is effectively zero.

- Within the fountain, particles move in ballistic trajectories defined by the spout exit velocity and effect of gravity.
- Particles leaving the spout zone fan out equally such that they become evenly distributed over the top of the annular zone.
- Gas pressure and velocity are effectively constant and equal to the exit values.

- Annular zone (denoted with subscript A)
  - Extends between walls and the outer radii of the entrainment zone and spout.
  - Gas flow is minimal and enters radially from the entrainment zone when particles flow into the entrainment zone.
  - Solid particles enter from fountain in uniform surface layer and exit by being pulled into entrainment zone.
  - Solid particles are loosely packed at minimum void fraction (i.e., in a de-fluidized state) and height varies as there is net inflow/outflow.
  - Solids downflow is uniform and regulated by solids transfer into entrainment zone.

In addition to the above assumptions about each zone, there are other assumptions common to all the zones:

- The total mass of solids (sum of all zones) is constant.
- Differential momentum and mass balances must be satisfied for the solids and gas in each zone.

- Unless otherwise specified, the conditions in each zone can be approximated in terms of average density and velocity for both the gas and solids.
- Gas acceleration/deceleration in each zone is much faster than solids, so gas flow reaches steady state locally at each time increment.

6.3 Differential balances for each zone

6.3.1 Entrainment zone

Applying the last assumption above that the gas flow reaches steady state immediately relative to the solids, the time derivatives for the mass and momentum of the gas are set to zero, and the rate controlling processes for the hydrodynamics in this zone are the differential balances of mass and momentum for the solids. The differential solids momentum balance requires the following:

$$\rho_p A_E H_E \frac{d[(1-\varepsilon_E)v_{Ep}]}{dt} = -Gravity_{Ep} + Drag_{Ep} + F_s \qquad (6.1).$$

The gravity force is defined by, $Gravity_{Ep} = \rho_p A_E H_E (1-\varepsilon_E) g$ (6.2).

The drag force is defined by, $Drag_{Ep} = \frac{0.75 H_E \rho_p (1-\varepsilon_E)(u_E/\varepsilon_E - v_E)^2 C_D}{d_p} A_E$ (6.3).

u_E is the gas velocity in the entrainment zone. It is well known that the air expands suddenly after it passes through the narrow inlet pipe in turbulent flow and enters the bottom of the spouted bed. So the diameter of the entrainment zone could be equal to or bigger than the inlet pipe diameter.

Since the gas flow has reached steady state at any instant in time, and the particle-gas slip velocity is well defined. The drag coefficient, C_d, is related to the particle Reynolds number using a correlation such as:

$$C_d = \frac{24}{\mathrm{Re}_p}(1 + 0.15\,\mathrm{Re}_p^{\,0.687}), \text{ for } \mathrm{Re_p} < 10^3 \qquad (6.4);$$

$$C_d = 0.44, \text{ for } \mathrm{Re_p} > 10^3 \qquad (6.5);$$

where the particle Reynolds number, $\mathrm{Re}_p = \dfrac{d_p \rho_p \,|\, u_{Ep}/\varepsilon_E - v_{Ep} \,|}{\mu_{Ef}}$ (6.6).

The last term in Equation 6.1, F_s, represents the solid particles resistance to compression to a void fraction smaller than their minimum static value. Effectively the particles become incompressible at the point of maximum packing and any further compression is strongly resisted. For purposes of this study this anti-compression force is represented as a sharply rising exponential function of void fraction:

$$F_s = e^{-1000\,(\varepsilon_E - \varepsilon_{mf})} \qquad (6.7).$$

The differential mass balance for particles in the entrainment zone is given by:

$$\frac{dm_{Ep}}{dt} = \dot{m}_{Ep}(in) - \dot{m}_{Ep}(out) \qquad (6.8).$$

In Equation 6.8 $\dot{m}_{Ep}(in)$ is the radial inflow of solids mass from the annular zone. For this study this inflow rate is assumed to be proportional to the available 'empty space' in the entrainment zone. This is stated mathematically as:

$$\dot{m}_{Ep}(in) = k_E A_E H_E \rho_p (\varepsilon_E - \varepsilon_{mf}) \qquad (6.9)$$

where ε_{mf} is the minimum void fraction of loosely packed particles, and k_E is a characteristic granular flow rate constant with units of 1/time. The quantities A_E and H_E are the cross-sectional area and height of the entrainment zone, respectively. The rule governing k_E will be recommended for future study by means of more advanced experimental.

The quantity $\dot{m}_{Ep}(out)$ is the vertical mass outflow of solids into the spout. This flow rate is determined by the upward velocity of the particles and is equal to:

$$\dot{m}_{Ep}(out) = v_{Ep} A_E \rho_p (1-\varepsilon_E) \qquad (6.10)$$

Combining Equations 6.8-.10, the differential mass balance can be restated as:

$$\rho_p A_E H_E \frac{d(1-\varepsilon_E)}{dt} = kA_E H_E (\varepsilon_E - \varepsilon_{mf})\rho_p - v_{Ep} A_E \rho_p (1-\varepsilon_E) \qquad (6.11).$$

Equation 6.11 can be further simplified to obtain,

$$\frac{d\varepsilon_E}{dt} = \frac{v_{Ep}(1-\varepsilon_E)}{H_E} - k(\varepsilon_E - \varepsilon_{mf}) \qquad (6.12).$$

Equations 6.1 and 6.12 can be combined and rearranged to yield,

$$\frac{dv_{Ep}}{dt} = \frac{{v_{Ep}}^2}{H_E} - \frac{kv_{Ep}(\varepsilon_E - \varepsilon_{mf})}{(1-\varepsilon_E)} + \frac{Drag_{Ep} + F_s}{\rho_p A_E H_E (1-\varepsilon_E)} - g \qquad (6.13)$$

Equations 6.12 and 6.13 are the final ODEs for the entrainment zone.

One additional aspect of the entrainment zone needs to be included in the model in order to capture an important observed feature of entrainment zone behavior. Although the gas flow entering the bottom of the entrainment zone is constant, the exit flow can leave

either through the top into the spout or through sides into the annulus. The side flow of gas into the annulus compensates for the inward solids flow that occurs after the entrainment zone has been emptied of solids and the annulus solids collapse into the available space. This side flow gas is visible experimentally as a kind of upward moving wave that passes upward through the annular solids while the entire annular solids mass shifts downward in response.

To capture this process the model produces a split in the outlet gas flow depending on whether the solids inventory in the entrainment zone is increasing or decreasing. Specifically, when the net solids inventory is decreasing, all the gas exits from the top. When the net solids inventory is increasing, a portion of the gas exits radially and the remainder exits at the top. The net effect is to reduce the upward gas flow and thus the rate at which solids are entrained. This can be summarized mathematically as

$$u_E = u_i \quad \text{for} \quad \frac{d\varepsilon_E}{dt} \geq 0 \tag{6.14a}$$

$$u_E = k_r u_i \ \text{for} \ \frac{d\varepsilon_E}{dt} < 0 \tag{6.14b}$$

where k_r (the entrainment velocity ratio) is an empirical constant between 0 and 1. k_r would be determined in this way such that the simulated fountain height equals to the experimental results. Since the drag force on the solids depends on the relative gas-solids slip velocity, the drop in u_E that occurs when ε_E is increasing causes a sudden reduction in the drag force.

The above ordinary differential equations for void fraction and particle velocity in the entrainment zone can be rewritten in non-dimensional form as:

$$\dot{\varepsilon}_E = \frac{d\varepsilon_E}{dt^*} = -G(\varepsilon_E - \varepsilon_{mf}) + v_{Ep}{}^*(1-\varepsilon_E) \qquad (6.15)$$

$$\dot{v}_{Ep}{}^* = \frac{dv_{Ep}^*}{dt^*} = F_{Ed}{}^* - 1 - Gv_{Ep}{}^* \frac{\varepsilon_E - \varepsilon_{mf}}{1-\varepsilon_E} + v_{Ep}{}^{*2} + F_s{}^* \qquad (6.16)$$

where $v_{Ep}{}^* = \frac{v_{Ep}t_c}{H_E}$, $t_c = \sqrt{\frac{H_E}{g}}$, $t^* = \frac{t}{t_c}$, $G = kt_c$, and $F_{Ed}{}^* = \frac{F_{Ed}}{\rho_p(1-\varepsilon_E)g}$

F_{Ed} is the drag force exerted on particles in the entrainment zone.

The boundary condition for the entrainment zone is that the inlet gas velocity is constant; that is, for all t*>0:

$u_E = u_i$ at z = 0 (6.17a)

In dimensionless form this can be written as:

$$u_E^* = u_i^* = \frac{u_i}{\sqrt{gH_E}} \quad \text{at } z^* = 0 \qquad (6.17b)$$

In order to integrate the entrainment zone ODEs, it is also necessary to specify initial conditions for the void fraction and solids velocity. For simplicity these are usually taken as:

$$\varepsilon_E = \varepsilon_{mf} \text{ and } v_{Ep}^* = 0 \text{ at } t^* = 0 \qquad (6.18)$$

As previously discussed, the gas flow is assumed to be at steady-state for each time increment as the solids inventory and velocity in the entrainment zone evolves. Once the

ODEs for the entrainment zone are integrated, one important remaining gas-related quantity that can also be determined is the pressure drop. This is explicitly determined from:

$$\Delta P_E = F_{Ed}/A_E \qquad (16.19)$$

6.3.2 Spout zone

For deep spouted beds, most of the gas flows through the spout zone and only a small part of the gas leaks into the annular zone. For shallow spouted beds such as that studied here, one expects that the impact of radial gas leakage from the spout zone might be even less important. The gas velocity profile reported in previous chapter also indicates that until the fountain zone is reached, the gas velocity in the spout is much higher than in the annulus. So as a first approximation it is assumed here there is no radial gas leak from spout zone into the annular zone. This means that the gas flow throughout the spout zone equals to the flow rate of the gas flow entering from the entrainment zone.

The resulting solids momentum equation balance requires that:

$$\frac{d[\rho_p A_S H_S (1-\varepsilon_S) v_S]}{dt} = -Gravity_{Sp} + Drag_{Sp} \qquad (6.20)$$

where $Drag_{Sp} = \dfrac{0.75 H_S \rho_p (1-\varepsilon_S)(u_S/\varepsilon_S - v_S)^2 C_D}{d_p} A_S$ (6.21).

The drag coefficient, C_D, is calculated in the similar way as shown in equations 6.4 and 6.5. In the spout zone the particle Reynolds number is determined from:

$$\mathrm{Re}_{Sp} = \frac{d_p \rho_p \mid u_{Sp} / \varepsilon_S - v_{Sp} \mid}{\mu_{Sf}} \qquad 6.22.$$

The differential solids mass balance requires that:

$$\frac{dm_{Sp}}{dt} = \dot{m}_{Sp}(in) - \dot{m}_{Sp}(out) \qquad (6.23),$$

which can be rewritten as:

$$\frac{d[\rho_p A_S H_S (1-\varepsilon_S)]}{dt} = v_{Ep} A_E \rho_p (1-\varepsilon_E) - v_{Sp} A_S \rho_p (1-\varepsilon_S) \qquad (6.24).$$

In above equation, the spout zone height equals to the annular zone height minus entrainment zone height and both vary with time. At each time step, the height of the annular zone is calculated based on the mass of solid particles in annular zone. In other words, at each time the radius of the bottom surface and top surface of the annular zone can be obtained, which equal to $H_E \tan(\frac{\gamma}{2})$ and $(H_E + H_S)\tan(\frac{\gamma}{2})$ respectively. Then the volume of the annular zone V_A equals to

$$V_A = \{\frac{\pi}{3}\left[(H_E + H_S)\tan(\frac{\gamma}{2})\right]^2 - \frac{\pi}{3}\left[H_E \tan(\frac{\gamma}{2})\right]^2 - \frac{\pi}{4} D_S{}^2\} H_A \qquad (6.25)$$

Then the mass of the annular zone equals to

$$m_{Ap} = \{\frac{\pi}{3}\left[(H_E + H_S)\tan(\frac{\gamma}{2})\right]^2 - \frac{\pi}{3}\left[H_E \tan(\frac{\gamma}{2})\right]^2 - \frac{\pi}{4} D_S{}^2\} H_S \rho_p (1-\varepsilon_{mf}) \qquad (6.26)$$

By solving equation 6.26, the annular zone height can be obtained at every instant in time. Then the spout zone height is obtained.

Combining terms and rewriting equations 6.20 and 6.24 in dimensionless form yields:

$$\dot{\varepsilon}_S = \frac{d\varepsilon_S}{dt^*} = v_{Sp}^*(1-\varepsilon_S)\frac{H_E}{H_S} - v_{Ep}^*(1-\varepsilon_E)\frac{H_E}{H_S} \quad (6.27)$$

$$\dot{v}_{Sp}^* = \frac{dv_{Sp}^*}{dt^*} = \frac{v_{Sp}^*}{1-\varepsilon_S}\frac{d\varepsilon_S}{dt^*} - 1 + F_{Sd}^* \quad (6.28)$$

$F_{Sd}^* = \frac{F_{Sd}}{m_{Sp}g}$ and m_{Sp} is the mass of the solid particles in the spout zone, F_{Sd} is the drag force exerted on particles in the spout zone.

The whole spout zone is assumed to be uniform. The gas velocity and particle velocity at the boundary of the spout zone are equal to their corresponding values anywhere else in the spout zone. The inlet gas flow is equal to the exit gas flow at the top of the entrainment zone, and the resulting non-dimensional boundary and initial conditions are:

$u_S^* = u_E^*$ for t*>0 (6.29)

$\varepsilon_S = \varepsilon_{mf}$ and $v_{Sp}^* = 0$ at $t^* = 0$ (6.30)

Neglecting the pressure loss due to gas-wall friction and gas potential energy, the gas pressure drop in the spout zone can be calculated as below [Briens et al, 1988],

$$\Delta P_S = \frac{F_{Sd}}{A_S} \quad (6.29)$$

6.3.3 Fountain zone

As soon as gas exits the spout and annular zones, the flow area is expanded to the whole bed cross-sectional area including top annular area plus spout area. Gas pressure in the fountain zone equals to the atmosphere pressure. Gas velocity becomes so small that the drag force exerted on solid particle is trivial compared to gravitational force particle.

So the gravitational force can be treated as the total force exerted on solid particles, and

the gas pressure drop in fountain zone can be approximated as zero. The momentum balance on each particle becomes simply:

$$\frac{dv_{Fp}}{dt} = -g \qquad (6.30.)$$

This can be restated in dimensionless form as:

$$\frac{dv_{Fp}^{*}}{dt^{*}} = -1 \qquad (6.31).$$

The particles shooting out of the spout zone at the same time step share the same velocity in the fountain zone as time evolves until they fall upon the top surface of the annular zone. Different sets of particles coming out of spout zone at different times have different speed. And the particle speed decreases as they rise till they reach the apex and then increases due to gravitational acceleration till they merge into annular zone. Now particles in fountain zone are not treated as having average speed any more as the way the particles in both entrainment zone and spout zone are treated. The trajectories of individual particles are tracked at each time step in the fountain zone.

The corresponding boundary and initial conditions are:

$v_{Fp}^{*} = v_{Sp}^{*}$ at $z^* = 1+H_S/H_E$ for $t^*>0$ (6.32)

$\varepsilon_F = \varepsilon_{mf}$ and $v_{Fp}^{*} = 0$ at $t^*=0$ (6.33)

After solid particles shoot out of the spout zone and enter fountain zone, their trajectories are tracked at each time step. Their velocity evolves with time due to gravity acceleration. Their distances from the dynamic top surface of the annular zone are calculated at each time step. When the distance equals to or less than zero, the particles enter the annular

zone. The total mass of solid particles at each time step is the sum of the mass of the particles staying in the fountain zone.

6.3.4 Annular zone

The rate of solids inflow to the annular zone equals the rate at which solids leave the fountain. Likewise the rate at which solids leave the annular zone equals the rate at which they enter the entrainment zone. A global mass balance requires that the total amount of solids in all zones remains constant, so at every instant in time the inventory of solids in the annular zone is just:

$$m_{Ap} = m_{Tp} - m_{Ep} - m_{Sp} - m_{Fp} \qquad (6.34).$$

Combining equations 6.25 and 6.26 with equation 6.34, the annular zone height can be obtained. So is spout zone which is assumed to equal to annular zone height.

The velocity of the solids in the annular zone is very small because of the large cross section and there are large and complex frictional forces at the walls, so a differential momentum balance is not very useful here. For purposes of this study, the solids inventory and height of this zone is sufficient and further details are not needed.

7. Characterization and validation of the low-order model

7.1 Characterization of the entrainment zone

As discussed previously, the initial contact between solids and gas occurs just above the gas inlet, and the subsequent dynamics in all the other zones can be viewed as a response to this initial interaction. The dynamic coupling between the zones is inherently one-way in the low-order model as it is currently defined, because there is no mechanism provided for dynamic feedback between the annular and entrainment zones (i.e., there is no way for changing conditions in the annular zone to affect what happens in the entrainment zone). Thus to understand the present model, it is possible to focus first on the entrainment zone by itself to study how the inlet gas energy is initially transferred to the bed solids. Later, the momentum and mass transfer between successive zones can be studied to understand how they act collectively.

The governing equations for the entrainment zone are the ODEs derived from the differential mass and momentum balances. The key parameters in these ODEs and their boundary conditions are inlet gas velocity, gas density and viscosity, particle size and density, settled void fraction, and the dimensionless quantities G and Lf, which represent the tendency for lateral solids and gas flow, respectively.

Because the governing ODEs in the entrainment zone cannot be solved analytically, their behavior was studied numerically for a range of parameter values. The two primary parameters varied in the spouted bed experiments were particle size and inlet gas velocity, so these parameters were varied in the numerical studies of the entrainment zone. The

range of particle sizes considered for the model was 200 to 800μm. Particle size can be expressed non-dimensionally by dividing the particle diameter by the assumed entrainment zone height. It was found to be convenient to express inlet velocity in terms of its ratio to the terminal particle velocity, u_t, and this ratio was varied from 0 to 4.

The ranges of the key remaining model parameters, the dimensionless solids and gas lateral flow parameters G and Lf, were unknown *a priori* and were varied by $0.1 \leq G \leq 1$ and $0.05 \leq Lf \leq -0.4$. These choices were later confirmed to be reasonable, as discussed below.

To simplify integration, H_E was held fixed at 0.35cm, but as noted below, this may be an inappropriate assumption in reality. Estimates of the actual value of H_E suggest that it can change with inlet gas flow. Particle density was held fixed at the experimental value of 5890 kg/m^3, and gas density was 1.172 kg/m^3. This yields a resulting particle-to-gas density ratio ($(\rho_p-\rho_g)/\rho_g$) of 5025. The settled particle void fraction was set to 0.46 and the gas viscosity to 1.86×10^{-5} kg/(m s) to match the experimental conditions.

Even with the above restrictions, an exhaustive mapping of the dynamics over the entire parameter space poses a daunting task because of the high dimensionality of the response surface. The approach used in this study instead focused on selecting a nominal reference condition and observing how the predicted dynamics shifted as one parameter at a time was varied and other parameters are ceteris paribus. The reference condition chosen was

d_p=0.5mm, u_E/u_t=1.5, G=0.6, and Lf=0.08. The dynamic trends in the entrainment zone were then observed as the above parameters were varied about this reference point.

Example results for void fraction and solids flow are summarized in Figures 7.1 to 7.16. From these plots (parenthetically referenced below), the following general observations may be made about how the predicted dynamics change as the key parameters deviate from the reference condition:

- As the dimensionless lateral solids flow parameter, G, increases (i.e., solids flow in more readily from the annulus), pulsation frequency (7.1) and amplitude (7.2 and 7.3) and solids circulation rate (7.4) trend up. These trends suggest that it is the effective 'flowability' of the solids that determines the intensity and frequency of the pulsations in the entrainment zone. Solids that flow readily tend to promote overall bed circulation.
- As the dimensionless lateral gas flow parameter, Lf, increases (more of the inlet gas leaks out to the annular zone), pulsation frequency (7.5) and mean solids circulation rate (7.8) trends down. Amplitude of pulsation frequency (7.6) and solid flow (7.7) increase with Lf. These trends suggest that bed design features (e.g., cone angle) or particle properties which promote lateral gas leakage will tend to lower pulsation and mean solid flow but increase fluctuation of both pulsation frequency and solid flow.

  The solid circulation rate is defined as below:

$$\frac{v_{Ep}(1-\varepsilon_E)}{u_t}$$

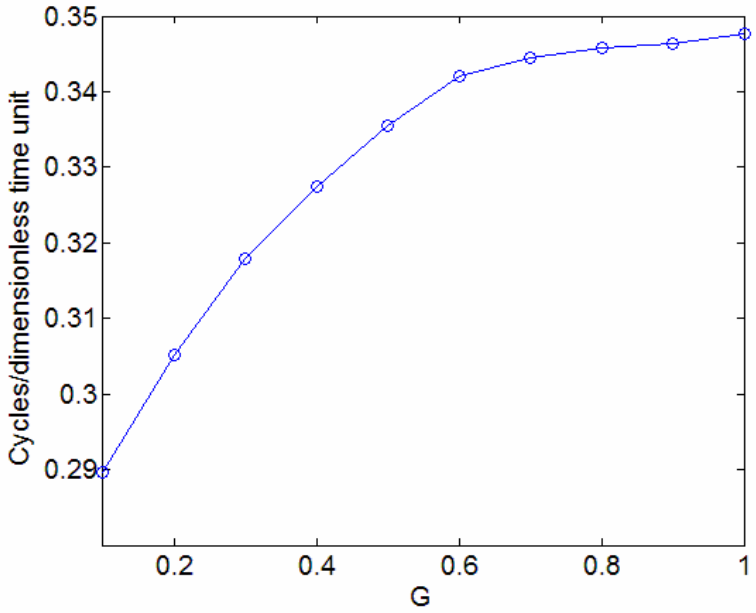

Figure 7.1 Dimensionless frequency of void fraction fluctuation in the entrainment zone *vs*. the lateral solids flow parameter, G (d_p = 0.5mm, Lf = 0.08 and u_E/u_t = 1.5).

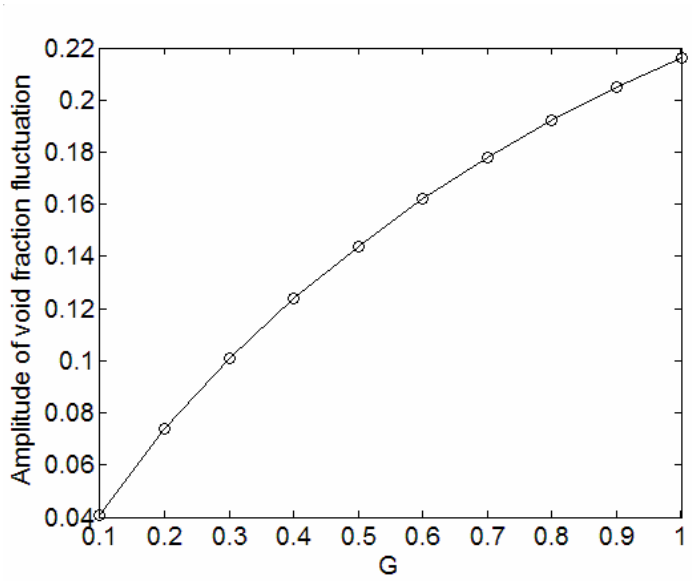

Figure 7.2 Amplitude of void fraction fluctuation *vs*. the lateral solids flow parameter, G (d_p = 0.5mm, Lf = 0.08 and u_E/u_t = 1.5).

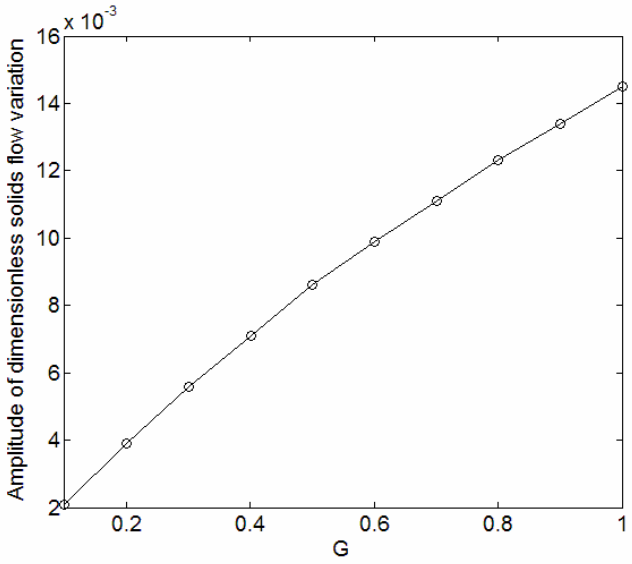

Figure 7.3 Amplitude of solids flow fluctuation *vs*. the lateral solids flow parameter, G (d_p = 0.5mm, Lf = 0.08 and u_E/u_t = 1.5).

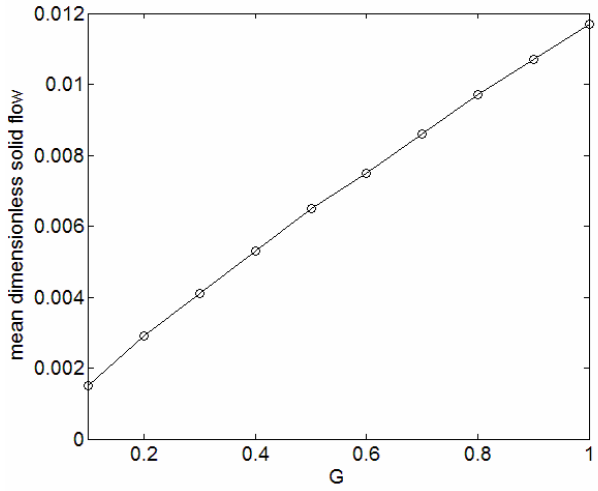

Figure 7.4 Mean dimensionless solid flow rate ($\frac{v_{Ep}}{u_t}(1-\varepsilon_E)$) *vs*. lateral solids flow parameter, G (d_p = 0.5mm, Lf = 0.08 and u_E/u_t = 1.5).

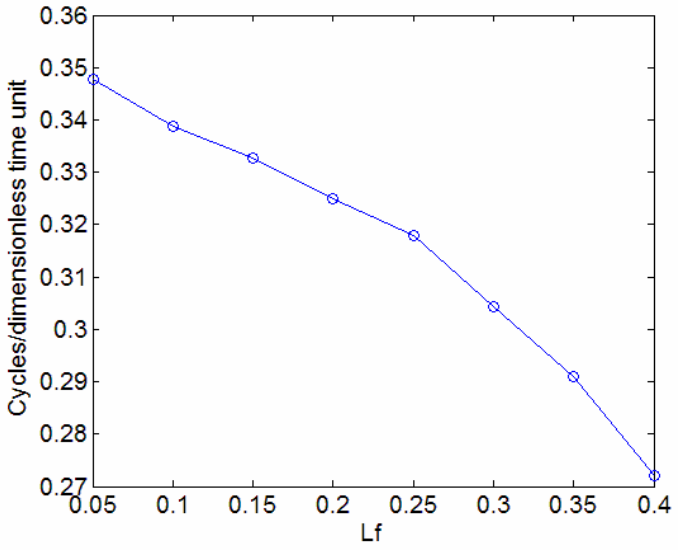

Figure 7.5 Dimensionless void fraction pulsation frequency *vs*. lateral gas flow parameter, Lf (d_p = 0.5mm, G = 0.6 and u_E/u_t = 1.5).

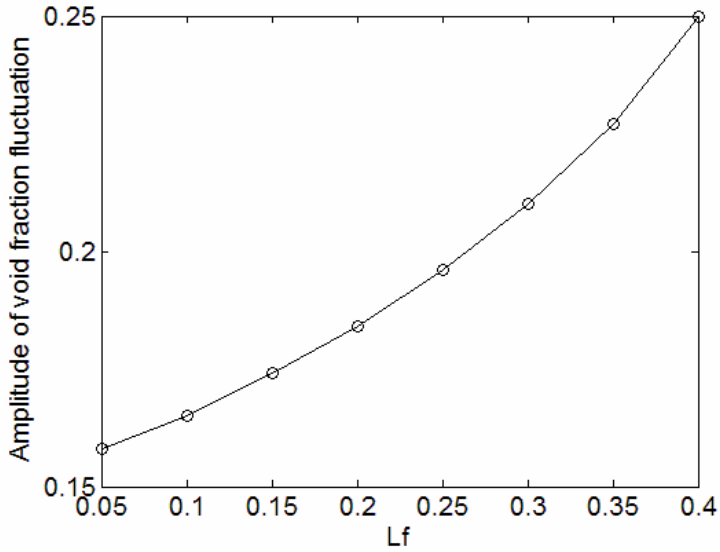

Figure 7.6 Void fraction pulsation amplitude *vs*. lateral gas flow parameter, Lf (d_p = 0.5mm, G = 0.6 and u_E/u_t = 1.5).

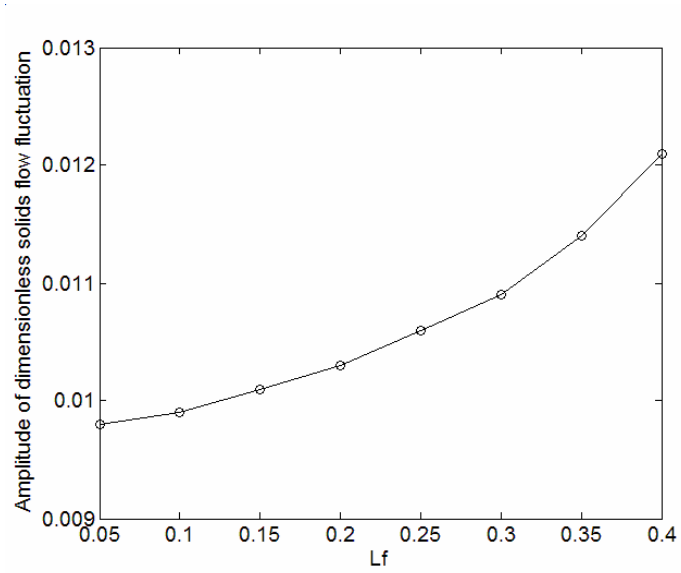

Figure 7.7 Solid flow pulsation amplitude *vs*. lateral gas flow parameter, Lf (d_p = 0.5mm, G = 0.6 and u_E/u_t = 1.5).

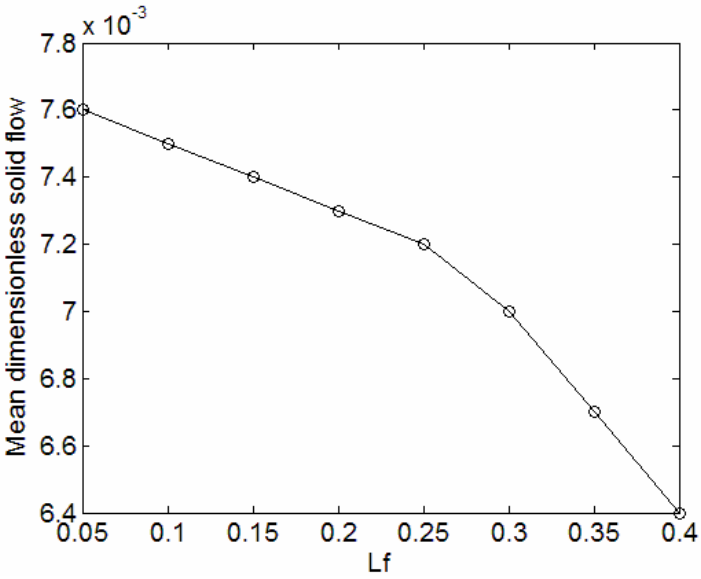

Figure 7.8 Mean dimensionless solid flow *vs*. lateral gas flow parameter, Lf (d_p = 0.5mm, G = 0.6 and u_E/u_t = 1.5).

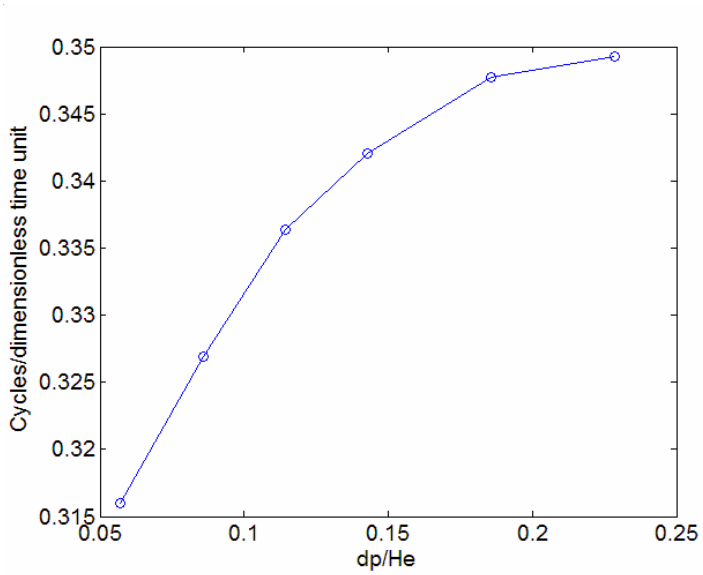

Figure 7.9 Frequency of the void fraction pulsation *vs.* particle size (G = 0.6, Lf = 0.08, and $u_E/u_t = 1.5$).

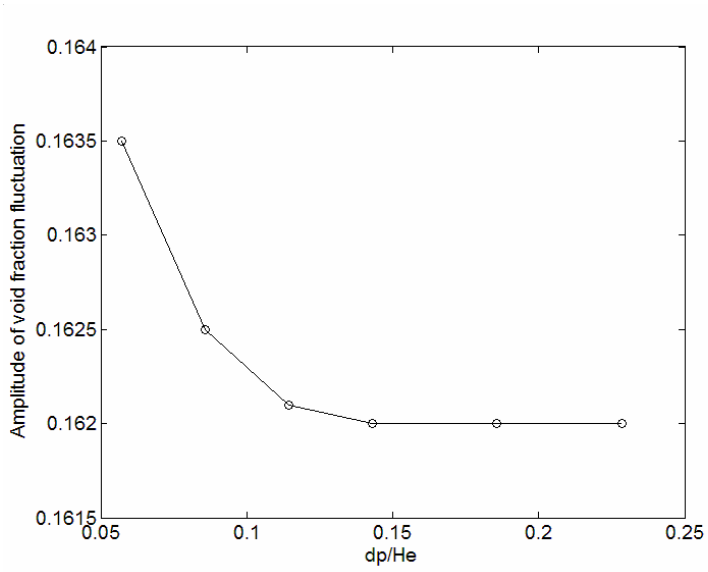

Figure 7.10 Amplitude of the void fraction pulsation *vs.* particle size (G = 0.6, Lf = 0.08, and $u_E/u_t = 1.5$).

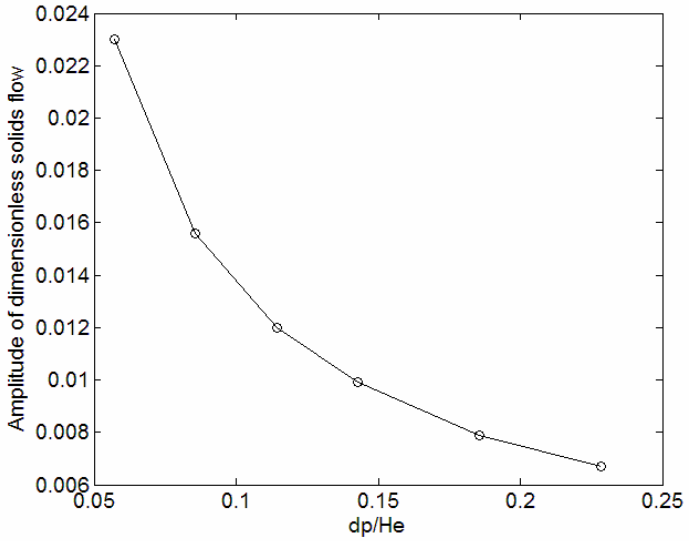

Figure 7.11 Amplitude of solid flow pulsation *vs*. particle size (G = 0.6, Lf = 0.08, and $u_E/u_t = 1.5$).

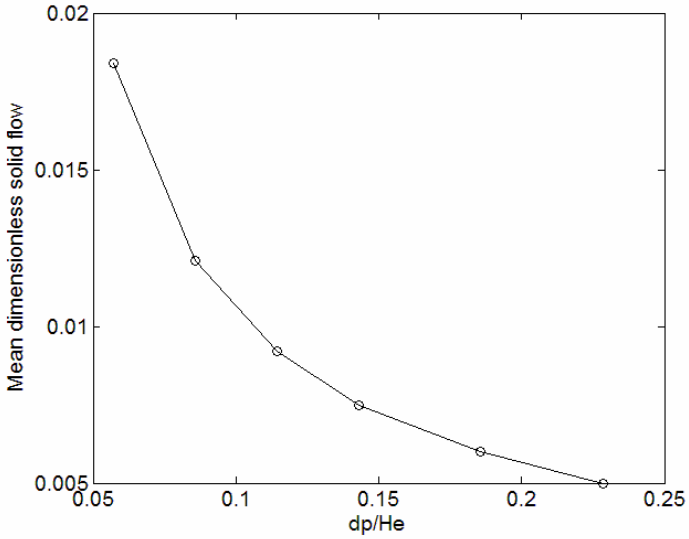

Figure 7.12 Mean dimensionless solid flow *vs*. particle size (G = 0.6, Lf = 0.08, and $u_E/u_t = 1.5$).

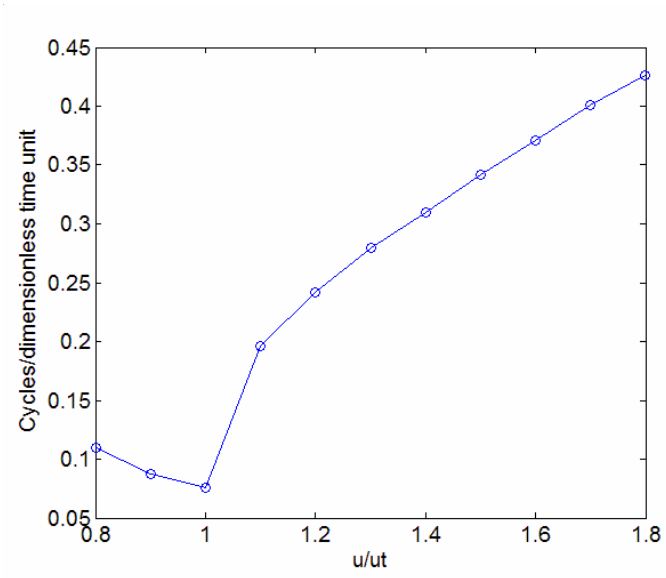

Figure 7.13 Frequency of void fraction pulsations *vs.* inlet gas velocity (G = 0.6, Lf = 0.08, and d_p = 0.5mm).

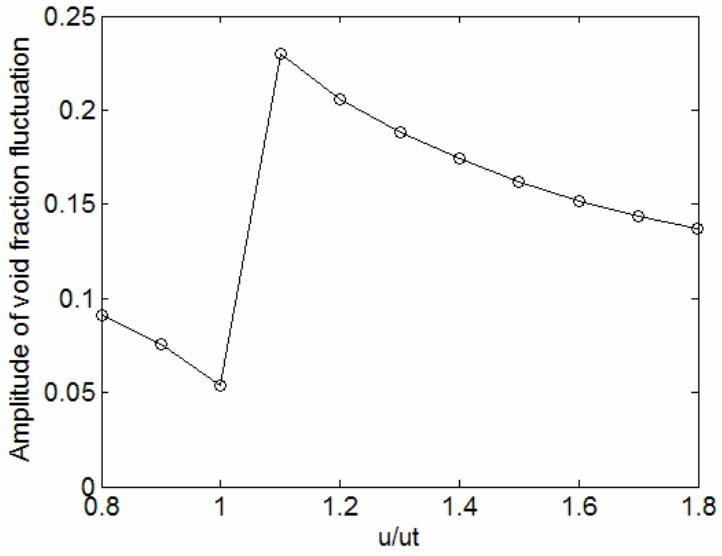

Figure 7.14 Amplitude of the void fraction pulsation *vs.* inlet gas velocity (G = 0.6, Lf = 0.08, and d_p = 0.5mm).

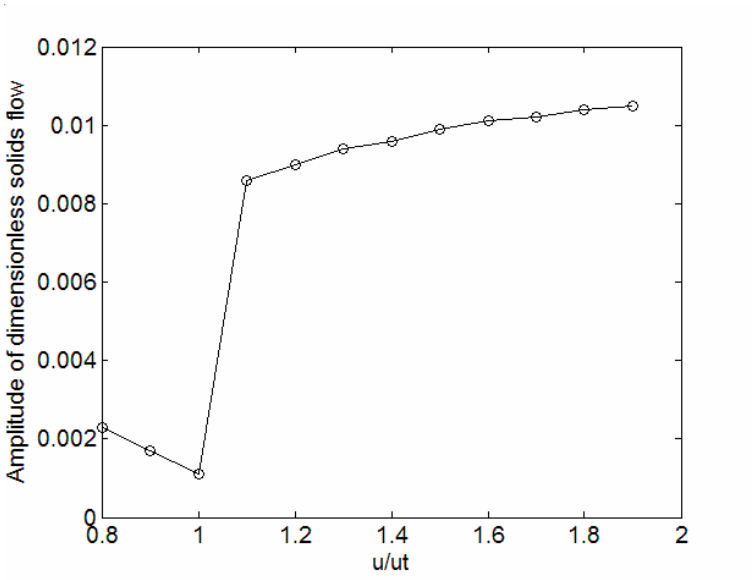

Figure 7.15 Amplitude of the solids flow pulsation *vs*. inlet gas velocity (G = 0.6, Lf = 0.08, and d_p = 0.5mm).

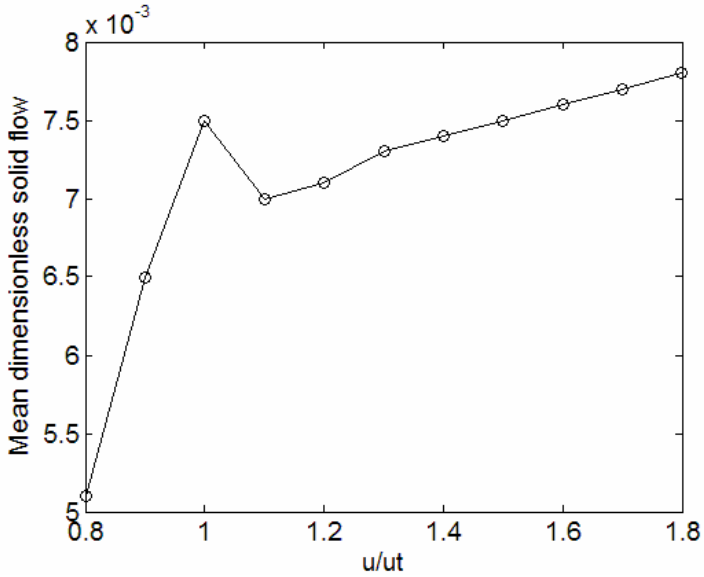

Figure 7.16 Mean solids flow *vs*. inlet gas velocity (G = 0.6, Lf = 0.08, and d_p = 0.5mm).

One period of the pulsation is defined as one cycle. The mean solid circulation is time-averaged solid circulation rather than per cycle.

- As particle size increases, pulsation frequency (7.9) increases while pulsation amplitude of solid flow (7.11) and void fraction (7.10) and solids circulation rate (7.12) all decrease.
- Pulsation frequency (7.13), pulsation amplitude (7.14), and mean solids flow (7.15) vary in complex ways with inlet gas velocity in the region $0.8 \leq u_E/u_t \leq 1.9$. At $u_E/u_t = 1$, the minimum pulsation frequency occurs. The mean solid flow steadily increases as $u_E/u_t > 1.1$ (7.16).

The onset of finite solids flow and a minimum in pulsation frequency $u_i/u_t = 1$ strongly suggest a connection to the minimum spouting velocity. If this same range of flow indeed corresponds to U_{ms}, it should be possible to make improved estimates for the physical dimensions of the entrainment zone based on experimentally observed values for U_{ms}. As an example, consider that the observed U_{ms} for 0.5mm ZrO_2 with a settled height of 3.5cm was 15.9m/s in the 60° conical bed (recall that this velocity was evaluated at the 0.4cm diameter inlet). On the other hand the entrainment zone model predicts that the onset of significant solids convection occurs at $u_E = u_t$ or approximately 6.4m/s. For these conditions to have the same volumetric flows, it is necessary that the entrainment zone diameter be approximately 0.63cm. This would seem to be a reasonable diameter for the entrainment zone considering that some expansion of the inlet gas stream would be

expected; this expansion was experimentally observed in trials with the glass cone. A similar expansion effect is also predicted by MFIX simulations of the experiment.

Another implication of the assumption of U_{ms} correspondence between the model and experiment is the connection between the observed and predicted pulsation frequencies. The minimum frequency predicted by the model is approximately 0.076 cycles/dimensionless time unit, while the minimum pulsation frequency observed experimentally was approximately 17 cycles/s. The two frequencies should be proportionally related by the characteristic time scale defined for the entrainment zone model, which is given by $\sqrt{H_E / g}$. In order for these two frequencies to be consistent, H_E must be approximately equal to 0.019cm. The height of entrainment zone needs to be equal or a little bit larger than particle size.

Just above U_{ms} on the other hand, the maximum dimensionless and experimental frequencies are about 0.2 cycles/dimensionless time unit and 10.4 cycles/s respectively. This implies that the effective value of H_E at this condition must be approximately 0.13cm. These results would seem to suggest that the height of the entrainment zone changes significantly with gas flow. In some sense it may not even be appropriate to think of the entrainment zone as a separate region for gas flows below U_{ms} because there would be no actual solids entrainment. Instead the solids essentially oscillate in place as the gas passes through. For flows above U_{ms}, it would seem reasonable that the entrainment zone height might parallel the expansion of the fountain height (which varies approximately proportional to u_i/U_{ms} as discussed previously). One might also consider

that the effective values of G and Lf probably vary with flow as well, although the model does not indicate such a strong correlation between these parameters and pulsation frequency.

7.2 Characterization of the combined multi-zone model

As discussed above, the initial interaction between the solid particles and incoming gas begins in the entrainment zone and then propagates through the spout, fountain, and annulus zones. The combined model is constructed such that all of the subsequent particle and gas flows in these latter zones are responses to processes that begin in the entrainment zone. The dominance of the entrainment zone in the combined model is further emphasized by the fact that this zone has most of the adjustable parameters.

The results of an example simulation including the interaction of all the zones is illustrated in Figures 7.17 through 7.19 for the case where H_0 = 3.5cm, G= 0.6, Lf = 0.08, u_i = 23.87m/s, D_E= 0.63cm and H_E= 0.35cm.

As before, it is useful to consider how important features of the combined model behave as key parameters are varied. Again for simplicity, the model predictions (in this case for all zones together) are plotted as each entrainment parameter is varied and the other parameters are held fixed at nominal values of d_p = 0.5mm, H_E = 0.35cm, G = 0.6, Lf = 0.08, u_i = 23.87m/s, H_0 = 3.5cm and D_E= 0.63cm.

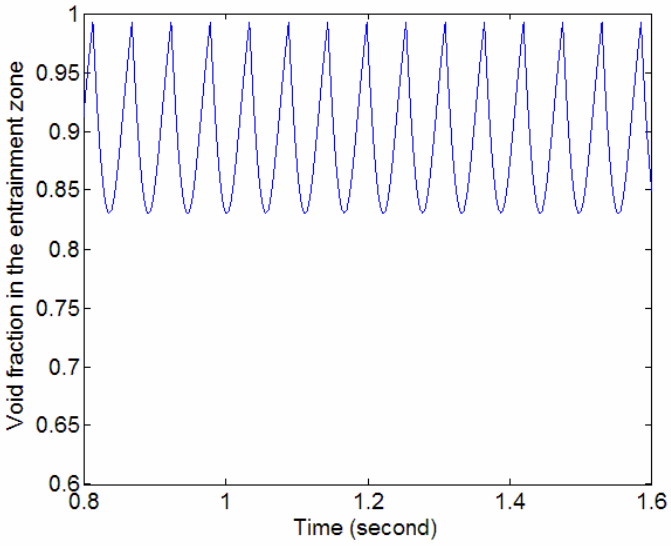

Figure 7.17 Void fraction in entrainment zone vs. time for d_p = 0.5mm, H_0 = 3.5cm, G= 0.6, Lf = 0.08, u_i = 23.87m/s, D_E= 0.63cm and H_E= 0.35cm.

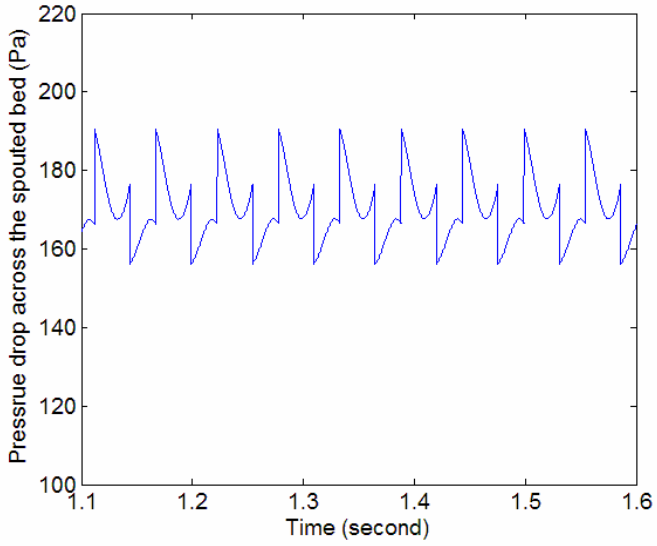

Figure 7.18 Air pressure drop across the spouted bed vs. time for d_p = 0.5mm, H_0 = 3.5cm, G= 0.6, Lf = 0.08, u_i = 23.87 m/s, D_E= 0.63cm and H_E= 0.35cm.

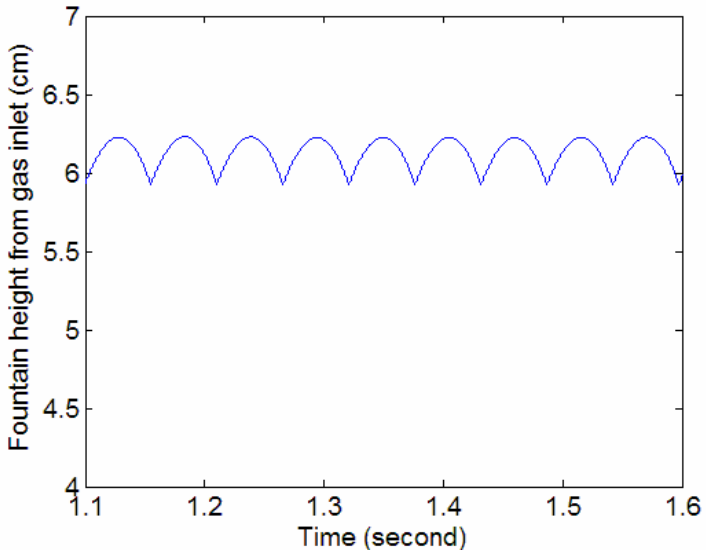

Figure 7.19 Fountain height vs. time for d_p = 0.5mm, H_0 = 3.5cm, G = 0.6, Lf = 0.08, u_i = 23.87m/s, D_E = 0.63cm and H_E = 0.35cm.

Figures 7.20-7.22 illustrate the predicted trends in overall average pressure drop, pressure pulsation frequency, and fountain height, respectively, with the granular flow parameter G. All of these results suggest that solids which flow more readily from annulus into the entrainment zone tend to more readily couple with the fluid flow, thereby creating a more fluid-like dynamics.

Figures 7.23 through 7.25 summarize the predicted multi-zone trends with variations in the lateral inlet gas flow parameter, Lf. Average pressure drop (Figure 7.23) increases with Lf while both pulsation frequency and fountain height decrease with lateral gas leakage. All of these trends seem reasonable considering that higher Lf implies more gas by-passing of the spout zone. Gas that bypasses the spout must move through the

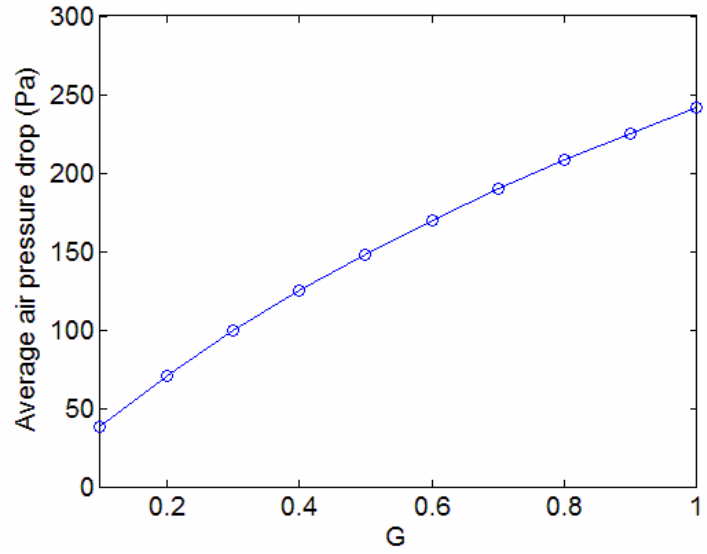

Figure 7.20 Average air pressure drop across the spouted bed vs. G for the combined model at d_p = 0.5mm, H_0 = 3.5cm, Lf = 0.08, u_i = 23.87m/s, D_E= 0.63cm and H_E= 0.35cm.

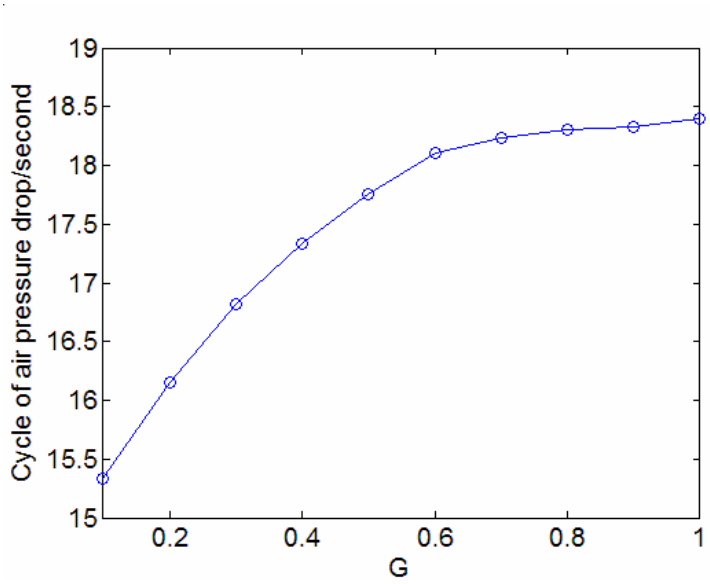

Figure 7.21 Pulsation frequency vs. G for the combined model at d_p = 0.5mm, H_0 = 3.5cm, Lf = 0.08, u_i= 23.87m/s, D_E= 0.63cm and H_E= 0.35cm.

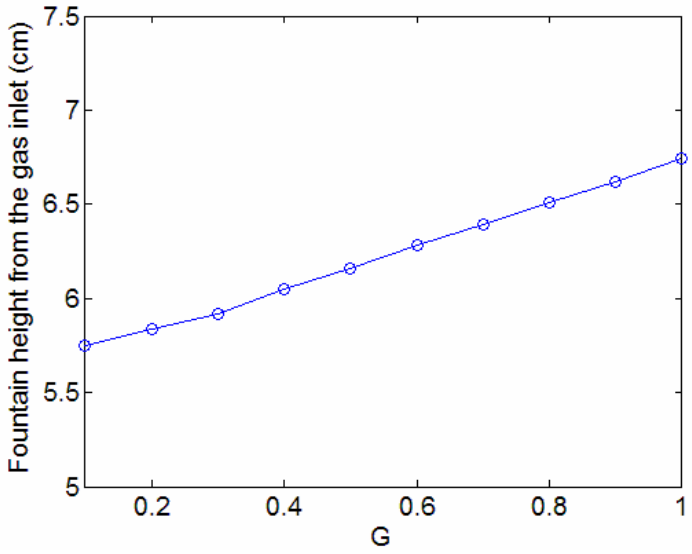

Figure 7.22 Fountain height vs. G for the combined model at d_p = 0.5mm, H_0 = 3.5cm, Lf = 0.08, u_i = 23.87m/s, D_E = 0.63cm and H_E = 0.35cm.

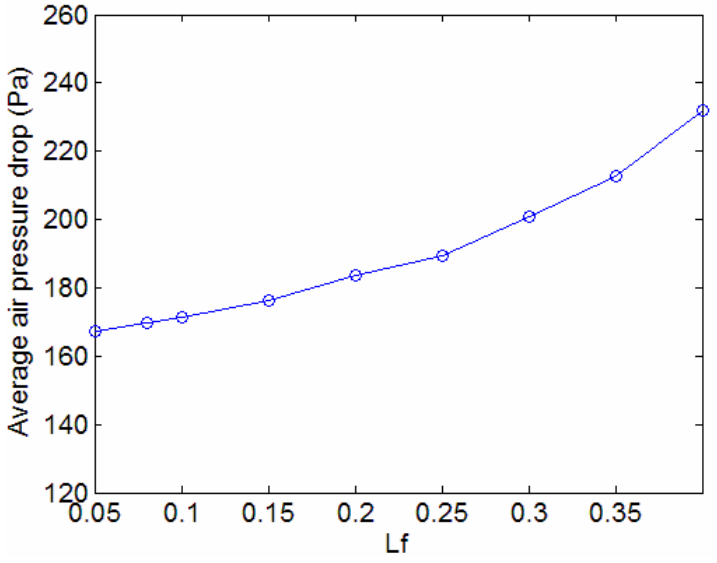

Figure 7.23 Predicted average pressure drop for the combined model vs. Lf at d_p = 0.5mm, H_0 = 3.5cm, G = 0.6, u_i = 23.87m/s, D_E= 0.63cm and H_E = 0.35cm.

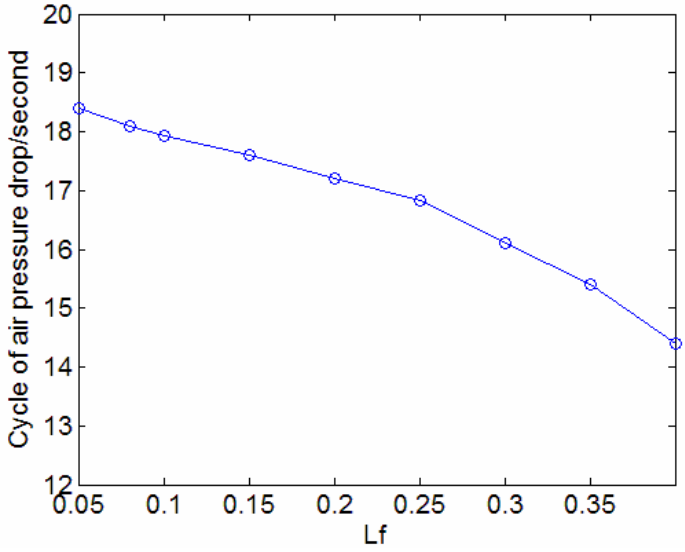

Figure 7.24 Predicted pressure pulsation frequency for the combined model vs. Lf at d_p = 0.5mm, H_0 = 3.5cm, G = 0.6, u_i = 23.87m/s, D_E = 0.63cm and H_E = 0.35cm.

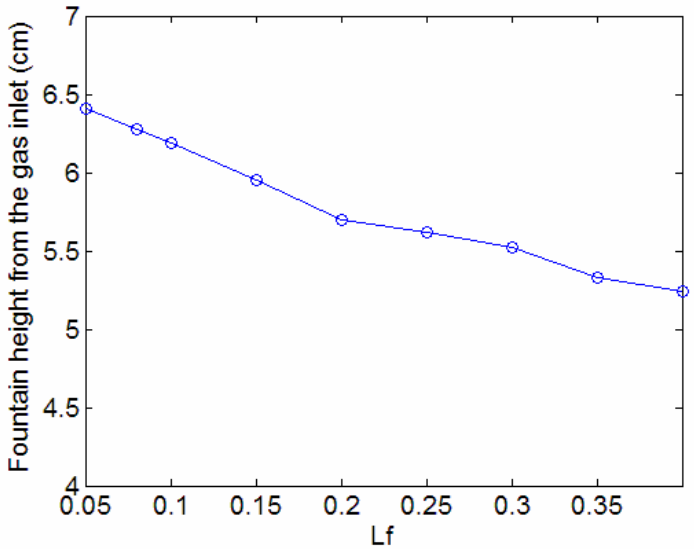

Figure 7.25 Predicted fountain height for the combined model vs. Lf at d_p = 0.5mm, H_0 = 3.5cm, G = 0.6, u_i = 23.87m/s, D_E = 0.63cm and H_E = 0.35cm.

annulus, which has a much higher solids fraction and thus higher pressure drop. As gas bypassing increases, there is also less energy available for particle entrainment and the associated pulsation process.

While the general behavior illustrated above appears reasonable, it is important to make more direct comparisons with experimental observations to determine if the model is behaving properly. One way to make such comparisons is to consider how important spouted bed features behave as key experimental parameters are varied. The following discussion specifically focuses on the trends predicted by the combined model with changes in inlet gas flow. Again for simplicity, the model predictions (in this case for all zones together) are evaluated as gas flow is varied and the other parameters are held fixed at nominal values of d_p = 0.5mm, G = 0.6, Lf = 0.08, H_0 = 3.5cm, D_E = 0.63cm and H_E = 0.35cm.

Figures 7.26-7.28 compare model predicted trends with experimental trends with variations in inlet air flow. There appears to be, *prima facie*, considerable disagreement between the trends with air flow (7.26). For example, the experimental pressure drop effectively remained constant for inlet flows above U_{ms}, but the multi-zone model predicts a continually decreasing pressure drop. One potential explanation for this discrepancy might be that the dimensions of the entrainment and/or spout zones or the parameters G and Lf do change with flow above U_{ms}, as expected in the discussions above.

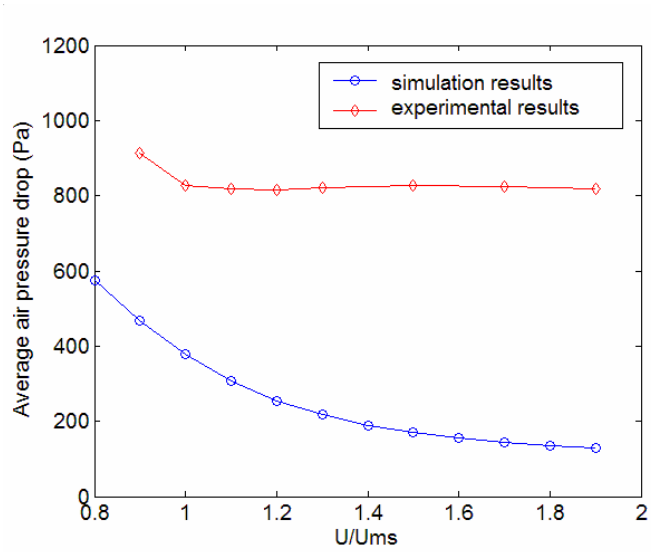

Figure 7.26 Predicted air pressure drop of the combined model compared with experimental results for d_p = 0.5mm, H_0 = 3.5cm, G = 0.6, Lf = 0.08, D_E = 0.63cm and H_E= 0.35cm.

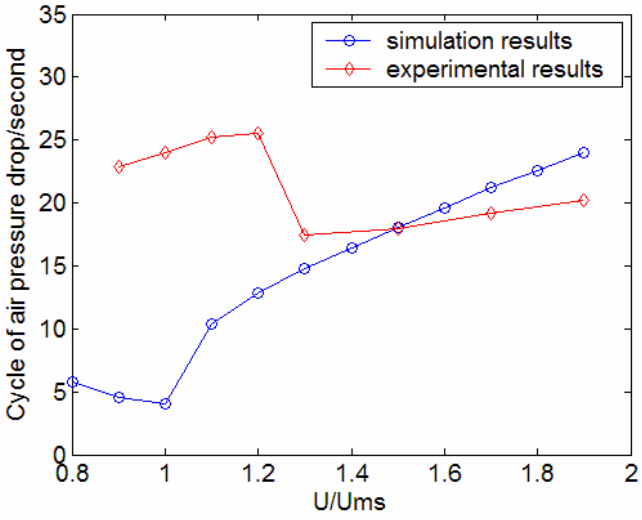

Figure 7.27 Predicted pressure pulsation frequency of the combined model compared with the experimental results for d_p = 0.5mm, H_0 = 3.5cm, G = 0.6, Lf = 0.08, D_E = 0.63cm and H_E = 0.35cm.

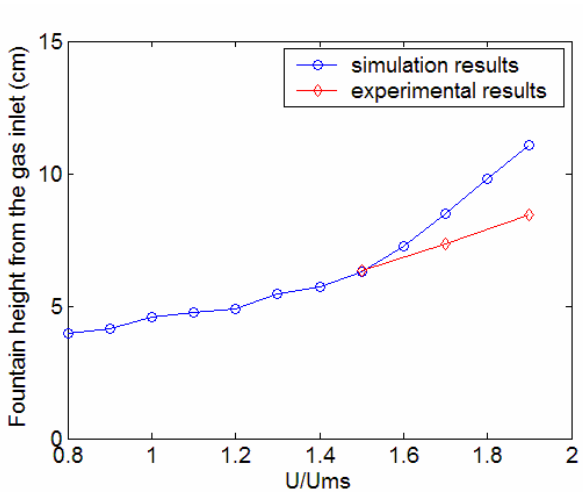

Figure 7.28 Predicted H_f for the combined model compared with experimental results for d_p = 0.5mm, H_0 = 3.5cm, G = 0.6, Lf = 0.08, D_E = 0.63cm and H_E = 0.35cm.

As discussed in Section 7.1, one might assume that at least some of the five model parameters (D_E, H_E, D_S, G and Lf) are actually functions of the gas flow. This assumption would seem especially plausible for the physical dimensions of the entrainment and spout zones because these regions appear visually to expand with increasing gas flow [San José, 2005b]. This expansion process also appears to be supported by the predictions of CFD models such as MFIX [Pannala, 2006]. To investigate how variations in the sizes of the entrainment and spout zones might be used to reconcile the combined model predictions with the experimental trends, the height of entrainment zone (H_E) and the diameter of the spout zone (D_S) were adjusted to match the predicted and observed values of the pulsation frequency and fountain height, respectively. The resulting match between model predictions and experimental observations are illustrated in Figures 7.29 and 7.30.

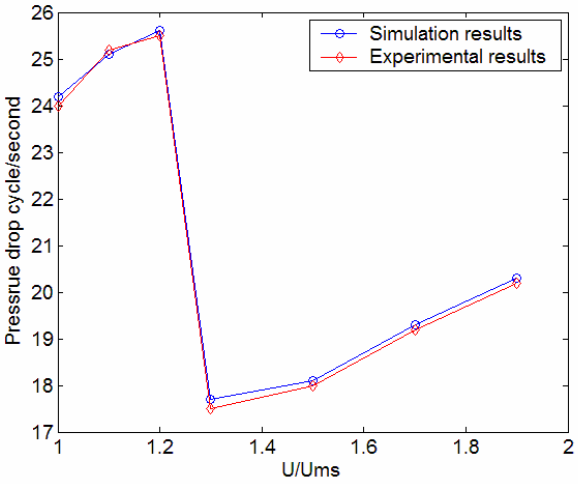

Figure 7.29 Comparison of pulsation frequency predicted by the combined model with experimental results for d_p = 0.5mm, H_0 = 3.5cm, G = 0.6, and Lf = 0.08. Values for the parameters H_E and D_S are listed in Table 7.1.

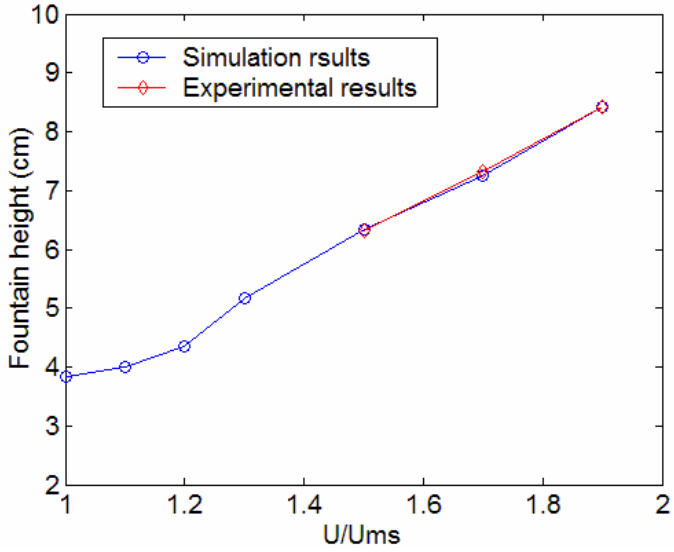

Figure 7.30 Comparison between the predicted air fountain height from the combined model with experimental results for d_p = 0.5mm, H_0 = 3.5cm, G = 0.6, and Lf = 0.08. Values for the parameters H_E and D_S are listed in Table 7.1.

The variations in H_E and D_S required to give the good model-experiment agreement shown in Figures 7.29 and 7.30 are listed in Table 7.1. As expected, it appears necessary for these dimensions to increase in order to correctly capture the observed trends in frequency and fountain height. The relative smoothness of the dimension variations seems physically plausible and suggests that simple correlations might be developed for these dimensions using experimental measurements and/or CFD simulations. Also, the variation in D_S is so small one might conclude that it is effectively constant, making H_E the only dimension to vary significantly with gas flow. This implies again that the entrainment zone is dominating the overall spout dynamics.

Conversely, the magnitudes of the predicted and measured average pressure drops are still considerably different, although the trends are similar as illustrated in Figure 7.31. This result indicates that the pressure drop produced by gas-particle interactions at the outer boundary of the spout zone (i.e., the spout 'wall') adds considerably to the overall pressure drop. As this 'wall drag' is currently not included in the combined model, it would appear that its addition is clearly appropriate and a subject for future investigations.

It seems fair to conclude that numerical studies such as those described above suggest that it should be possible to improve the combined-zone low order model by accounting for variations in the entrainment zone dimension and G and Lf with gas flow and by adding appropriate drag terms in the spout zone to account for gas and particle

Table 7.1 Values of H_E and D_S used in the simulations depicted in Figures 7.29 and 7.30 (G = 0.6, Lf = 0.08, D_E = 0.63cm)

u/U_{ms}	1	1.1	1.2	1.3	1.5	1.7	1.9
H_E(cm)	0.054	0.077	0.1	0.25	0.35	0.43	0.48
D_S(cm)	0.63	0.63	0.63	0.63	0.64	0.67	0.7

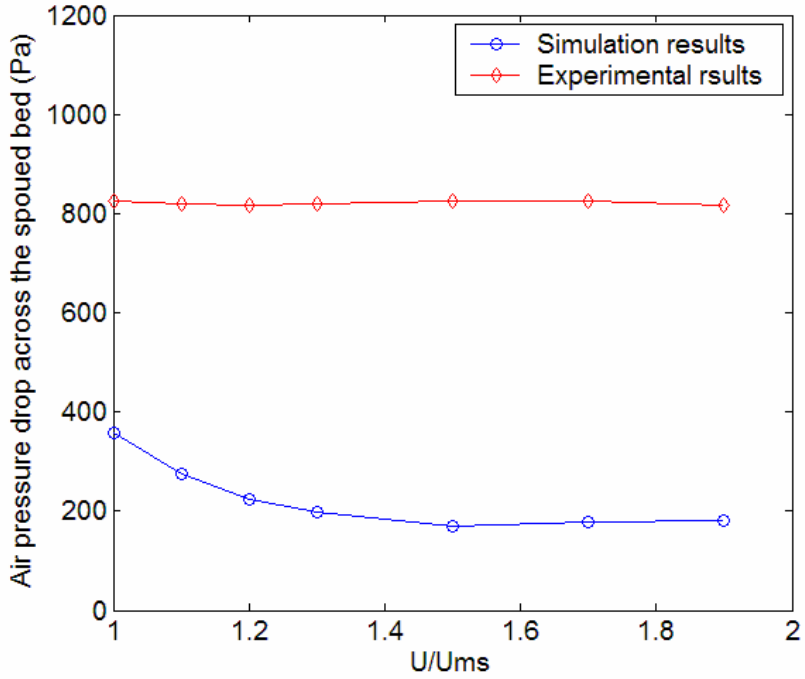

Figure 7.31 Comparison of average pressure drop predicted by the combined model with experimental results for d_p = 0.5mm, H_0 = 3.5cm, G = 0.6, Lf = 0.08, and D_E = 0.63cm.

interactions with the spout 'wall'. Because of the large number of possible values for the individual parameters and the difficulty of directly validating these values experimentally, it appears that a reasonable course for future studies should include CFD simulations. Such simulations could provide details unavailable from experiments that could be used to directly validate not only the effective parameter values used in the low-order model but also the key predictions of the model including the pulsation frequency, the rate of solids circulation, the pressure drop, and the fountain height. The use of CFD models would also allow the development of a detailed understanding of the physics behind these lumped low-order parameters.

One other suggested area for future research is the complex nature of the entrainment process itself. Although the present combined low-order model predicts that the pulsating flow that drives particle circulation is periodic, experimental observations clearly indicate that the dynamics are more complex. In particular, the pulsations appear to undergo bifurcations and complex variations that indicate deterministic chaos [Daw, 2007]. The only way this could occur in the present combined model would be by the addition of a feedback term connecting the each pulsation cycle with the residual effects of previous cycles. Such feedback could be expressed in terms of time-delay differential equations, such as those used to model the production of white blood cells [Glass and Mackey, 1988]. One plausible physical process by which feedback could occur in the entrainment process would be in hysteretic variations of the lateral granular and gas flows associated with the recovery phase of the pulsation cycle. Specifically, changes in the effective values of G and Lf associated with recent past history (e.g., by a time-delay mechanism)

could produce such a feedback. It is suggested this possibility should be a prominent consideration in future studies.

8. Conclusions and recommendations

The hydrodynamics of shallow, conical spouted beds of heavy particles was experimentally studied to determine differences from previous spouted bed reports in the literature. Key experimental measurements included minimum spouting velocity, time-average and time-varying (dynamic) pressure drop, time-average fountain height and time-average gas velocity profile in the bed. New correlations were developed for minimum spouting velocity and time-average pressure drop based on the experimental data. A previously reported correlation for fountain height appears to do a good job of representing the present observations. The time-average gas velocity profile measurements confirmed that the beds in the present study exhibited gas flow features that were at least qualitatively similar to those previously reported for other experimental conical spouted beds and predicted by detailed computational fluid dynamics models.

Key experimental observations regarding the time-varying pressure-drop measurements for the particles and beds in question include the following:

- For gas flows above the minimum spouting condition, there is always a significant level of pressure pulsation, which is observed to closely correlate with pulsations in solids circulation.
- The pulsations appear to originate at the gas inlet in the apex of the cone where the gas and solids first contact, and the remaining motion on the bed appears to be a response to the propagation of these pulsations.

- For gas flows above or below the minimum spouting condition, there appears to be a single dominant pulsation frequency with a modest amount of spreading in the Fourier spectrum.
- For gas flow below the minimum spouting condition, small-amplitude, higher-frequency pressure pulsations are observed, which appear to correlate with small up-and-down vibrations of particles (with no net motion).
- Near the minimum spouting condition, two distinct pulsation frequencies are present and appear to exchange dominance in some type of bifurcation as the gas flow increases.
- The net effect of the pulsation bifurcation near minimum spouting is to cause the dominant pulsation frequency to drop abruptly as gas flow increases, and this seems to be a reliable indicator of spouting onset.
- The standard deviation, skewness, and kurtosis of the pulsations also shift abruptly at the minimum spouting condition, providing additional indicators for spouting detection.
- The pulsation frequency decreases with increasing cone angle and particle size but does not change much with static bed height.

At least some of the major features of the observed spouted bed pulsation behavior appear to be captured by a simple zone-based ODE model. The ODEs are derived from time-differential mass and momentum balances over 4 spatial zones: entrainment, spout, fountain, and annulus. The dynamic behavior of the model is dominated by the entrainment zone, which includes the effects of 3 key processes:

- Granular particle flow from the annulus into the area immediately above the gas inlet;
- Radial leakage of gas outward from the inlet zone in response to the inward flowing particles and;
- Upward flow of the main part of the inlet gas and subsequent particle entrainment in response to the gas-particle drag.

Two new (non-standard) dimensionless groups are required by this model to represent the granular flow and radial air leakage processes, respectively.

While qualitatively realistic pulsation and time-average behavior appears to be produced by this model, more study is needed to confirm its usefulness and improve its accuracy. Specifically, the following issues are recommended as fruitful topics for future study:

- It appears that the effective dimensions of the entrainment zone change with deviations from the minimum spouting condition. Development of experimental measurements, correlations, and physical models for these effective size changes would be highly useful in improving the model.
- The physics behind the dimensionless parameters associated with granular flow into the entrainment zone and radial leakage of gas out are poorly understood at the moment. Development of experimental measurements, correlations, and physical models for these processes would also be highly useful for understanding how the parameters change with bed design and particle properties.

- Radial gas leakage from the spout zone is not included in the present model, although it is expected to be a key factor, especially for deeper beds.
- The present model is limited in its ability to capture feedback effects in the solids circulation because there is no dynamic coupling between the states of the annulus and entrainment zones. In reality, one expects that there is indeed an important impact of the solids packing condition in the annulus on the entrainment process, and this needs to be included in an improved model. One obvious effect of adding this effect will be to introduce the possibility of time-delay feedback on the entrainment dynamics, which is known to produce higher-dimensional nonlinear effects and chaos in other contexts.
- While experimental investigation of the above issues is likely to present considerable challenges, it is highly likely that the use of computational fluid dynamics codes such as MFIX can be very effective tools for unraveling the details that are hard to observe physically. Thus the use of such codes for conducting numerical experiments to understand solids entrainment and circulation, gas bypassing, and particle trajectories in the fountain and annulus should be highly productive.

References

Abdelrazek, I. D., An analysis of thermo-chemical deposition in spouted beds. Ph.D. thesis, University of Tennessee, Knoxville, 1969.

Aravinth, S. and Murugesan, T., General correlation for the minimum spouting velocity. *Bioprocess Engineering* **16**, 289–293, 1997.

Atkins, R. T., Summary of coating laboratory process development. GA-P-390-33, GA Internal Memo, June 25, 1969.

Beatty, R. L., Carlsen, F. A. Jr. and Cook, J. L., Pyrolytic-carbon coating on ceramic fuel particles. *Nuclear Applications* **1**, 560–566, 1965.

Becker, H. A., An investigation of laws governing the spouting of coarse particles. *Chemical Engineering Science* **13**, 245–262, 1961.

Bi, H., Macchi, A., Chaouki, J. and Legros, R., Minimum spouting velocity of conical spouted beds. *Canadian Journal of Chemical Engineering* **75**, 460–465, 1997.

Bi, H., A discussion on minimum spout velocity and jet penetration length. *Canadian Journal of Chemical Engineering* **82**, 4–10, 2004.

Broadhurst, T. E., *Particle Oscillation in Fluidized Beds*. **Encyclopedia of Fluid Mechanics**, Gulf, Houston, vol. 4, 781–815, 1986.

Cecen, A., The maximum spoutable bed heights of fine particles spouted with air. *Canadian Journal of Chemical Engineering* **72**, 792–797, 1994.

Chen, J. J. J. and Lam, Y. W., An analogy between the spouted bed phenomena and the bubbling-to-spray transition. *Canadian Journal of Chemical Engineering* **61**, 759–762, 1983.

Choi, M. and Meisen, A., Hydrodynamics of shallow, conical spouted beds. *Canadian Journal of Chemical Engineering* **70**, 916–924, 1992.

Daw, C. S., personal communications, 2005.

Daw, C. S., personal communications, 2007.

Day, J.-Y., The fountain height and particle circulation rate in a spouted bed, *Chemical Engineering Science* **45**, 2987–2990, 1990.

Fane, A. G. and Mitchell, R. A., Minimum spouting velocity of scaled-up beds. *Canadian Journal of Chemical Engineering* **62**, 437–439, 1984.

Freitas, L. A. P., Dogan, O. M., Lim, C. J., Grace, J. R. and Bai, D., Identification of flow regimes in slot-rectangular spouted beds using pressure fluctuation. *Canadian Journal of Chemical Engineering* **82**, 60–73, 2004.

Fryer, C. and Potter, O. E., Experimental investigation of models for fluidized bed catalytic ceactors. *AIChE Journal* **22**, 38–47, 1976.

Gay, E., Nelson, G. L. and Clary, B. L., Air flow requirements and bed turnover time for a spouted bed peanut drier. Meeting of the American Society of Agricultural Engineers Paper No. 70-309., Minneapolis, 1970.

Ghosh, B., A study of the spouted bed. Part I A theoretical analysis. *Indian Chemical Engineering* **1**, 16–19, 1965.

Goltsiker, A. D., Ph.D. thesis, Lensovet Technology Institute, Leningrad, Russia, 1967. (Quoted in Mathur and Epstein (1974b))

Gorshtein, A. E. and Muknlenov, I .P., Critical speed of gas corresponding to the beginning of spouting. *Zhurnal Prikladnoi Khimii* **37**, 1887–1893, 1964. (Quoted in Mathur and Epstein (1974b))

Grace, J. R. and Mathur, K. B., Height and structure of the fountain above the spouted beds. *Canadian Journal of Chemical Engineering* **56**, 533–537, 1978.

Gyarmati, E., Mehner, A. W. and Wallura, E., 4th Europe Conference on Chemical Vapor Depositions. Eindhoven, 312–320, 1983.

Gyarmati, E. and Nickel, H., JUEL-900-RW[1972] 1/71, C.A. 78, NO154090, 1973. (Cited by Heit, W (1986))

Heit, W. "SIC in Nuclear Technology," **Gmelin Handbook of Inorganic Chemistry, Silicon Supplement** Vol. B3, 478–500, 1986.

Kmiec, A., Expansion of solid-gas spouted bed. *Chemical Engineering Journal* **13**, 143-147, 1977.

Kmiec, A., The minimum spouting velocity in conical beds. *Canadian Journal of Chemical Engineering* **61**, 274–280, 1983.

Knowlton, T. M., Karri, S. B. R. and Issangya, A., Scale-up of fluidized-bed hydrodynamics. *Powder Technology* **150**, 72–77, 2005.

Lauf, R. J. and Braski, D. N., ORNL-TM-7209[1980] 1/40, C. A., 93, No. 193909, 1980. Oak Ridge National Laboratory Technical Report ORNL-TM-7209.

Limtrakul, S., Boonsrirat, A. and Vatanatham, T., DEM model and simulation of a catalytic gas-solid fluidized bed reactor: a spouted bed as a case study. *Chemical Engineering Science* **59**, 5225–5231, 2004.

Lu, H., He, Y., Liu, W., Ding, J., Gidaspow, D. and Bouillard, J., Computer simulations of gas-solid flow in spouted beds using kinetic-frictional stress model of granular flow. *Chemical Engineering Science* **59**, 865–878, 2004.

Madonna, L. A. and Lama, R. F., The derivation of an equation for predicting minimum spouting velocity. *AIChE Journal* **4**, 497–498, 1958.

Malek, M. A. and Lu, B. C. Y., Pressure drop and spoutable bed height in spouted beds. *Industrial and Engineering Chemistry Process Design and Development* **4**, 123–128, 1965.

Mamuro, T., and Hattori, H., Flow pattern of fluid in spouted beds, *Journal of Chemical Engineering of Japan* **1**, 1–5, 1968.

Manurung, F., Studies in the spouted bed technique with particular reference to low temperature coal carbonization. Ph.D. thesis, University of New South Wales, Kensington, Australia, 1964.

Markowski, A. and Maminski, W., Hydrodynamic characteristics of jet-spouted beds. *Canadian Journal of Chemical Engineering* **61**, 377–381, 1983.

Mathur, K. B. and Epstein, N., Dynamics of spouted beds. *Advances in Chemical Engineering* **9**, 111–191, 1974a.

Mathur, K. B. and Epstein, N., **Spouted Beds**. Academic Press, New York, 1974b.

Mathur, K. B. and Gishler, P. E., A technique for contacting gases with solid particles. *AIChE Journal* **1**, 157–164, 1955.

Morgan, M. H. III and Littman, H., Predicting the maximum spoutable height in spouted beds of irregular shaped particles. *Industrial and Engineering Chemistry Fundamentals* **21**, 23–26, 1982.

Mukhlenov, I. P. and Gorshtein, A. E., Hydraulic resistance of the suspended layer in grateless conical sets. *Zhurnal Prikladnoi Khimii* **37**, 609, 1964. (Quoted in Mathur and Epstein (1974b))

Mukhlenov, I. P. and Gorshtein, A. E., Investigation of a spouting bed. *Khimicheskaya Promyshlennost* **41,** 443-446, 1965 (Quoted in Mathur and Epstein (1974b))

Nikolaev, A. M. and Golubev, L. G., Basic hydrodynamic characteristics of the spouting bed. *Khimiya i Tekhnologiya Topliv i Masel* **7**, 855–867, 1964. (Quoted in Mathur and Epstein (1974b))

Olazar, M., San José, M. J., Aguayo, J. M. and Bilbao, J., Stable operation conditions for gas-solid contact regimes in conical spouted beds. *Industrial and Engineering Chemistry Research* **31**, 1784–1792, 1992.

Olazar, M., San José, M. J., Aguayo, A. T., Arandes, J. M. and Bilbao, J., Pressure drop in conical spouted beds. *Chemical Engineering Journal* **51**, 53–60, 1993.

Olazar, M., San José, M. J., Aguayo, J. M. and Bilbao, J., Hydrodynamics of nearly flat base spouted beds. *Chemical Engineering Journal* **55**, 27–37, 1994a.

Olazar, M., San José, M. J., Penas, F. J., Arandes, J. M.and Bilbao, J., Gas flow dispersion in jet-spouted beds. *Industrial and Engineering Chemistry Research* **33**, 3267–3273, 1994b.

Olazar, M., San José, M. J., Llamosas, R., Alvarez, S. and Bilbao, J., Study of local properties in conical spouted beds using an optical fiber probe. *Industrial and Engineering Chemistry Research* **34**, 4033–4039, 1995a.

Olazar, M., San José, M. J. , Aguayo, A. T. Arandes, J. M. , and Bilbao, J., A simplified model for gas flow in conical spouted bed. *Chemical Engineering Journal* **56**, 19-25, 1995b.

Olazar, M., San José, M. J., Aguayo, J. M. and Bilbao, J., Solid flow in jet spouted beds. *Industrial and Engineering Chemistry Research* **35**, 2716–2724, 1996.

Olazar, M., San José, M. J., Izquierdo, M. A., Salazar, A. O. de and Bilbao, J., Effect of operations on solid velocity in the spout, annulus and fountain of spouted beds. *Chemical Engineering Science* **56**, 3585–3594, 2001.

Pallai, I. and Nemeth, J., Measurement and regulation of particle residence time in spouted bed driers. Third International Congress on Chemical Engineering, Prague, September 1969, paper No. C2.4.

Pannala, S., personal communications, 2005a.

Pannala, S., Daw, C. S. and Halow, J., Simulation of reacting fluidized beds using an agent-based bubble model. *International Journal of Chemical Reactor Engineering* **1**, A20, 2003.

Pannala, S., Daw, C. S., Finney, C. E. A. and Boyalakuntla, D., ORNL FY04 Process Modeling Summary Report for the Advanced Gas Reactor Fuel Development and Qualification Program. Oak Ridge National Laboratory, 2004.

Pannala, S., Boyalakuntla, D., Finney, C. E. A., Miller, J. H., Lowden, R. A., and Daw, C. S., Simulations of nuclear fuel particle coating in spouted bed reactors. AIChE Annual Meeting, 2005b.

Pannala, S., Boyalakuntla, D., Finney, C. E. A., Miller, J. H., Lowden R. A., and Daw, C. S., Simulations of spouted beds for coating TRISO fuel particles. AIChE Annual Meeting, 2005c.

Pannala, S., Boyalakuntla, D., Finney, C. E. A., and Daw, C. S., Simulations of spouted bed dynamics in the context of coating nuclear fuel particles. AIChE Spring National Meeting, 2006.

Pham, Q. T., Behavior of a conical spouted-bed dryer for animal blood. *Canadian Journal of Chemical Engineering* **61**, 426–434, 1983.

Rao, K. B. and Husain, A., Prediction of the maximum spoutable height in spout-fluid beds. *Canadian Journal of Chemical Engineering* **63**, 690–692, 1985.

Rocha, S. C. S., Taranto, O. P. and Ayub, G. E., Aerodynamics and heat transfer during coating of tablets in two-dimensional spouted bed. *Canadian Journal of Chemical Engineering* **73**, 308–312, 1995.

San José, M. J., Olazar, M., Aguayo, A. T., Arandes, J. M and Bilbao, J., Hydrodynamic correlations of conical jet spouted beds. Fluidization VII, Engineering Foundation, New York, 831–838, 1992.

San José, M. J., Olazar, M., Alvarez, S., Morales A. and Bilbao, J., Local porosity in conical spouted beds consisting of solids of varying density. *Chemical Engineering Science* **60**, 2017–2025, 2005a.

San José, M. J., Olazar, M., Alvarez, S., Morales, A. and Bilbao, J., Spout and fountain geometry in conical spouted beds consisting of solids of varying density. *Industrial and Engineering Chemistry Research* **44**, 193–200, 2005b.

Schaaf, J. van der, Ommen, J. R. van, Takens, F., Schouten, J. C. and Bleek, C. M. van den, Similarity between chaos analysis and frequency analysis of pressure fluctuations in fluidized beds. *Chemical Engineering Science* **59,** 1829–1840, 2004.

Schouten, J. C. and Bleek, C. M. van den, Chaotic hydrodynamics of fluidization: consequences for scaling and modeling of fluid bed reactors, *AIChE Symposium Series* **88**, 70-84, 1992.

Schouten, J.C. and Bleek, C. M. van den, Monitoring the quality of fluidization using the short-term predictability of pressure fluctuations. *AIChE Journal* **44**, 48–60, 1998.

Shuck, D. L. and Knudsen, I. E., Spouted bed blender apparatus. U. S. Patent 4577972, 1982.

Sierra, C., Tadrist, L. and Occelli, R., Local and global dynamics of shallow gas-fluidized beds. *Physics of Fluids* **18**, 043303, 2006

Smith, J. W. and Reddy, K. V. S., Spouting of mixed particle-size beds. *Canadian Journal of Chemical Engineering* **42**, 206, 1964.

Stinton, D. P. and Lackey, W. J., ORNL-TM-5743[1977] 1/30, C. A. 88, No. 160199., 1978.

Svoboda, K., Cermak, J., Hartman, M., Drahos, J. and Selucky, K., Pressure fluctuations in gas-fluidized beds at elevated temperatures. *Industrial and Engineering Chemistry Process Design and Development.* **22**, 514–520, 1983.

Takeuchi, S., Wang, S. and Rhodes, M., Discrete element simulation of a flat-bottomed spouted bed in the 3-D cylindrical coordinate system. *Chemical Engineering Science* **59**, 3495–3504, 2004.

Thorley, B., Mathur, K. B., Klassen, J. and Gishler, P. E., The effect of design variables on flow characteristics in a spouted bed. National Research Council Canada. Ottawa, 1955. (Quoted in Mathur and Epstein (1974b))

Thorley, B., Saunby, J. B., Mathur, K. B. and Osberg, G. L., An analysis of air and solid flow in a spouted wheat bed. *Canadian Journal of Chemical Engineering* **38**, 184, 1959.

Tsuji, Y., Kawaguchi, T. and Tanaka, T., Discrete particle simulation of two-dimensional fluidized bed. *Powder Technology* **77**, 79–87, 1993.

Tsvik, M. Z., Nabiev, M. N., Rizaev, N. U. *et al.*, The velocity for external spouting in the combined process for production of granulated fertilizer. *Uzbekskii Khimicheskii Zhurnal* **11**, 50–59, 1967. (Quoted in Mathur and Epstein (1974b))

Van Velzen, D., Flamm, H. J. and Langenkamp, H., Gas flows in spouting beds. Dragon Project Report No. 785. Euratom, Ispra, Italy, 1972.

Voice, E. H. and Lamb, D. N., DP-Report-677[1969] 1/86. N.S.A. 28, NO 8546, 1973. (Cited by Heit (1986))

Wan-Fyong, F., Romankov, P. G. and Rashkovskaya N. B., Research on the hydrodynamics of the spouted bed. *Zhurnal Prikladnoi Khimii* **42**, 609–617, 1969. (Quoted in Mathur and Epstein (1974b))

White, F. M., **Fluid Mechanics**, McGraw-Hill, New York, 2003.

Xu, J., Bao, X. and Wei, W., *et al.*, Statistical and frequency analysis of pressure fluctuation in spouted beds. *Powder Technology* **140**, 141–154, 2004.

Zhong, W., Xiong, Y.,Yuan, Z. and Zhang, M., DEM simulation of gas-solid flow behaviors in spouted-fluid bed. *Chemical Engineering Science* **61**, 1571–1584, 2006.

Zhong, W. and Zhang, M., Pressure fluctuation frequency characteristics in a spout-fluid bed by modern ARM power spectrum analysis. *Powder Technology* **152**, 52–61, 2005.

Vita

Jiandong Zhou graduated in July of 1992 with a B. S. in Polymer Science in the College of Chemical Engineering and Materials Science in Beijing Institute Technology (BIT). He obtained his first Master's degree on Materials Science in BIT in March of 1995. He spent 5 years on chemical process design, simulation and optimization in WUZHOU Engineering Design & Research Institute in Beijing from April, 1995 to April, 2000. Jiandong Zhou graduated in August of 2002 with his 2nd M.S. in Chemical Engineering of the University of Tennessee, Knoxville (UTK). Then he continued his graduate study towards Ph.D degree in chemical engineering at UTK. In 2006, he also obtained his Master degree on Statistics science.